공학박사 학위논문

From Intrinsic to Extrinsic Design of Electrode Materials for the High-Performance Lithium-Ion Batteries

전극소재의 내적/외적 기능 설계를 통한 고성능 이차전지 개발

2021년 8월

서울대학교 대학원

재료공학부

정 철 호

From Intrinsic to Extrinsic Design of Electrode Materials for the High-Performance Lithium-Ion Batteries

지도 교수 홍 성 현

이 논문을 공학박사 학위논문으로 제출함
2021년 8월

서울대학교 대학원
재료공학부
정 철 호

정철호의 공학박사 학위논문을 인준함
2021년 4월

위 원 장 박 병 우

부위원장 홍 성 현

위 원 김 미 영

위 원 조 우 석

위 원 정 성 균

Abstract

From Intrinsic to Extrinsic Design of Electrode Materials for the High-Performance Lithium-ion Batteries

Chul-Ho Jung

Department of Materials Science and Engineering

The Graduate School

Seoul National University

Since the commercialization of lithium-ion batteries (LIBs) by Sony Corporation in 1991, extensive researches have been conducted to meet the demand of the consumer needs. Especially, with the emergence and rapid growth of large-scale energy storage devices such as electric vehicles (EVs), the development of low cost and high energy density LIB electrode materials is highly demanding. In perspective of cathode materials, most widely used $LiCoO_2$ (LCO) layered oxide has faced the severe limitation due to its limited practical capacity (~140 mAh g^{-1}) and high price of cobalt (Co). To meet the automotive battery need (350 Wh/kg at US $75/kWh at cell level), further extraction of lithium from the crystalline structure and substitution of high price Co with other elements are highly required. In this regard, three component layered $LiNi_xCo_yMn_{1-x-y}O_2$ (LNCM) has successfully substituted the LCO layered oxide over the years and solidified their status as the cathode material of choice for EV batteries. Nevertheless, the practical implementation of Ni-rich layered oxides is currently hindered by their continuous capacity fading and especially, the deterioration becomes increasingly severe with the increase of Ni content or at a high state of charge (SOC). To overcome these issues,

the development of low-cost methods, new materials design strategies, and a comprehensive understanding of electrochemical mechanisms is prerequisite.

In the first chapter of this thesis, intrinsic characteristics of LIB cathode material is modified through Zr doping in order to improve its cathodic performance. In specific, we provide the comprehensive analyses of the Zr doping effects in a $LiNi_{0.92}Co_{0.04}Mn_{0.04}O_2$ LIB cathode material with a focus on discovering the critical origin of its mechanism. First, by adopting multi-length-scale X-ray spectroscopic analysis and gas analysis technique, we show that Zr doping enhances the electrochemical performance of LNCM by suppressing the abrupt c-axis contraction, particle cracks, oxygen evolution, electrolyte decomposition, and Li–Ni disorder, thus alleviating the diverse LNCM degradation factors. Then, the fundamental role of Zr doping is systematically investigated with the collaboration of state-of-the-art magnetometer, resonant inelastic X-ray scattering (RIXS), scanning transmission X-ray microscopy (STXM), and first-principles calculations. For the first time, we revealed that Zr doping suppresses the oxygen oxidation upon deep charge, which is associated with the oxygen instability and to the multiple degradation factors.

In the second chapter, extrinsic characteristics of LIB cathode material is modified by doping to enhance the cathode cycle life. In specific, the textured microstructure, in which the primary particles are aligned along the radial direction, has been managed by the phosphorous or boron doping. Previously, the origin of crystalline texture by the B doping have been proposed as the surface energy modification. The proposal has been suggested by using first-principle calculations, however, systematic investigation to understand the doping mechanism on the microstructure modulation has not yet been conducted. In this chapter, systematic investigation has been conducted to reveal the origin of the texture structure through B/P doping on Ni-rich

layered oxide. For the first time, we have unveiled that the unique crystallographic texture of B/P doped layered oxide was originated from the hydroxide precursor morphology, while the mechanism was highly related to the formation of an amorphous layer that delayed the recrystallization onset temperature during synthesis.

In the third chapter, we provide design strategy for the microstructure textured Ni-rich layered oxide. In specific, two microstructure textured layered cathode, that is, P doped layered oxide and B doped layered oxide, have been electrochemical tested and compared. Attributed by its texture, both P- and B-doped cathodes suppressed the microcrack formation and improved the cycle life compared to the undoped cathode, however, there existed meaningful capacity retention difference between the doped cathodes. To elucidate the underlying mechanisms behind the cyclability difference between the doped cathodes, we conducted various measurements starting from multi-length-scale X-ray spectroscopic analysis to gas analysis technique. From the results, we have revealed that the cycle life difference between the doped cathodes was highly related with the behavior of oxygen stability that depended on primary particles orientation facet, in which B-LNCM primary particles exposed a facet that is stable against oxygen release, therefore leading to better cycle life compared to P-LNCM.

Keywords: Lithium-ion battery, layered oxide, doping, mechanism, textured microstructure

Student Number: 2016-20828

Table of Contents

List of Figures and Tables

Figure 1.3.4. (a) *In-situ* XRD plot of layered cathode during charge. Reproduced with permission [55]. Copyright 2019, American Chemical Society, (b) cyclability comparison of $LiNi_xCo_yMn_zO_2$ (x=0.6, 0.8, 0.9, 0.95, 1), (c) dQ/dV plot of Ni-low (x=0.6) NCM/Ni-rich NCM (X=0.95), (d) c-axis lattice parameter of $LiNi_xCo_yMn_zO_2$ (x=0.6, 0.8, 0.9, 0.95, 1) as a function of cell voltage, (e) cross-sectional SEM image of cycled Ni-low (x=0.6) NCM/Ni-rich NCM (X=0.95). (b, c, d, e) Reproduced with permission [59]. Copyright 2018, American Chemical Society, (f) comparison of galvanostatic graph and variation of c-axis lattice parameter depending of Ni content of NCM. Reproduced with permission [60]. Copyright 2019, American Chemical Society, and (g) Badar charge calculation of Li_xNiO_2 during delithiation process. Reproduced with permission [61]. Copyright 2017, American Chemical Society.

Figure 1.3.5. (a) Cross-sectional HADDF images of cycled NCM622, (b) intragranular crack formation along the (003) plane, (c) HADDF imaging and (d) EELS analysis showing the phase transformation around the intragranular crack. (a, b, c, d) Reproduced with permission [62]. Copyright 2018, Springer Nature, (e) Finite element modeling (FEM) model of NCM. Reproduced with permission [63]. Copyright 2018, American Chemical Society, (f) presence of nanopore inside NCM, (g) HADDF imaging and (h) EELS analysis showing the phase transformation around the nanopore. (f, g, h) Reproduced with permission [64]. Copyright 2019, American Chemical Society.

Figure 1.3.6. (a) Schematic on illustrating the characterization techniques for observing the NCM degradation factors, (b) XRD profile to observe the degree of cation mixing by using (003)/ (104) intensity ratio. (b) Reproduced with permission [65]. Copyright 2020, Wiley. (c) *Operando* differential electrochemical mass spectrometry (DEMS) analysis for the LIBs cathode materials. (c) Reproduced with permission [66]. Copyright 2017, American Chemical Society. (d) Mapping of resonant inelastic X-ray scattering (mRIXS) analysis to observe the oxidized oxygen. (d) Reproduced with permission [69]. Copyright 2019, American Chemical Society.

Figure 1.4.1. (a) Schematic illustration of the Na doping effect in NCA 811, (b) HAADF images of undoped and Zr-doped NCM after cycling. Reproduced with permission [73]. Copyright 2019, Wiley, (c) HAADF images of the Mo-doped NCM 523. Different locations in the bulk and at the surface are indicated as areas 1, 3 and 2, 4, respectively, (d) EDS spectra

acquired from areas 1-4. (c, d) Reproduced with permission [76]. Copyright 2018, American Chemical Society, and (e, f) bright field images and corresponding ASTAR TEM phase mapping for (e) undoped LNO and (f) W-doped LNO. (e, f) Reproduced with permission [78]. Copyright 2018, Royal Society of Chemistry.

Figure 1.4.1.1 (a) TGA measurement of mass loss (thick line) and derivative of weight (thin line) of charged undoped and Sn-doped NCM 622. Reproduced with permission [79]. Copyright 2018, Elsevier, (b) soft XAS spectra of O K-edge for undoped and Ti-doped NCA 811. Reproduced with permission [72]. Copyright 2019, American Chemical Society, (c) SEM images of undoped and B-doped NCM 90. Reproduced with permission [83]. Copyright 2018, Wiley, and (d) cross-sectional SEM images of the 1st charged states at 4.5 V of undoped NCM 90 and W-doped NCM90. (d) Reproduced with permission [85]. Copyright 2019, Elsevier.

Figure 1.4.2. (a) HRTEM image of Al_2O_3-coated NCM 622. (b) DSC curves of bare and Al_2O_3-coated NCM 523. (a, b) Reproduced with permission [86]. Copyright 2016, Elsevier, (c) cycle performance and (d) rate capability of bare NCM 622, Li-Al-O-2, and Al-O-2. (c, d) Reproduced with permission [88]. Copyright 2018, Elsevier, (e, f) *in situ* XRD patterns for charged bare NCM and LP-NCM in the temperature range of (e) 276-384 ℃ and (f) 394-500 ℃. (e, f) Reproduced with permission [90]. Copyright 2017, Elsevier, (g) scheme of the formation of glue layer on NCA, and (h) STEM images of bare and LCO-infiltrated NCA after 300 cycles. (g, h) Reproduced with permission [91]. Copyright 2016, Wiley.

Figure 1.4.3. (a) Scheme of core-shell, (b) CP-SEM images of bare NCM and core-shell design NCM after cycles. (b) Reproduced with permission [95]. Copyright 2019, Wiley, (c) SEM image of single-crystal NCM 622. Reproduced with permission [96]. Copyright 2016, Elsevier, (d) CP-SEM images of poly-crystal NCM 811 and SC-NCM after cycles. (d) Reproduced with permission [97]. Copyright 2020, Elsevier, (e) scheme of Cd gradient doping, (f) CP-SEM images of Cd gradient doped-NCA 811, (g) EDS mapping analysis of Cd content from the region marked with red dots in (f). (e, f, g) Reproduced with permission [98]. Copyright 2020, Elsevier, (h) HAADF-STEM images of the stabilizer on the NCM surface, (i) corresponding HAADF signal profiles of the pink and blue boxes in (h), and (j) TEM image of the graphite anode after cycling test. (h, i, j) Reproduced with permission [101]. Copyright 2018, Royal Society of Chemistry.

Figure 2.1. HRPD patterns of as-synthesized (a) U-LNCM and (b) Zr-LNCM powders. (c) The Reteiveld refinement results of as-syntheiszed powders. SEM images of (d) U-LNCM and (e) Zr-LNCM. (f) Cross-sectioned polished SEM image of Zr-LNCM and its EDS mapping data.

Figure 2.2. (a) Initial charge-discharge voltage profiles for U-LNCM and Zr-LNCM electrodes between 2.5 and 4.4 V (vs. Li^+/Li) at the current density of 0.1 C (1 C= 200 mA g^{-1}). (b) Cycle performance of U-LNCM and Zr-LNCM electrodes at the current density of 0.3 C for 100 cycles, while 0.1 C current density was applied at 101^{th} cycle. (c) Cycle comparision between the various Zr mole % doped LNCM. (d) Rate performance of the electrodes by varying the current density from 0.1 to 2 C. (e) The calculated lithium ion mobility of U-LNCM and Zr-LNCM by using GITT analysis.

Figure 2.3. (a) *In situ* XRD patterns of U-LNCM and Zr-LNCM electrodes during charge process at current density of 0.2 C. Cross-sectioned polished SEM images of (b) pristine U-LNCM, Zr-LNCM and after 50^{th} cycled (c) U-LNCM, Zr-LNCM electrodes. The upper data corresponds to U-LNCM while the below are Zr-LNCM data.

Figure 2.4. Line-scanning EELS spectra of O K-edge and Ni L-edge (as-labeled) for after cycled (a) U-LNCM and (b) Zr-LNCM. Differential electrochemical mass spectrometry (DEMS) spectra of (c) U-LNCM and (d) Zr-LNCM electrodes when charged to 4.8 V at 0.1 C current density. Atomic-resolution STEM images of after 50^{th} cycled (e) U-LNCM and (f) Zr-LNCM. Scale bars are 2 nm.

Figure 2.5. EIS measurements of the charged samples for (a) U-LNCM and (b) Zr-LNCM upon cycling from 1^{st} to 100^{th}

Figure 2.6. (a) Galvanostatic graphs of U-LNCM and Zr-LNCM with the points indicating the SOC states in which Squid-VSM analyses have been taken. Susceptibility versus temperature graph for the (b) U-LNCM and (c) Zr-LNCM samples. (d) Calculated effective paramagnetic moment of the samples depending on the SOC. (e) Schematic illustration of the sudden increase of magnetic moment upon high SOC.

Figure 2.7. (a) O K-edge mRIXS analysis of U-LNCM and Zr-LNCM during first cycle delithiation (x, $Li_{1-x}MO_2$). (b) O-K mRIXS-sPFY analysis of U-LNCM and Zr-LNCM at x=0.88 state, where the peak on the shaded area around 530~532 eV indicates the oxidized

oxygen. (c) Ni L-edge STXM results of U-LNCM and Zr-LNCM during first cycle delithiation (x, $Li_{1-x}MO_2$). (d) Atomic structure of $Li_{12}Ni_{11}ZrO_{24}$, (e) atomic structure near Ni atom, and (f) atomic structure near Zr atom. The number on (e) and (f) indicates the charge loss of corresponding oxygen when delithiated from $Li_{12}Ni_{11}ZrO_{24}$ to $Li_2Ni_{11}ZrO_{24}$, which is obtained by the Badar charge analysis.

Figure 2.8. Temperature-resolved heating XRD patterns of 4.4 V charged (a) U-LNCM and (b) Zr-LNCM. The thermal decomposition temperature of the electrode is 480 and 520 °C for U-LNCM and Zr-LNCM, respectively.

Figure 3.1.1. X-ray diffraction patterns of as-synthesized U-LNCM, P-LNCM, and B-LNCM powders, which was annealed at 740 ℃ 12h.

Figure 3.1.2. Low magnification SEM images of (a) U-LNCM, (d) P-LNCM, (g) B-LNCM, and (j) NCM precursor, high magnification SEM images of (b) U-LNCM, (e) P-LNCM, (h) B-LNCM, and (k) NCM precursor. Cross-sectioned polished SEM images of (c) U-LNCM, (f) P-LNCM, (i) B-LNCM, and (l) NCM precursor powders.

Figure 3.1.3. HRTEM image of (a) P-LNCM, (d) B-LNCM, and (g) NCM precursor. STEM image of (b) P-LNCM, (e) B-LNCM, and (h) NCM precursor. Fast fourier transform image of (c) P-LNCM, (f) B-LNCM, and (i) NCM precursor.

Figure 3.1.4. Microstructure comparison between the as-synthesized U-LNCM, P-LNCM, B-LNCM, and NCM precursor particles by using (a) NCM 622 precursor and (b) NCM 811 precursor.

Figure 3.1.5. Synthesis time varied *ex-situ* SEM analysis of the as-synthesized powders. Synthesis time was varied from 0 minutes to 12 hours, while the annealing temperature was fixed to 740 ℃.

Figure 3.1.6. Synthesis time varied *ex-situ* XRD analysis of the as-synthesized (a) U-LNCM, (b) P-LNCM, and (c) B-LNCM powders. Synthesis time was varied from 0 minutes to 12 hours, while the annealing temperature was fixed to 740 ℃.

Figure 3.1.7. Synthesis temperature varied *ex-situ* SEM analysis of the as-synthesized powders. Synthesis temperature was varied from 600 ℃ to 840 ℃, while the annealing time was fixed to 12 hours.

Figure 3.1.8. Synthesis temperature varied *ex-situ* XRD analysis of the as-synthesized (a) U-LNCM, (b) P-LNCM, and (c) B-LNCM powders. Synthesis temperature was varied from 600 ℃. To 840 ℃., while the annealing time was fixed to 12 hours.

Figure 3.1.9. HRTEM image of FIB cross-sectioned (a) B-LNCM and (b) P-LNCM, which showed the amorphous layer covering the particle surface. (c) EDS mapping and (d) EELS analysis of P-LNCM. (e) Microstructure comparison between the 1 mole % doped P- and B-LNCM with the 5 mole % doped P- and B-LNCM.

Figure 3.1.10. HRTEM image of FIB cross-sectioned (a) 1 mole % doped P-LNCM and (b) 5 mole % doped P-LNCM, which showed the increase of amorphous layer thickness upon doping amount.

Figure 3.1.11. (a) SEM image of FIB cross-sectioned U-LNCM (650 ℃ 12h).HRTEM image of U-LNCM (650 ℃ 12h) with showing (b) original plate-alike particle [A] and (c) newly formed ellipse-alike particles [B,C]. STEM image of (d) particle A, (e) particle B, and (f) particle C. FFT image of (h) particle A, (i) particle B, and (j) particle C.

Figure 3.1.12. HRTEM image of FIB cross-sectioned U-LNCM annealed at (a) 650 ℃ 12h and (b) 740 ℃ 12h.

Figure 3.1.13. Disorientation angle within the inner primary particle for the 740 ℃ 12 h annealed (a) U-LNCM, (b) P-LNCM, and (c) B-LNCM, calculated from the scanned procession NBD data. Low magnification STEM image of 740 ℃ 12 h annealed (d) U-LNCM, (e) P-LNCM, and (f) B-LNCM.

Figure 3.2.1. (a) HRPD patterns of as-synthesized U-LNCM, P-LNCM, and B-LNCM powders. Enlarged patterns for (b) (006)/(102) and (018)/(110) peaks and (c) (003) peaks. (d) Calculated lattice parameters by Rietveld refinement for as-synthesized U-LNCM, P-LNCM, and B-LNCM powders.

Figure 3.2.2. FT-IR spectra of as-synthesized U-LNCM, P-LNCM, and B-LNCM powders.

Figure 3.2.3. Low maginification SEM images of (a) U-LNCM, (d) P-LNCM, and (g) B-LNCM, high maginification SEM images of (b) U-LNCM, (e) P-LNCM, and (h) B-LNCM, and cross-sectioned polished SEM images of (c) U-LNCM, (f) P-LNCM, and (i) B-LNCM powders.

Figure 3.2.4. Schematic illustration for the FIB preparation and TEM observing direction.

Figure 3.2.5. (a) HR-TEM image of P-LNCM particle and (b) atomic resolution image of marked area in (a), (c) HR-TEM image of B-LNCM particle and (d) atomic resolution image of marked area in (c). Color-coded crystallographic orientation maps of cross-sectional TEM sample of (e) U-LNCM, (f) P-LNCM, and (g) B-LNCM obtained by ASTAR device (NanoMEGAS) (The orientation of the planes is normal to z-axis), and (i) color codes for the crystal orientation maps expressed in the standard stereographic triangle notation.

Figure 3.2.6. (a) Initial charge-discharge voltage profiles of U-LNCM, P-LNCM, and B-LNCM electrodes between 2.5 and 4.4 V (vs. Li^+/Li) at the current density of 0.1 C (1 C= 200 mA g^{-1}), (b) cycle performance of U-LNCM, P-LNCM, and B-LNCM electrodes at the current density of 0.3 C, (c) rate test for the three electrodes, and dQ dV^{-1} profiles obtained by differentiating the charge-discharge profiles at 5^{th}, 10^{th}, 15^{th}, and 30^{th} cycles for (d) U-LNCM, (e) P-LNCM, and (f) B-LNCM electrodes.

Figure 3.2.7. Enlarged HRPD patterns of (003) peak for (a) pristine/cycled U-LNCM, (b) pristine/cycled P-LNCM, and (c) pristine/cycled B-LNCM electrodes. Rietveld refinement results of (d) pristine U-LNCM, (e) pristine P-LNCM, (f) pristine B-LNCM, (g) cycled U-LNCM, (h) cycled P-LNCM, and (i) cycled B-LNCM electrodes.

Figure 3.2.8. Variation of (a) lithium ion mobility and (b) charge transfer resistance depending on cycles. Lithium ion mobility was calculated by GITT measurement whereas charge transfer resistance was determined by EIS measurement. GITT measurements for (c) U-LNCM, (d) P-LNCM, and (e) B-LNCM. EIS measurements for (f) U-LNCM, (g) P-LNCM, and (h) B-LNCM electrodes.

Figure 3.2.9. *In situ* XRD patterns of (a-1) U-LNCM, (a-2) P-LNCM, and (a-3) B-LNCM electrodes and cross-sectioned polished SEM images of pristine (b-1) U-LNCM, (b-2) P-LNCM, and (b-3) B-LNCM electrodes and after 50^{th} cycled (c-1) U-LNCM, (c-2) P-LNCM, and (c-3) B-LNCM electrodes.

Figure 3.2.10. HR-TEM images of cycled (a) U-LNCM, (d) P-LNCM, and (g) B-LNCM electrodes, line-scanning EELS spectra of O K-edge and Ni L-edge (as-labeled) for (b) frontal and (c) lateral facets of cycled U-LNCM, (e) frontal and (f) lateral facets of cycled P-LNCM, and (h) frontal and (i) lateral facets of cycled B-LNCM electrodes. (j) (003) plane and (k) (102) plane for $LiNiO_2$, and (l) oxygen vacancy formation energy of (003) and (102) planes.

Figure 3.2.11. Atomic-resolution STEM images of (a) P-LNCM pristine, (b) P-LNCM cycled, (c) B-LNCM pristine, and (d) B-LNCM cycled electrodes. Scale bars are 2 nm.

Figure 3.2.12. Differential electrochemical mass spectrometry (DEMS) spectra of (a) U-LNCM, (b) P-LNCM, and (c) B-LNCM electrodes when charged to 4.8 V at 0.1 C current density, (d) schematic illustration of cycle stability difference between P-LNCM and B-LNCM electrodes, and soft X-ray absorption spectroscopy (sXAS) O K-edge FY mode spectra for pristine/cycled (e) P-LNCM and (f) B-LNCM electrodes and sXAS Ni L-edge FY mode spectra for pristine/cycled (g) P-LNCM and (h) B-LNCM electrodes.

Chapter 1.

General Background

1.1. Overview: Layered oxide for Li-ion batteries cathode

Since the commercialization of lithium ion batteries (LIBs) by Sony Corporation in 1991, extensive researches have been conducted to meet the demand of the consumer needs [1, 2]. Especially, with the emergence and rapid growth of large scale energy storage devices such as electric vehicles (EVs), the development of low cost and high energy density LIB electrode materials is highly demanding [3]. In perspective of cathode materials, the layered transition metal oxides have been recognized as promising cathode materials for high energy density applications owing to their high theoretical capacity (~280 mAh g^{-1}) compared with that of olivine (~170 mAh g^{-1}) or spinel (~150 mAh g^{-1}) materials [4, 5]. As the most widely used $LiCoO_2$ (LCO) layered oxide can only provide a limited practical capacity due to its narrow potential window (~4.3 V vs Li/Li^+), its derivative $LiNi_xCo_yMn_{1-x-y}O_2$ (NCM) or $LiNi_xCo_yAl_{1-x-y}O_2$ (NCA) materials are regarded as the most promising substitutions for LCO that can potentially reduce the cost and enhance the energy the density of LiBs [6, 7]. Currently, nickel content less than 60% have been successfully commercialized [8].

It is significantly important to achieve the high state-of-charge (SOC) within the limited voltage window (~4.4 V vs Li/Li^+) to increase the practical capacity. As the high Ni content locates the e_g in acceptor band at higher position, it requires less energy to extract the electron within same voltage compared to the low Ni cathode [9]. Therefore, the Ni-rich cathodes with

above 80% Ni content are receiving a great interest, which allow the high capacity (above 200 mAh g^{-1}) on the fixed voltage [10-13]. Even though NCM offers the attractive features, the degradation of NCM materials occurs from nanometer-scale to micro-scale during battery cycling, which results in an electrochemical failure. Briefly to mention, the degradation of NCM can be attributed to undesired Li-Ni cation disorder (so called cation mixing), oxygen release, dissolution of transition metals, electrolyte decomposition, state-of-charge (SOC) heterogeneity within the particle, and formation/propagation of microcracks between the primary particles and within the primary particle [14-17]. To solve these problems, many scientists have conducted the extensive researches over the past years. For example, the partial replacement of transition metal (TM) with other elements via doping [18-21], surface coating [22-24], morphology design [25, 26], etc. have been suggested, which effectively enhanced the cycle lifespan of layered cathodes. However, as these strategies alleviate more than one degradation phenomenon, the fundamental origin of its effect on the layered cathode is still under debate. For instance, it has been reported that tungsten doping could restrain the cation mixing, oxygen evolution, and particle cracking during multiple cycles [18]. Thus, several proposals are being drawn up on explaining the mechanism of doping effects on the layered cathode, which have not been integrated into one. We believe that the interference of each proposal arises from the perception that the above-mentioned degradations are being considered as an independent phenomenon, however, in fact, they are highly correlated. To truly propose and develop the design strategy to resolve the deterioration of NCM cathodes, the fundamental finding of the degradation mechanism correlation has to be preceded beforehand.

Therefore, this review article focuses on the insightful understanding of the capacity/voltage fading mechanisms of NCM with an aim to provide important clues for the future design of

layered lithium transition metal oxides. Before introducing the degradation mechanisms of NCM cathodes, we first discuss the crystal structure and electronic configuration of the layered cathodes as their characteristics are linked with the NCM deterioration mechanisms. Then, on the discussion of each fatigue mechanism, we focus on discovering the correlations between each individual mechanism that had been considered as independent phenomenon on the previous review papers [1, 2, 9, 14]. Finally, after overviewing the NCM degradations, we present the recent NCM material designs with an effort to discover the direct relationship between proposed solving strategies and fatigue mechanisms.

1.2. Crystal structure and electronic configuration of layered cathodes

The crystal structure of layered NCM materials (Figure 1.2a), in general written as $LiTMO_2$, consists of cubic closed-packed (ccp) oxygen layers with Li and TM occupying the intestinal sites along the $[111]_{cubic}$ direction ($[001]_{hexagonal}$ direction). The resulting structure is rhombohedral with a space group of R-3m, which is derived from the ordered rock-salt structure of α-$NaFeO_2$ [27]. The layers filled by TM cations form the TMO_2 sheets consists of edge-sharing TMO_6 octahedra. The lithium ions are intercalated between the TMO_2 sheets which can occupy the prismatic (P), tetrahedral (T), or octahedral (O) sites [9, 28]. The lithium ions occupy the octahedral sites for the most widely used layered compounds in lithium ion batteries [29]. This type of $LiTMO_2$ is normally referred as O3-type structure because the oxygen has an ABCABC stacking with three repeating unit. Oxygen occupies the 6c site in Wyckoff notation while TM occupies 3a site and Li occupies the 3b site, yielding $[Li]_{3b}[TM]_{3a}[O2]_{6c}$. The TM site is occupied by a combination of Ni, Co, and Mn elements. However, it is difficult to synthesize the stoichiometric $LiTMO_2$ materials with exact

Li:TM=1:1 ratio due to Li^+/Ni^{2+} cation disorder resulting from the similar ionic radius (Li^+: 0.76 Å and Ni^{2+}: 0.69 Å) [30]. Thus, the chemical formula can be actually written as $[Li_{1-z}Ni_z]_{3b}[Ni_{x-z}Co_yMn_{1-x-y}]_{3a}[O2]_{6c.}$ The synthesis of ideal stoichiometry becomes much challenging with increasing the Ni-content, especially in case of $LiNiO_2$ due to a low-spin Ni^{3+} (electronic configuration: $t_{2g}^6e_g^1$), which induces the Jahn-Teller distortion [31]. Furthermore, Li^+/Ni^{2+} cation disorder (widely denominated as cation-mixing) also occurs during cycling process which will be further discussed on later section.

In perspective of the electronic structure, the different transition metals in $LiTMO_2$ play a critical role in the relative energy of redox levels. In addition, the position of TM redox-active energy level relative to the oxygen 2p energy level may affect the oxygen reaction/evolution [32]. According to the crystal-filed splitting theory, the hybridization of oxygen anion with transition metal splits the five transition metal bands into two sets of e_g (d_{x2-y2}, d_{z2}) and t_{2g} (d_{xy}, d_{xz}, d_{yz}) levels (Figure 1.2b). The e_g levels have a higher energy than the t_{2g} levels due to the increased electrostatic repulsion from the coordinating anion [33]. When comparing the relative redox energy levels, Co^{3+}/Co^{4+} is located at lower energy than Ni^{2+}/Ni^{3+}, Ni^{3+}/Ni^{4+}, or Mn^{3+}/Mn^{4+}, which means that higher charge voltage is required to achieve the identical capacity for $LiCoO_2$ compared to $LiNiO_2$ or $LiMnO_2$. This is because the electron has to be extracted from the energetically stable t_{2g} level for Co^{3+} (electronic configuration: $t_{2g}^6e_g^0$), while the electron can be extracted from unstable e_g level for Ni^{2+} (electronic configuration: $t_{2g}^6e_g^2$), Ni^{3+} (electronic configuration: $t_{2g}^6e_g^1$), and Mn^{3+} (electronic configuration: $t_{2g}^3e_g^1$) [33]. Thus, for NCM cathodes, the oxidation occurs first from $Ni^{2+}\rightarrow Ni^{3+}$, followed by the oxidation of $Ni^{3+}\rightarrow Ni^{4+}$, and then finally the oxidation of $Co^{3+}\rightarrow Co^{4+}$. Mn is in 4+ valence state, therefore, Mn does not participate in the redox process for NCM [34].

With respect to Ni:Co:Mn ratio, the increase or decrease of one-element affects the NCM

materials in terms of electrochemical/thermal properties. This is because a trade-off relationship lies in TM ratio. The main redox center of NCM is Ni^{2+}/Ni^{3+} and Ni^{3+}/Ni^{4+}, thus increasing the nickel content increases the practical capacity, while cobalt enhances the rate capability and reduces the Li/Ni cation disorder, and manganese improves the structural/thermal stability (Figure 1.2c). It is widely accepted that manganese valence state is fixed to be 4+ during charge/discharge, while there is a debate whether oxidation state of cobalt varies during cycling [35]. By combining each TM's pros/cons, the most widely used and being researched TM ratios are NCM333, NCM523, NCM622, NCM811, and $LiNiO_2$ (LNO). Even though the Ni-low NCM (Ni<60%) provides the satisfactory cycle/rate performance as well as good thermal characteristics, it delivers a relatively low practical specific capacity (<200mAh g^{-1}), which could not meet the industrial demand that is required for large scale energy storage devices. Therefore, Ni-rich cathode with Ni content over 80% is an attractive alternative candidate that can provide the specific capacity more than 200 mAh g^{-1} at 4.3 V charge voltage. However, Ni-rich NCM possesses the several instability issues from as-prepared state to cycled state that have to be faced for the practical applications. First, due to insufficient amount of Co and Mn atoms around Ni ion, individual Mn and Co clusters are segregated on the particle surface that can lead to the instability of Ni-rich NCM [36]. Second, Ni valence for as-prepared Ni-rich NCM is in the state of 3+. As Ni^{3+} is active Jahn-Teller (JT) ion due to unpaired electron on e_g band, it is highly unstable and tends to reduce to inactive JT Ni^{2+} ion during synthesis process, therefore making hard to obtain well stoichiometric $LiTMO_2$ [32]. Third, Ni-rich NCM shows a poor cycle performance due to cation mixing, oxygen evolution, and mechanical instability etc. which will be thoroughly discussed in the next section.

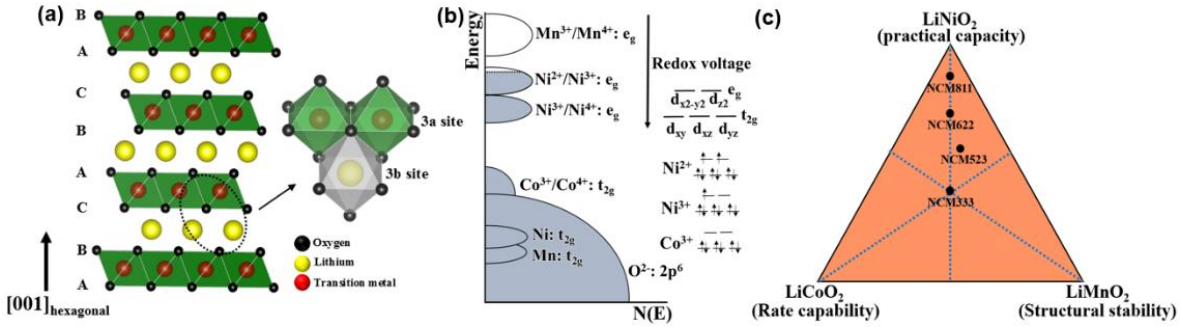

Figure 1.2. (a) Illustration of crystal structure for the lithium layered oxide, (b) typical electronic configuration in NCM layered oxide and (c) compositional phase diagram of NCM cathode illustrating the effect of transition metal ratio on the electrochemical performance.

1.3. Fatigue mechanisms and challenges

Even though the NCM layered cathode is an attractive material with low cost and high practical capacity, the commercialization is hindered by the challenges that occur from the particle outer surface to the inner bulk. The Li-Ni cation mixing, which increases the cathode polarization, occurs mainly on the particle surface and thus, it is notated as "surface reconstruction layer (SRL)" [37, 38]. Furthermore, the cation mixing concurrently occurs with the oxygen release as this phenomenon transforms the layered phase ($LiTMO_2$) to the oxygen depleted spinel/rock-salt phase (TMO_x). The oxygen gaseous evolution during the degradation threats the battery to explode during cycling, thus exposing the battery on "vulnerable thermal characteristics" [39]. On the bulk-scale, due to an insufficient time for the electron/lithium to diffuse along the micrometer sized secondary particles during charge process, non-equilibrium lithium distribution on the particle leads to "state-of-charge (SOC) heterogeneity" within the NCM cathode, which could accelerate the degradation [40]. Finally, the sudden c-axis contraction upon charging provokes the particle cracking, which provides the electrolyte

infiltration pathway that leads to the unwanted side reactions. The particle cracks occur between the particle's gaps and also within the individual particle, which is denominated as "intergranular cracks" [41] and "intragranular cracks" [42], respectively. On the overview of NCM degradation, we discuss the fatigue mechanisms starting from outer particle surface to bulk degradation in sequence. After summarizing the degradation mechanisms, we briefly discuss about the "characterization techniques" that are used to analyze the NCM degradation factors.

1.3.1. Surface reconstruction layer (cation-mixing)

During the charge process (delithiation), NCM is in a metastable state and is thermodynamically unstable compared to fully lithiated state. With the extraction of Li^+ during charging, Ni is in the unstable valence state of 3+ or 4+. For Ni^{3+}, due to unpaired electron spin on e_g orbitals, Ni^{3+} tends to reduce to Ni^{2+} in the FCC octahedral site [38]. For Ni^{4+}, as it is highly reactive species, it tends to react with the electrolyte and reduces to Ni^{2+} with releasing the O_2 gas. As mentioned earlier, due to the similarity of ionic size between Li^+ (0.76Å) and Ni^{2+} (0.69 Å), Ni^{2+} tends to migrate from TM-slab 3a site toward Li-slab 3b site, which is designated as a "cation mixing" (Figure 1.3.1a). This migration transforms the perfect layered structure (R-3m) to spinel structure (Fd-3m) and eventually to rock salt structure (Fm-3m) (Figure 1.3.1b). This phase transformation has been recognized as one of the major NCM degradation mechanisms [37]. Compared to the perfect layered structure, a disordered structure has a higher activation energy barrier for lithium ion migration because the transition metals in Li-slab kinetically hinder the lithium migration. Thus, rate capability as well as cyclability degrade with an intensified cation mixing. Jung et al. reported that the phase transformation

occurred on the surface even at first cycle and reached a penetration depth of 20 nm after 50 cycles for the case of NCM523 (Figure 1.3.1c) [43]. The penetration depth became more severe when cycled at higher charge voltage because the oxygen CCP structure becomes unstable due to the empty lithium sites. Furthermore, the cycling with higher current rate also promoted the faster structure degradation. Especially, this phase transformation is widely observed only on the particle surface, while the bulk phase transformation is rarely reported. Kong et al. have systematically studied and suggested that the cation mixing behavior only observed on the particle surface is related to the oxygen evolution [44]. First, they have discovered that the oxygen vacancy formation energy dramatically decreased with increasing x in $Li_{1-x}NiO_2$ (formation energy decreases from 1.8 eV (for x=0) toward 0.35 eV (for x=0.75)), which indicates that oxygen is more prone to be released during delithiation process (Figure 1.3.1d). As the oxygen 2p states are hybridized with the transition metal 3d orbitals, the nickel oxidation during charge process introduces the hole in oxygen p orbital to form highly reactive peroxide O_2^{2-}, which results in the oxygen loss [7]. Then, to find a correlation relationship between presence of oxygen vacancy and tendency of Ni migration to Li-slab, Ni migration energy barrier has been calculated and the result showed that the migration energy barrier decreased from 1.6 to 0.8 eV when oxygen vacancy was introduced to delithiated $Li_{0.5}NiO_2$ phase (Figure 1.3.1e). This indicates that an oxygen vacancy opens a new cation migration path. Therefore, it seems reasonable that Li-Ni cation disorder should be observed regardless of the particle position on thermodynamic terms. However, this was not true according to the numerous reports, in which a cation mixing has been observed only on the particle surface. To investigate the reasons, they have focused on the kinetic issue of the oxygen migration and have calculated that an oxygen migration is kinetically prohibited in the bulk even though the oxygen evolution is thermodynamically possible (Figure 1.3.1f) This is because there is no open space for the

evolved oxygen to move out from inner bulk to outer surface. In the case of surface, together with the open space for oxygen migration and possibility to react with the electrolyte, the surface oxygen is kinetically much more favorable to migrate and evolve into O_2 gas, eventually leading to the surface reconstruction layer.

Interestingly, Zhu et al. have showed that the cation mixing behavior depended on the orientation of the facets, where the lithium diffusion path channels (for example, <001> direction) were more prone to go under phase transformation than the other planes (Figure 1.3.1g) [45]. This behavior suggests that the phase transformation is promoted by the lithium removal during charge process, while it becomes more severe in the regions that undergo the dynamic lithium transport. Furthermore, Sharifi-Asl et al. have showed that the oxygen evolution is highly dependent on facet orientation of layered cathodes by Ab initio molecular dynamics simulation (AIMD) [46]. By comparing [001], [012], and [104] facets, the calculations showed that oxygen was most stable in [001] plane for both pristine and delithiated states (Figure 1.3.1h). As the oxygen atoms are under-coordinated in [012] and [104] facets, they are usually coordinated to one TM ion and one lithium ion. However, they become coordinated to only one TM ion under delithiation condition. Thus, two neighboring under-coordinated oxygen atoms oscillate to become bonded and eventually evolved as oxygen gas. As mentioned previously, the oxygen evolution can highly trigger the TM ion migration toward Li slab by Kong's report. In terms of this theory, the facet dependent cation mixing behavior and facet dependent oxygen evolution behavior are highly linked. As the oxygen gas is more prone to be released for the lithium diffusion facet such as [012] and [014] compared to [001] facet, the evolution of gas for those facets would kinetically induce more severe cation mixing behavior, thus leading to the anisotropic behavior of surface reconstruction layer. Overall, it is postulated that cation mixing, which is one of the major degradation mechanisms of NCM,

seems to be highly linked with the oxygen instability on the particle surface.

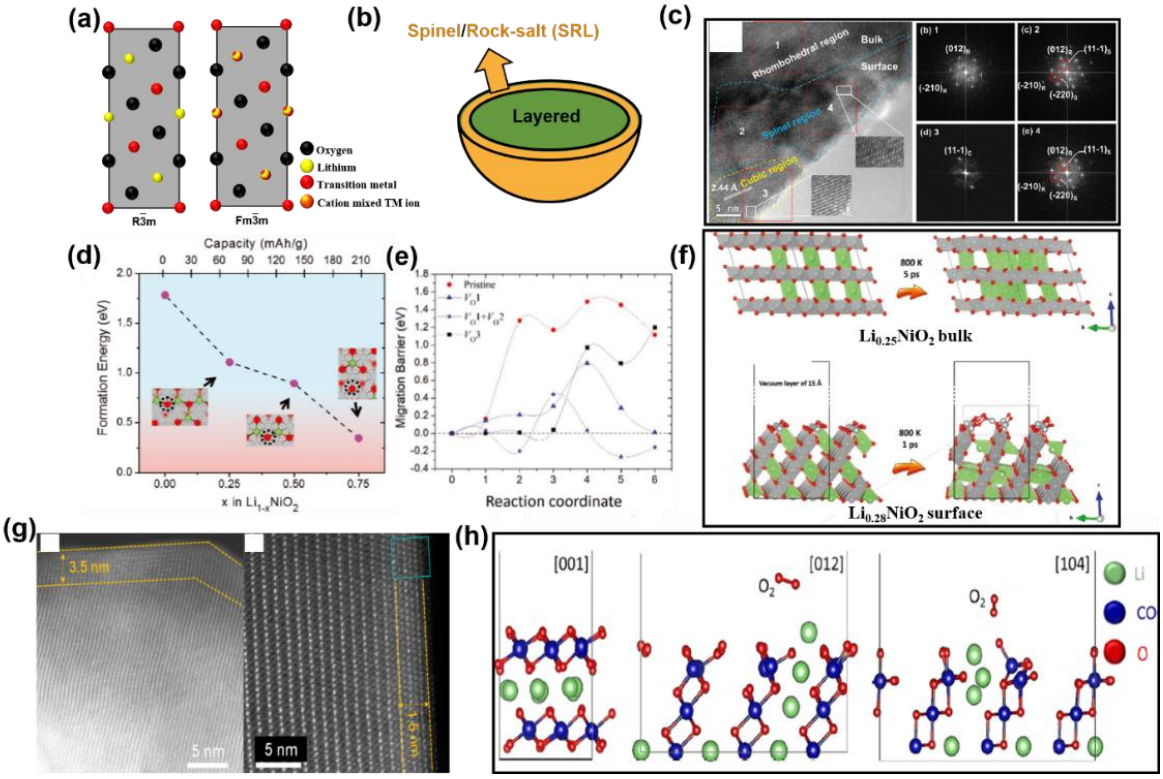

Figure 1.3.1. (a) Illustration of disordered phase in lithium layered oxide, (b) schematic figure for the formation of surface reconstruction layer (SRL), (c) TEM analysis of cycled NCM523. Reproduced with permission [43]. Copyright 2013, Wiley. (d) calculated oxygen vacancy formation energy during delithiation of $LiNiO_2$ (LNO), (e) Ni migration energy barrier for the delithated LNO, (f) atomic kinetics comparison between particle surface and bulk of charged LNO. (d, e, f) Reproduced with permission [44]. Copyright 2019, Wiley, (g) STEM imaging of cycled NCM. Reproduced with permission [45]. Copyright 2020, American Chemical Society, and (h) dependence of thermal stability on particle orientation of charged $LiCoO_2$ calculated. Reproduced with permission [46]. Copyright 2017, American Chemical Society.

1.3.2. Vulnerable thermal characteristics

The thermal stability of NCM is one of the major concerns for the battery industry as it is directly related to the battery safety issue especially when cycled at high temperature. The instability of synthesized pristine NCM or lithiated NCM is of no concern as they are safe even under high-temperature condition [2]. However, it becomes highly unstable when lithium is extracted from the structure (delithiated NCM) and becomes more severe under highly overcharged state. The oxygen gas is released when heated above 200 ºC (onset temperature depends on SOC and Ni content) and can ignite violently with an explosive reaction with a highly flammable electrolyte [7]. The oxygen release of the NCM inevitably coincides with the structure transformation, where the phase transition starts from the surface and migrates toward the inner bulk. Nam et al. systematically investigated the thermal stability of charged Ni-rich layered oxide (SOC: ~70%) via *in-situ* time resolved XRD (TR-XRD) with mass spectroscopy (MS) attached [47]. During heating, they have found that two distinct peaks for O_2 gas evolution were detected via MS and the center of the peaks were around 230 and 300 ºC, respectively (Figure 1.3.2a). From the TR-XRD, the structure transitions from initial layered structure (R-3m) toward spinel structure (starts at 180 ºC) and lastly to NiO-like rock-salt structure (starts at 250 ºC) were observed. This is because the oxygen gas evolution inevitably accompanies with the phase transition based on the following equations

$Li_{0.33}TMO_2$ (layered, R-3m) → $Li_{0.33}TMO_{1.77}$ (spinel, Fd-3m) $+0.115O_2\uparrow$,

$Li_{0.33}TMO_{1.77}$ (spinel, Fd-3m) → $Li_{0.33}TMO_{1.33}$ (rock-salt, Fm-3m) $+0.22O_2\uparrow$.

To unveil what transition metal was responsible for the structure transformation during heating, *in-situ* X-ray absorption near edge structure (XANES) measurement was conducted (Figure 1.3.2b). The absorption pre-edge peak (A) is associated with the dipole-forbidden 1s→

3d electronic transition for each transition metal, while the main peaks (B, C) are associated with the transition of 1s core electron to unoccupied 4p state. Therefore, the intensity of pre-edge peak is related to the number of transition metal occupying the tetrahedral sites, while the main peak shift is related to the valence state of transition metals. By observing the K-edge XANES spectra of transition metals during heating, the main peak energy shift toward a low energy was most severe for Ni K-edge, while Mn K-edge was very stable (Figure 1.3.2c). As the energy shift towards the low energy in XANES spectra indicates the reduction of TM valence state, the severe energy shift of Ni K-edge indicates that Ni is the most unstable species when the battery is heated. The onset temperature of the energy shift for Ni well corresponds with MS or TR-XRD result, where oxygen gas evolution or phase transformation also accompanied with the reduction of the Ni (Figure 1.3.2c). For Co K-edge XANES, the main energy peak shift was not severe compared to Ni K-edge, while the pre-edge peak intensity substantially increased with increasing temperature. This indicates that cobalt continuously transits from octahedral site to tetrahedral site during heating process, thus forming Co_3O_4-type spinel phase.

As stated previously, the Ni-rich cathodes with Ni content above 80% are receiving great interest for industrial demand and have advantages on allowing higher practical capacity on the fixed voltage (above 200 mAh g^{-1} when charged to 4.3 V vs Li/Li^+). This indicates that Ni-rich NCMs are in higher SOC state compared to Ni-low NCM at same charge voltage and thus, most of the Ni is in valence state of 4+. As the Ni^{4+} (electronic configuration: $t_{2g}^6e_g^0$) is highly unstable due to empty e_g band and is prone to react with the electrolyte, the thermal stability of charged NCM decreases with increasing Ni content. Bak et al. found that increasing the Ni content on NCM lowered the onset temperature of phase transformation as well as increasing the amount of released oxygen [48]. For NCM532, the oxygen evolution as well as structure

transformation started at high temperature of 235 ºC, while the onset temperature was lowered to 185 ºC for NCM622 and 135 ºC for NCM811 (Figure 1.3.2d).

To make things worse, the residual lithium impurities on Ni-rich NCM surface further contribute to the vulnerable thermal characteristic [49]. The most common employed method to synthesize NCM is by solid-state method, in which NCM precursors are mixed with lithium source and subsequently calcined. The calcination temperature depends on Ni-content of NCM and a lower temperature is normally required for Ni-rich cathode. For example, NCM622 is synthesized above 800 ºC while LNO is synthesized below 700 ºC [50]. This is because Ni-rich NCM is unstable at high temperature and tends to decompose and to give off-stoichiometric $Li_{1-z}TM_{1+z}O_2$. However, even though stoichiometric Ni-rich NCM can be synthesized at low temperature, unreacted lithium precursor remains as impurities. This lithium residual reacts with air and moisture in atmosphere to form the passivation layer (mainly composed of LiOH, Li_2CO_3, Li_2O, and Li_2O_2) on the NCM particle surface (Figure 1.3.2e). These lithium residuals impact the electrochemical properties of NCM due to their insulating characteristics, which build up the electrode impedance. It has been confirmed that Li_2CO_3 on the particle surface can react with $LiPF_6$ in the electrolyte to accelerate the dissolution of transition metals of NCM [51, 52]. From the XPS depth profile on the cycled layered cathode, the amount of TM on the surface was lower than the bulk, which indicates that TM has been etched away during cycling (Figure 1.3.2f). The dissolved transition metals migrated from cathode to anode site (so called “transition metal cross-talk”), which could induce a short-circuit between cathode and anode to provoke the explosive reaction (Figure 1.3.2g, h). Also, the transition metal migration acts as a catalyst to trigger the unstable solid-electrolyte-interphase (SEI) layer on the anode material, leading to the degradation of electrochemical performance for both cathode and anode. Furthermore, it has been reported that the residual

lithium can be electrochemically oxidized during charge process (around 4.1 V vs Li/Li^+) or react with the electrolyte solvent to form carbon dioxide gas, which arises the thermal safety issue. The residual lithium can be diminished by washing process, however, which leads to the poor cycle performance. Overall, the increase of energy density in lithium ion batteries by adopting the Ni-rich NCM cathode cannot avoid the thermal-stability issue.

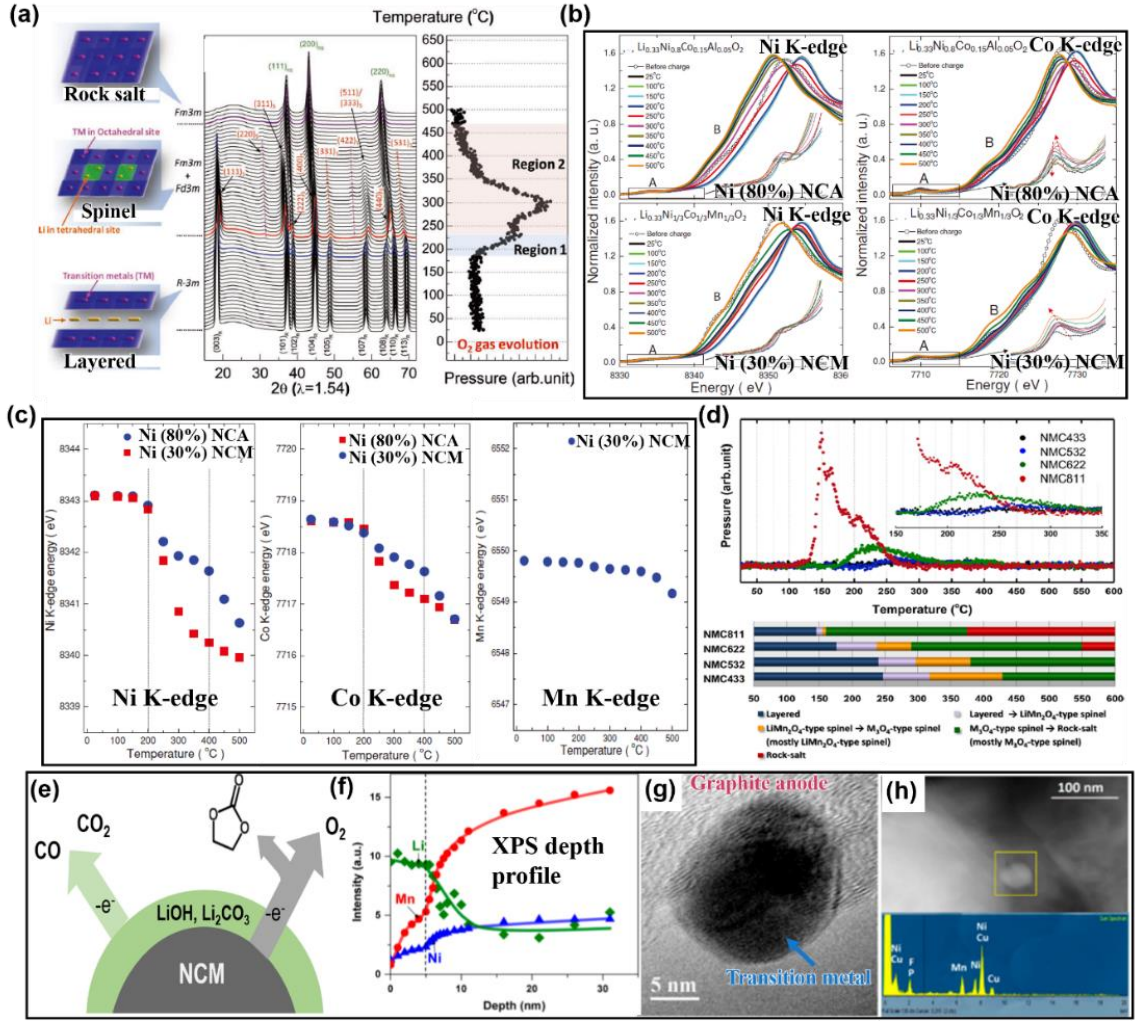

Figure 1.3.2. (a) TR-XRD patterns and simultaneously measured mass spectra (MS) for the charged $Li_{0.5}Ni_{0.8}Co_{0.15}Al_{0.05}O_2$ layered oxide, (b) K-edge XANES spectra of Ni and Co for the charged NCM and NCA during heating, (c) variation of transition metal K-edge position as a function of temperature. (a, b, c) Reproduced with permission [47]. Copyright 2013, Wiley, (d) mass spectroscopy profile for the $LiNi_xCo_yMn_zO_2$ (x=0.4, 0.5, 0.6, 0.8) during heating. Reproduced with permission [48]. Copyright 2014, American Chemical Society, (e) shematic illustration of the residual lithium on the NCM particle, (f) XPS depth profile for the cycled layered cathode, and (g), (h) TEM imaging of transition metal cross-talk on the graphite anode. (f, g, h) Reproduced with permission [51]. Copyright 2013, American Chemical Society.

1.3.3. State-of-charge heterogeneity

Due to the insufficient time for electron or Li ion to diffuse and progress along the micrometer sized secondary particles, non-equilibrium lithium distribution on the particle upon delithiation leads to the SOC heterogeneity within the NCM individual secondary particles. Such SOC heterogeneity can generate the local overcharge domains within the particles, which accelerate the release of oxygen, fasten the transition migration toward Li slab, and generate the stress to accelerate the particle fracture. Gent et al. have showed that during charge, the local lithium content varied over 10% for NCM333 even after 10 h of extensive relaxation process (Figure 1.3.3a) [40]. As expected, SOC heterogeneity becomes more severe with increasing the amount of lithium extraction from the NCM structure. Surprisingly, the reduction of the charge current rate from 1.1C to C/110 or increasing of the relaxation time from 10 to 170 h did not lower the SOC heterogeneity within the secondary particles (Figure 1.3.3b). The authors suggested that this kind of heterogeneity is not caused by the Ni-Co-Mn compositional non-uniformity in the synthesized NCM, but affected by the NCM morphology, which is consisted of primary particles aggregated to micrometer sized secondary particle. However, before drawing the firm conclusion, what one should consider is that electrochemical inactive components are present in the electrode. As these inactive components, such as conductive carbon or binder, have the electronic/ionic effect on the NCM particles, there is a possibility that this might have affected the SOC heterogeneity during electrochemical delithiation process. Therefore, Tian et al. have chemically delithiated the NCM 622 using NO_2BF_4 as an oxidant to observe the contribution of inactive components on the SOC heterogeneity (Figure 1.3.3c) [53]. From the results, it showed that the degree of heterogeneity was similar regardless of delithiation process by chemical or electrochemical way, confirming that inactive components in the electrode does

not affect the heterogeneity. Recently, it has been reported that the crystallographic orientation of primary particle can affect the SOC heterogeneity. Xu. et al. have prepared the two NCM particles which have similar chemical composition, crystal structure, and electronic structure, however, only differing in crystal orientation (Figure 1.3.3d) [54]. The road-NCM primary particle is shaped with the lithium channel along the radial orientation which could favor the lithium transport, while gravel-NCM primary particle is randomly oriented with no texture. Even though both NCM showed the similar specific capacity during first cycle, the deterioration of cell and increase of polarization were much faster for gravel-NCM compared to road-NCM. To investigate the reason, three-dimensional (3D) TXM was used to probe the variation of Ni valence within the primary particle. The 2D nanodomain valence gradient vectors are most parallel to each other for road-NCM and aligned in the radial direction, while the gradient vectors were randomly distributed in the case of gravel-NCM (Figure 1.3.3e). This indicates the SOC heterogeneity was relatively small for road type compared to gravel type, which suggest that the crystallographic orientation could actually influence the lithium ion mobility to reduce the SOC heterogeneity and eventually enhance the cycle performance.

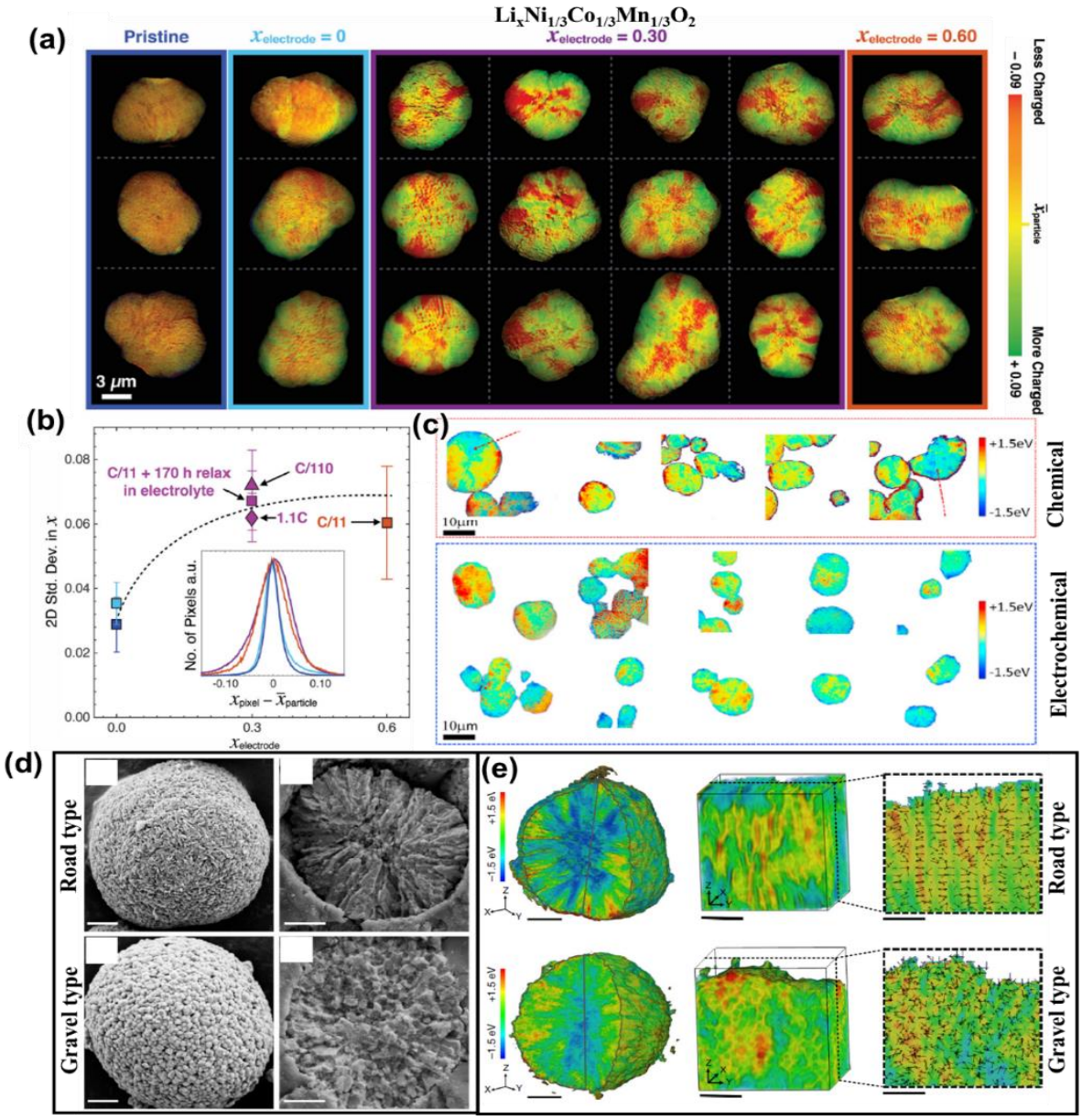

Figure 1.3.3. (a) State of charge (SOC) heterogeneity maps of charged NCM333 obtained by imaged *ex situ* Ni K-edge spectra, (b) Average lithium fraction of charged NCM depending on the current rate and relaxation time. (a, b) Reproduced with permission [40]. Copyright 2016, Wiley, (c) SOC maps of chemically delithiated and electrochemically delithiated NCM622. Reproduced with permission [53]. Copyright 2018, Cell Press, (d) SEM images of road and gravel type NCM and (e) SOC maps of road and gravel type charged NCM. (d, e) Reproduced with permission [54]. Copyright 2020, Springer Nature.

1.3.4. Intergranular cracks

In general, NCM particles are synthesized through the co-precipitation method. When the particles are produced via this method, it is consisted of primary particles which are aggregated to micrometer sized secondary particles [4]. During charge process, Ni-rich NCM goes under multiple phase transitions (H1 phase→M phase→H2 phase→H3 phase), which could be verified by dQ dV^{-1} profiles and *in-situ* XRD [55]. Specifically, the $(003)_{H1}$ peak smoothly shifts toward a lower 2θ upon charging and completely evolves into $(003)_{H2}$ in the voltage range of 4.1~4.2 V (Figure 1.3.4a). The shift of (003) peak to the low-angle indicates the lattice expansion in c-axis direction, which is attributed by the oxygen-oxygen repulsion within the Li-slab as the screening effect by lithium ion has been diminished [56]. However, during the phase transition from H2 to H3, (003) peak swiftly moves toward the high angle which leads to the sudden lattice shrinkage (about ~5%) on c-axis direction. Compared to c-axis, a-axis continuously decreases because of the increase in electrostatic attraction caused by nickel oxidation during delithiation [13]. Thus, this anisotropic lattice change during cycling induces the stress between the primary particles, eventually leading to "intergranular cracks". As the electrolyte penetrates through the cracks, the direct exposure of freshly formed in-grain primary particle with the electrolyte leads to the unwanted reactions, such as cation mixing or electrolyte decomposition [57]. Furthermore, the electrolyte infiltration through the cracks shortens the lithium ion diffusion path but not for the electron diffusion length due to the loss of electrical contact between primary particles via cracks. This results in the electronic and ionic conductivity mismatch, which increases the SOC heterogeneity between the particles that could potentially develop more morphological damage [58]. This type of behavior has been rarely found in Ni-low NCM, but typically observed in Ni-rich NCM. Therefore, many studies

have focused on this specific phenomenon only in Ni-rich NCM. For instance, Ryu et al. have compared the NCM crack behavior during cycle depending on Ni content ($LiNi_xCo_yMn_{1-x-y}O_2$, $0.6<x<0.95$) [59]. The cyclability decreased with increasing Ni content, in which NCM622 retained 97% of its original capacity after 100^{th} cycles while LNO only retained 75% of its original capacity (cycled between voltage of 2.7-4.3 V vs Li/Li^+) (Figure 1.3.4b). From the $dQ\ dV^{-1}$ profiles (Figure 1.3.4c), H2→H3 phase transition (the phase transition occurs at 4.2 V vs Li/Li^+) was observed for Ni-rich NCM and *in-situ* XRD verified the sudden c-axis lattice collapse contributed by the H2→H3 phase transition (Figure 1.3.4d). The cross-sectional polishing SEM images of NCM at 4.3 V charged states showed that intergranular cracks became severe with increasing Ni content (Figure 1.3.4e), which verifies that the H2→H3 phase transition is responsible for the crack contributor. Thus, it seemed that intergranular crack is a degradation phenomenon that only contributes to the Ni-rich NCM. However, Li et al. have recently discovered that the lattice collapse is a universal phenomenon that depends on the SOC (utilization of Li during delithiation) rather than Ni content (Figure 1.3.4f) [60]. The researchers have selected the NCMs with different Ni-content (Ni: 33%, 50%, 70%, and 90%) to show the fact. When NCMs were electrochemically charged at the voltage of 4.4 V vs Li/Li^+, the 4 NCMs delivered the different capacity, where the specific capacity increased with increasing Ni content. By *in-situ* XRD, the sudden c-axis contraction was only observed for Ni-rich cathode (Ni: 90%). However, when the 4 NCMs were charged to 80% of SOC (5.01 V-Ni (33%), 4.94 V-Ni (50%), 4.81 V-Ni (70%), 4.49 V-Ni (90%)), the sudden lattice change were observed regardless of Ni-content in NCMs. Thus, this indicates that Ni-rich NCMs do not necessarily possess fundamentally inferior electrochemical stability compared to Ni-low NCM, however, the degree of lithium utilization (SOC) is often the deciding parameter. There is still a debate why this lattice contraction occurs during H2→H3 phase transition. For one

opinion, the induction of charge-transfer between oxygen and transition metal has been suggested [61]. In detail, Kondrakov et al have discovered the oxygen pre-edge peak increased during H2→H3 phase transition by soft X-ray absorption spectroscopy (sXAS), while c-axis shrinkage was mainly attributed by the collapse of Li-slab rather than TM-slab. Based on bader charge, it has been discovered that the effective oxygen charge increased from -1.2 ($Li_{0.5}NiO_2$) toward -0.8 ($Li_{0.25}NiO_2$) during H2→H3 phase transition (Figure 1.3.4g), which is an indication of negative charge transfer from oxygen 2p orbital to partially filled e_g orbitals of nickel, eventually leading to the decrease of electrostatic repulsion within the Li-slab and thus, the lattice collapse of Li-slab.

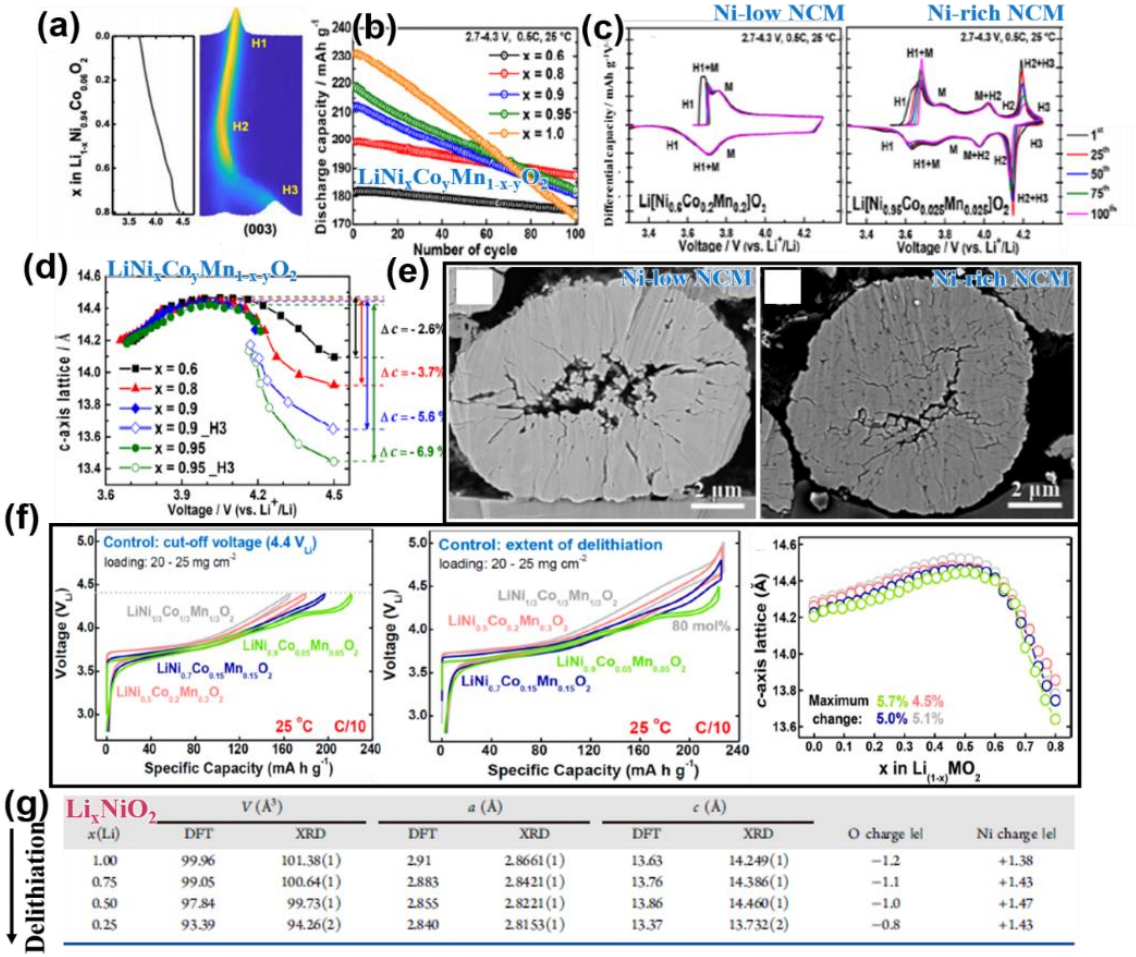

Li_xNiO_2	V (Å³)		a (Å)		c (Å)			
x(Li)	DFT	XRD	DFT	XRD	DFT	XRD	O charge |e|	Ni charge |e|
1.00	99.96	101.38(1)	2.91	2.8661(1)	13.63	14.249(1)	−1.2	+1.38
0.75	99.05	100.64(1)	2.883	2.8421(1)	13.76	14.386(1)	−1.1	+1.43
0.50	97.84	99.73(1)	2.855	2.8221(1)	13.86	14.460(1)	−1.0	+1.47
0.25	93.39	94.26(2)	2.840	2.8153(1)	13.37	13.732(2)	−0.8	+1.43

Figure 1.3.4. (a) *In-situ* XRD plot of layered cathode during charge. Reproduced with permission [55]. Copyright 2019, American Chemical Society, (b) cyclability comparison of $LiNi_xCo_yMn_zO_2$ (x=0.6, 0.8, 0.9, 0.95, 1), (c) dQ/dV plot of Ni-low (x=0.6) NCM/Ni-rich NCM (X=0.95), (d) c-axis lattice parameter of $LiNi_xCo_yMn_zO_2$ (x=0.6, 0.8, 0.9, 0.95, 1) as a function of cell voltage, (e) cross-sectional SEM image of cycled Ni-low (x=0.6) NCM/Ni-rich NCM (X=0.95). (b, c, d, e) Reproduced with permission [59]. Copyright 2018, American Chemical Society, (f) comparison of galvanostatic graph and variation of c-axis lattice parameter depending of Ni content of NCM. Reproduced with permission [60]. Copyright 2019, American Chemical Society, and (g) Badar charge calculation of Li_xNiO_2 during delithiation process. Reproduced with permission [61]. Copyright 2017, American Chemical

1.3.5. Intragranular cracks

Even though the theoretical models predict the grain boundary as the preferred sites for crack initiation, the cracks within each grain interior have also been observed. The so called "intragranular crack" is best observed when NCM is cycled at high voltage (>4.7 V vs Li/Li^+) or high temperature (>150 ^oC) [42, 62]. As the intragranular cracks can generate more freshly exposed surface to the electrolyte compared to the intergranular cracks because of its high-density characteristics, the mitigation of this issue is essential for high-performance NCM. However, the comprehensive information of crack behavior or preventive method to suppress the intragranular crack has not yet been clearly suggested. To date, Yan et al. have observed that minor intragranular crack was formed when NCM622 was charged up to 4.8 V vs Li/Li^+, while the cracks were propagated and expanded when delithiated NCM was thermally heated (Figure 1.3.5a) [62]. All intragranular cracks followed a strict crystallographic preference along the (003) plane, and the edge dislocations acted as a nucleation site (Figure 1.3.5b). This is because the primary particle which is often considered as a single crystal, is in fact polycrystalline that contains a low-angle grain boundary. Therefore, it was discovered that the cracks were initiated from the grain interior, which was the sharp contrast with the general belief that the crack might propagate from the grain boundaries or open surface. From the selected area diffraction pattern (SAED), spinel phase was observed at the free surfaces of cracks (Figure 1.3.5c), while the depletion and evolution of oxygen was observed along the cracks by EELS measurement (Figure 1.3.5d). Therefore, the research team have concluded that material phase heterogeneity (between rock-salt phase and layered phase) with the buildup of internal pressure associated with oxygen evolution was the two major driving forces for the intragranular crack propagation along the (003) plane. Mu et al. suggested that oxygen release

was the main driving factor for the initiation and propagation of intragranular crack [63]. Upon release of oxygen on the surface of primary particle, compressive stress is generated on the particle surface while tensile stress is formed in the particle center (Figure 1.3.5e). Thus, the tensile stress inside the primary particle initiates and propagates the unstable radial crack in NCM grains. Besides the intragranular cracks, the presence of intragranular pore has been observed [64]. Ahmed et al. have found that the nanopore was present inside the primary particle even in the pristine state of $LiNi_{0.85}Co_{0.1}Mn_{0.05}O_2$, while the diameter of pore increased during cycling operation (Figure 1.3.5f). A rock-salt region around the nanopore boundaries increased with progressive cycling (Figure 1.3.5g), while the O K-edge in EELS showed the formation of oxygen vacancy within the nanopore (Figure 1.3.5h). As these nanopores could act as a nucleation site for intragranular crack, the two defects could synergistically combine to deteriorate the NCM electrochemical performance.

To summarize, the fading mechanisms of NCM cathodes are classified as Li-Ni disorder on the particle surface, vulnerability of oxygen release, residual lithium impurities, state-of-charge heterogeneity within the particle, and nano/micro cracks during cycling. Previously, these mechanisms have been perceived as an independent phenomenon, which concurrently operates during battery cycling. However, the systematic study in this review suggests that the degradation factors are in fact highly co-linked. Upon high SOC, oxygen gas is susceptible to be released on the particle surface, which opens a new Ni migration pathway toward Li slab and also induces the mechanical stress that could act as a nucleation site for intergranular/intragranular crack. Furthermore, the mechanical cracks lead to the electronic and ionic conductivity mismatch during lithiation/delithiation, which increases the SOC heterogeneity that could potentially induce more severe mechanical damage. Therefore, to truly propose and develop the design strategy to solve the deterioration of NCM cathodes, the

fundamental finding of the degradation mechanism correlation has to be preceded beforehand.

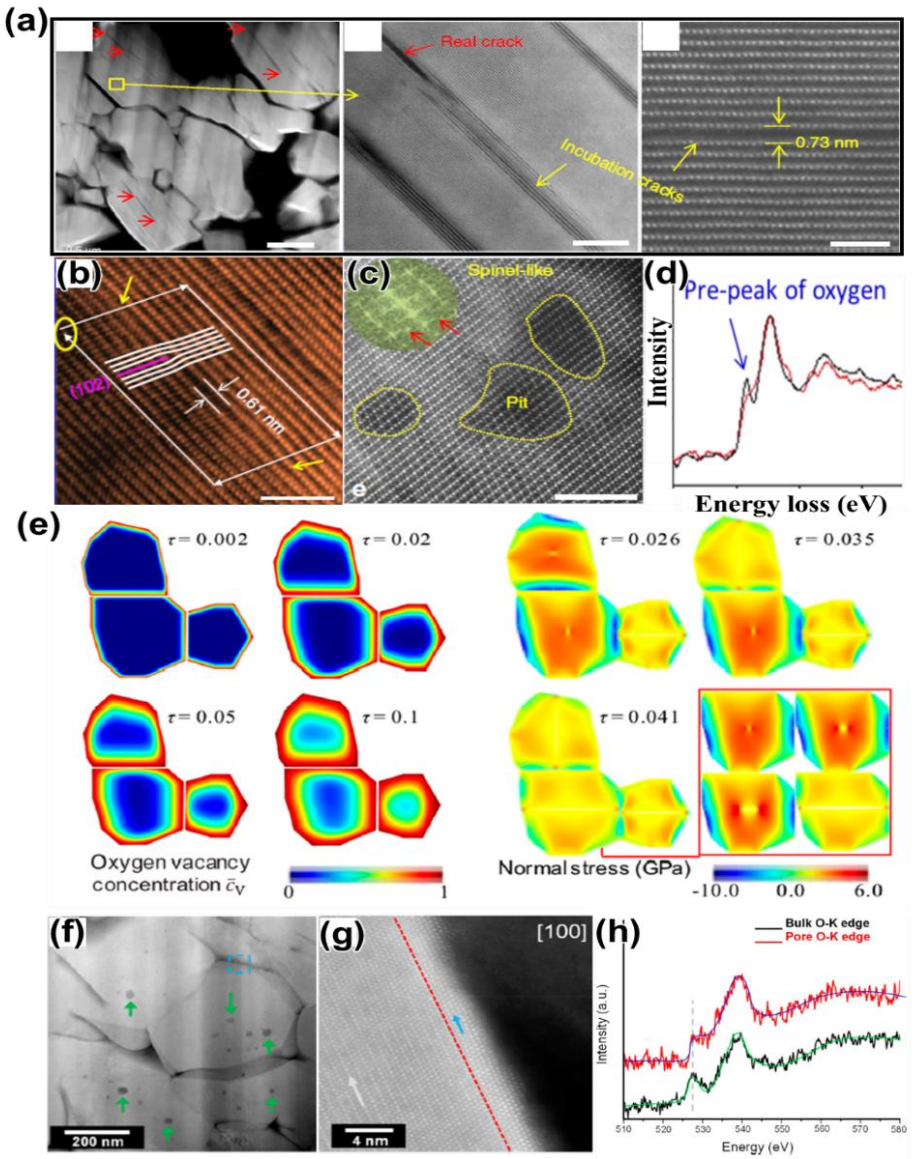

Figure 1.3.5. (a) Cross-sectional HADDF images of cycled NCM622, (b) intragranular crack formation along the (003) plane, (c) HADDF imaging and (d) EELS analysis showing the phase transformation around the intragranular crack. (a, b, c, d) Reproduced with permission [62]. Copyright 2018, Springer Nature, (e) Finite element modeling (FEM) model of NCM. Reproduced with permission [63]. Copyright 2018, American Chemical Society, (f) presence of nanopore inside NCM, (g) HADDF imaging and (h) EELS analysis showing the phase transformation around the nanopore. (f, g, h) Reproduced with permission [64]. Copyright 2019, American Chemical Society.

1.3.6. Brief overview on characterization techniques to observed NCM degradations

To unveil the reasons for the continuous capacity fading of NCM during multiple cycles, various ex-situ/in-situ multi-length-scale X-ray spectroscopic techniques, microscopic imaging, and gas analysis have been utilized (Figure 1.3.6a). To visualize the cation-mixing which occurs in nanometer length scale, a "high-angle annular dark field scanning TEM (HAADF-STEM)" is widely used technique that can clearly detect the Ni migration toward the Li-slab (Figure 1.3.1g). Besides the STEM analysis, the (003)/(104) intensity ratio from the XRD measurement can also be utilized to detect the degree of cation-mixing (Figure 1.3.6b) [65]. In case of oxygen gaseous release, an "*Operando* differential electrochemical mass spectrometry (DEMS)" experiment is one of the state-of-the-art analysis that can monitor and quantify the gas evolution during cycling (Figure 1.3.6c) [66]. During charge/discharge process, DEMS can detect O_2 gas as well as accompanying CO_2 gas in real time. The evolution of O_2 gas leaves the oxygen vacancy within the NCM crystal structure that can be measured by "electron energy loss spectroscopy (EELS)" analysis (Figure 1.3.5d). In EELS spectra, the excitation of an O1s shell electron to unoccupied hybridized TM3d-O2p orbitals rises the O K-edge spectrum, which can be used to detect the valence state change of oxygen [62, 64]. Furthermore, "*ex-situ/in-situ* X-ray absorption near-edge structure (XANES)" measurement can be used to trace the TM oxidation state variation that is resulted from the cation-mixing/oxygen-release (Figure 1.3.2b). The XANES K-edge spectra provides the valuable information regarding to the average TM valence state and the site-symmetry variation around the absorbing atoms. [9, 48] For the bulk degradation, which is induced by the sudden lattice collapse along the crystallographic c-axis direction, a "cross-section polishing SEM (CP-SEM)" imaging can

visualize the intergranular cracks between the primary particles (Figure 1.3.4e). However, CP-SEM cannot be used to observe the intragranular cracks as its phenomenon occurs in nanometer length scale and thus, STEM is used as a tool in case of intragranular cracks. To observe the crystallographic lattice variation during lithiation/delithiation process, "*in-situ* XRD" measurement can be used to trace the NCM phase transition during cycling in real time (Figure 1.3.4a). As the harsh oxygen/moisture environment can influence the sample status (due to the highly unstable characteristics of charged NCM) during *ex-situ* XRD measurement without an extra precaution [17, 24, 33], *in-situ* XRD analysis should be used to accurately detect the lattice variation during charge process.

As state above, various analysis techniques can be used to detect the NCM degradation factors starting from nano-surface to micro-bulk. With the development of analytic techniques, it is believed that the other NCM degradation factors we might have missed out can be discovered. For instance, before the introduction of HADDF-STEM, the cation mixing in NCM particles was only able to be observed by fast Fourier transform (FFT) patterns or diffraction patterns, which indirectly probed the phase transformation from layered oxide to rock-salt phase (Figure 1.3.1c) [43]. However, as STEM analysis can visualize the specimen in atomic-scale, we now can directly visualize the Ni-migration toward the Li-slab that leads to the cation-mixing (Fig. 2g) [45]. The nowadays spotlighted analysis tool might be "mapping of resonant inelastic X-ray scattering (mRIXS)" (Figure 1.3.6d), which is demonstrated as a tool-of-choice for visualizing the valence-state change of lattice oxygen in both Li- and Na-ion battery electrodes [67, 68]. Especially, the mRIXS measurements have gained much attention in the field of Li-rich LIB cathodes, which was successfully applied to demonstrate the oxygen redox mechanism. The mRIXS analysis is further expanding its applications toward the Ni-rich layered cathodes [69]. By using the methodology, we believe "oxygen charge transfer"

mechanism, which was proposed by Kondrakov et al as stated in "1.3.4 Intergranular cracks section", can be demonstrated by the use of state-of-the-art mRIXS analysis.

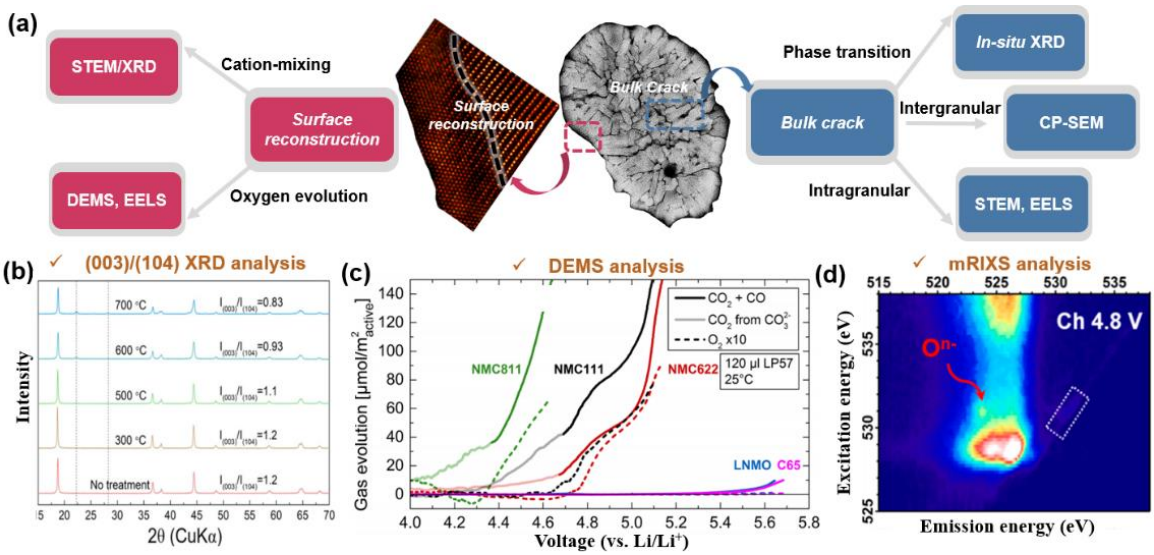

Figure 1.3.6. (a) Schematic on illustrating the characterization techniques for observing the NCM degradation factors, (b) XRD profile to observe the degree of cation mixing by using (003)/ (104) intensity ratio. (b) Reproduced with permission [65]. Copyright 2020, Wiley. (c) *Operando* differential electrochemical mass spectrometry (DEMS) analysis for the LIBs cathode materials. (c) Reproduced with permission [66]. Copyright 2017, American Chemical Society. (d) Mapping of resonant inelastic X-ray scattering (mRIXS) analysis to observe the oxidized oxygen. (d) Reproduced with permission [69]. Copyright 2019, American Chemical Society.

1.4. Aim and strategies

To date, various strategies have been suggested to resolve the various deterioration factors of Ni-rich NCM cathodes which we had explained above. The representative strategies include bulk doping, surface coating as well as other methods such as core-shell design. The previous reviews have well discussed the various strategies with respect to the electrochemical and thermal enhancement [1, 2, 7, 14]. However, the relationships between strategies and resolved deterioration factors have not been fully elucidated.

In this review, we will discuss the recent progress of the different strategies focusing on the correlation between strategies and resolved degradation factors. Overall, this section is divided into 4 sub-sections of “bulk doping”, “coating”, “other methods”, and “brief summary on the relationship between the proposed strategies and deterioration mechanisms”. In the “1.4.3 other method” section, we will introduce four different strategies of core-shell structure, single-crystal, gradient doping, and epitaxial layer coating, which effectively enhanced the NCM property by different mechanisms. In the last section, we will elucidate the correlation between the deterioration factors and the various proposed strategies.

1.4.1. Bulk doping

Bulk doping for NCM materials has been extensively researched to solve the issues we had summarized in the previous section [70-73]. The element dopants may either replace the TM or the Li in the crystal structure of NCM to enhance the structural stability as well as cycling performance. However, the proposed mechanism behind the improvements varies for each dopant, and one element may solve the multiple degradation factors of the NCM

simultaneously. Therefore, we will discuss each doping strategy according to the deterioration factor they resolve including cation mixing, electrode/electrolyte side reactions, thermal instability, and crack formation. One should note that, to the best of our knowledge, doping strategy focused on resolving the SOC heterogeneity within the NCM cathodes has not been reported.

"Cation mixing", which occurs by the migration of Ni^{2+} from TM-slab toward Li-slab, reconstructs the surface of NCM that could impedes the lithium ion conductivity during cycling [37]. In order to mitigate the cation mixing, the low valence element (Na^{+} and K^{+}) as well as high valence element (Zr^{4+} and Ti^{4+}) doping was conducted [70-73].

Dopants, such as Na and K, which have a similar or slightly larger size compared to the Li ion (Li^{+}: 0.76 Å, Na^{+}: 1.02 Å, K^{+}: 1.38 Å) occupy the Li layer when doped into the crystal lattice [70, 71]. The inlaid dopant materials in the Li slab develop a driving force that separates the TM layer from the Li ions during synthesis procedure, which reduces the cation mixing for the pristine electrode (Figure 1.4.1a) [74]. Xie et al. showed the reduced cation mixing by Na doping into NCA 811 [70]. The Rietveld refinement results revealed that the 1% concentration of Ni in the Li site decreased to 0.57% after Na doping. Additionally, the Na ions occupying the Li slab enlarged the Li layer and thus increased the Li diffusion. As a result, the reduced cation mixing of Na-doped NCA 811 lead to a higher capacity retention of 90.71% after 200 cycles at 1 C compared to the 80.46% capacity retention of undoped NCA 811.

With a similar mechanism to Na, K was also reported to reduce the cation mixing during synthesis. The K and Cl dual doped NCM 523 was prepared by Chen et al. via a solid state reaction to simultaneously utilize the different roles of each dopant [71]. The K and Cl were substituted for Li and O, respectively, in the crystal structure. The large K ion in the Li slab reduced the initial cation mixing by 0.53% while the strong ionic bonding between Cl and TM

enhanced the overall structural integrity of the crystal structure. As a result, the initial capacity and the rate performance was greatly improved after dual doping.

Unlike the low valence dopants, the high valence dopants such as Ti and Zr occupy the TM site that could also reduce the cation mixing level from pristine to cycled state [72, 73]. Qiu et al demonstrated a reduced cation mixing degree for the pristine state of NCA 811 after Ti doping [72]. The Rietveld refinement revealed a cation mixing degree of 4.74% and 1.34% for undoped NCA 811 and Ti-doped NCA 811, respectively. The reason to the lower cation mixing degree of the Ti-doped NCA is because Ti is an early TM which has a d orbital that is more delocalized than the Ni, Co, and Mn [72]. Thus, Ti^{4+} can strengthen the metal-metal bonding as well as metal-oxygen bonding, which can aid in suppressing the Ni^{2+} migration toward the Li-slab.

Zr doping reduces the cation mixing level of the after cycled cathode by a rather extraordinary way [73]. According to the density functional theory calculations (DFT calculations) conducted by Choi and co-workers, Zr dopants initially occupy the TM site when substituted into the NCM crystal structure. However, after the NCM cathode is fully delithiated, Zr ions migrate from the TM slab to the tetrahedral site of the Li slab. As the cation mixing occurs by the migration of Ni ions from the TM slab octahedral site → Li slab tetrahedral site → Li slab octahedral site in sequence, the Zr ions placed at the tetrahedral site of the Li slab can block the pathway of Ni ions moving toward the Li slab octahedral site, therefore effectively repressing the cation mixing during delithiation process [75]. After 100 cycles, high-angle annular dark field scanning TEM (HAADF-STEM) revealed that undoped NCM 622 showed the cation mixed layers on the surface even at the pristine state and the cation mixed layers severely propagated toward the bulk after cycling (Figure 1.4.1b). In contrast, the Zr-doped NCM 622 well preserved the layered structure even after cycling. Although there was a slight

decrease of initial discharge capacity due to the incorporation of electrochemical inactive Zr, Zr-doped NCM 622 exhibited a high capacity retention of 98.4% after 100 cycles at 0.1 C, while the capacity retention of undoped NCM 622 was only 83.7%.

Upon the delithiation of NCM, the highly reactive Ni^{4+} tends to react with the electrolyte, which accompanies oxygen evolution and surface reconstruction [37, 38]. “In order to protect the cathode material from the hazardous reactions with the electrolyte”, doping strategies that provides a surface protective layer or generates cathode surface reconstruction were employed [76-78].

Dopants such as Mo and Zr were reported to form a layer on the surface of the NCM cathode particle which can protect the active material from the electrolyte [76, 77]. Breuer et al. studied the effects of Mo substitution on NCM 523 [76]. Theoretically, each Mo should have six ligating oxygen atoms when substituting the Ni atoms. However, the hard X-ray extended absorption fined structure (EXAFS) fitting results revealed that the coordination number of Mo-O was 1.3 ± 0.5, which indicates that only a fraction of Mo is placed at the Ni sites while the rest is at the surface. This Mo segregation at the surface was further confirmed by energy dispersive X-ray spectroscopy (EDS) spectra acquired by the scanning transmission electron microscopy (STEM) (Figure 1.4.1c, d). The reduced electrode/electrolyte side reaction by the surface segregated Mo layer lead to a higher capacity retention of ~89% after 60 cycles at a C/3 rate, while the undoped NCM 523 exhibited a capacity retention of only ~76%.

As for Zr doping on LNO, Li_2ZrO_3 layer formation on the particle surface was reported. Yoon et al. doped LNO with Zr^{4+} ions by adding the Zr during the synthesis of the $Ni(OH)_2$ precursor prior to lithiation [77]. During lithiation, part of the Zr ions reacted with the residual LiOH at the surface forming a self-passivating Li_2ZrO_3 surface layer with a thickness of 5-10 nm while the rest of the Zr ions were intercalated into the crystal lattice. The Li_2ZrO_3 layer reduced the

electrode/electrolyte side reactions while the intercalated Zr increased the structural stability of LNO. The differential capacity curve profiles showed the lower intensity of the peak corresponding to the H2→H3 transition, indicating the reduced structural degradation. The Nyquist plots of the electrochemical impedance revealed that the charge transfer resistance (R_{ct}) for Zr-doped LNO was remained below 10 Ω up to 100 cycles, whereas the R_{ct} value of the undoped LNO reached 85 Ω after 100 cycles. The constant low R_{ct} value of the Zr-doped LNO suggests a stable SEI formation on the surface attributed by the Li_2ZrO_3 layer.

As explained in the previous sections, the surface reconstruction which occurs during the cycling of NCM accompanies structural collapse and oxygen evolution [44]. Therefore, the formation of the rock-salt phase by the surface reconstruction was commonly reported as a deterioration factor for NCM. However, the recent studies revealed that the rock-salt phase formed prior to cycling can rather increase the cycle life of Ni-rich NCM cathodes [78]. The rock-salt phase can act as a coating layer to prevent the electrode/electrolyte side reactions and suppress the additional phase transition during cycling. The surface reconstruction of the pristine state LNO by W doping was reported to be effective in enhancing the electrochemical properties [78]. Automatic TEM phase-identification/orientation mapping technique (ASTAR) revealed the rock-salt phase (Fm3-m) segregation at the surface of LNO after W-doping (Figure 1.4.1e, f). Through DFT calculations, it was shown that W-doping increases the surface energy of the layered LNO(10-14) plane and lowers the surface energy of the rock salt LNO(001) plane, as a result, W-doping leads to the surface phase transition from the layered structure to the rock salt phase. Although W-doped LNO exhibited a slight decrease of discharge capacity than the undoped counterpart (LNO= 255 mAh g^{-1}, W-doped LNO=245 mAh g^{-1} at a 0.1 C rate, between a voltage range of 2.7-4.3 V) due to the inactive rock-salt phase, it exhibited a higher capacity retention of 90% after 100 cycles compared to the 74% of pristine LNO.

As delithiated NCM cathodes are highly unstable, cycling the cathodes under high temperature conditioning could provoke the phase transitions that are accompanied with oxygen evolution, thus leading to thermal runaway. As the high thermal stability of NCM is essential for the battery industry, dopants which have a strong bonding energy with oxygen, such as Sn, Al, and Ti, were investigated in order to "suppress the oxygen evolution".

To unveil the effect of Sn doping on the oxygen evolution, Eilers-Rethwisch et al. investigated Sn-doped NCM 622 cathode using thermogravimetric analysis (TGA), which provided the information of the decomposition temperature and the release of gas in terms of mass loss (Figure 1.4.1.1a) [79]. For the analysis, the pristine and Sn-doped NCM 622 were first charged to 4.3 V and then heated up to 650 ℃. During the heating procedure, the TGA results showed that the average mass loss was 10.8 wt% and 9.0 wt% for undoped and Sn-doped NCM respectively, which indicates the lower oxygen release for Sn-doped NCM 622. Furthermore, the major mass loss corresponding to the phase transition from the layered structure to the spinel phase occurred at ~345 ℃ for undoped NCM 622, while the Sn-doped NCM 622 took place in the divided steps at ~288℃ and ~368℃. The step was not divided for undoped NCM 622 due to faster decomposition and higher mass loss. The reason for the thermal stability improvement by Sn doping was attributed to the strong Sn bond dissociation energy of Sn-O (548kJ mol^{-1}) that shortens the Sn-O bond length that aids in suppressing the oxygen release.

To systematically investigate the effect of doping on stabilizing the lattice oxygen, Dixit et al. performed the DFT calculations to seek the effect of Al incorporation on NCM's thermal stability [80]. The results proposed that Al transfers its electrons to oxygen, therefore, increasing the oxygen charge state. As a higher oxygen charge state leads to the increase of oxygen binding energy, the Al-doped NCM showed a 33% higher oxygen binding energy than the undoped counterpart [81]. Furthermore, the strong Al(s)-O(p) overlap, which was not found

for other metal dopants, suggested more ionic bonding characteristic of the Al-O bond. The structure and thermal stabilization of NCM with Al doping was further verified by experiments conducted by Do and co-workers [82]. Differential scanning calorimeter (DSC), which shows the exothermic peaks related to the thermal stability of the material, was utilized to calculate the activation energy of the undoped and Al-doped NCM 811 in the temperature range of 25-400 ℃. The major exothermic peak was observed at 321.5 ℃ for undoped NCM 811, while the peak shifted toward higher temperature of 324 ℃ after Al doping, which was accompanied with the reduced exothermic peak intensity. The results indicate that Al doing successfully improved the thermal stability of NCM.

As mentioned earlier, Ti^{4+}, which has delocalized d orbitals, increases the TM-O bonding strength when doped to the layered cathode, therefore, enhancing the structural stability. To investigate the effect of Ti doping on oxygen stability, Qiu et al. investigated the oxygen K-edge by soft XAS for undoped and Ti-doped NCA at various charge states up to 4.7 V (Figure 1.4.1.1b) [72]. As for undoped NCA 811, the intensity of the peak at 528.2 eV, which corresponds to the unoccupied density of states in the Ni 3d-O 2p bands, increased when the charge voltage increased from 4.5 to 4.7 V. This increase of the peak intensity indicates the formation of O 2p holes. The same peak intensity showed almost no change for Ti-doped NCA at the same voltage range, which means the less oxygen electronic structure transformation during the charge process, thus, stabilizing the lattice oxygen during delithiation.

"Intergranular crack", which is caused by the lattice collapse along the crystallographic c-axis direction upon H2→H3 phase transition, leads to the hindrance of charge percolation, unwanted parasitic surface reaction, and phase transformation due to the direct contact between freshly exposed surfaces with electrolyte [42]. Thus, to mitigate the problematic issue, dopants which effectively reduce the mechanical stress caused by the anisotropic lattice contraction,

such as B and W, were studied in order to suppress the crack formation and improve the cycle life of NCM cathodes [83-85].

In case of B-doping, element incorporation into Ni-rich NCM modified the primary particle morphology, which alleviated the stress caused by the H2→H3 phase transition during cycling. Park et al. have shown that the incorporation of boron into Ni-rich NCM produced highly crystallographic textured morphology, in which the primary particles were tend to elongate in the radial direction (Figure 1.4.1.1c) [83]. According to DFT calculations, the B dopant lowered the energy of the (003) surface which lead to the radial shape of the primary particle. Attributed by its morphology, the mechanical stress caused during cycling was spread uniformly which alleviated the local stress concentration. The improved stress reduction was confirmed by differential capacity curve profiles, in which the H2→H3 peak intensity was effectively maintained after 100 cycles for B-doped NCM 90. Due to the stress concentration during cycling, the cross-sectional SEM images of the undoped NCM 90 charged to 4.3 V showed numerous cracks across the secondary particle. On the contrary, the B-doped NCM 90 at the same condition showed no particular cracks. Thus, after 100 cycles at rate of 0.5 C, 91% of the discharge capacity was retained for B-doped NCM 90 while only 83% was retained for the undoped counterpart.

In-situ XRD was conducted by Ryu et al. to investigate the structural stabilization effect of W doping on LNO [84]. Above the charge voltage of 4.1 V, the abrupt shift of the (003) peak due to H2→H3 phase transition was clearly observed for undoped LNO, which indicates the severe lattice collapse. On the other hand, the (003) peak of the W-doped LNO showed a smooth continuous shift towards the H3 phase. A similar effect by W doping was observed for NCM 90 [85]. According to the differential capacity curve profiles, the W-doped NCM 90 showed more reversible H2→H3 phase transition during cycling compared to the undoped NCM 90,

which indicates the less irreversible structural damages caused by anisotropic lattice contraction. Consequently, the cross-sectional scanning electron microscope (SEM) images revealed the less crack formation for the W-doped NCM 90 than the undoped NCM 90 when both materials were charged to a high voltage of 4.5 V (Figure 1.4.1.1d). As a result, W-doped NCM 90 exhibited the same initial capacity of 235mAh g^{-1} at 0.1 C but a higher capacity retention (94.5% vs. 81.0%) after 100 cycles at 0.5 C with a cutoff voltage of 4.4 V.

Overall, elemental doping seems to be a reasonable way to resolve the various deterioration factors of NCM cathodes. Titanium significantly reduced cation mixing and increased the thermal stability of NCA cathodes [72]. Tungsten doping enhanced the cycle life of NCM by suppressing the crack formation while also reducing the electrode/electrolyte side reactions [78,84,85]. Although various dopant elements were reported to be effective in enhancing the NCM cathodes, the deep researches in the dopant optimization, such as control of doping concentration or doping methods, have not been thoroughly conducted. As the dopant optimization may be a critical factor in improving the NCM cathodes, further experiments and researches are required.

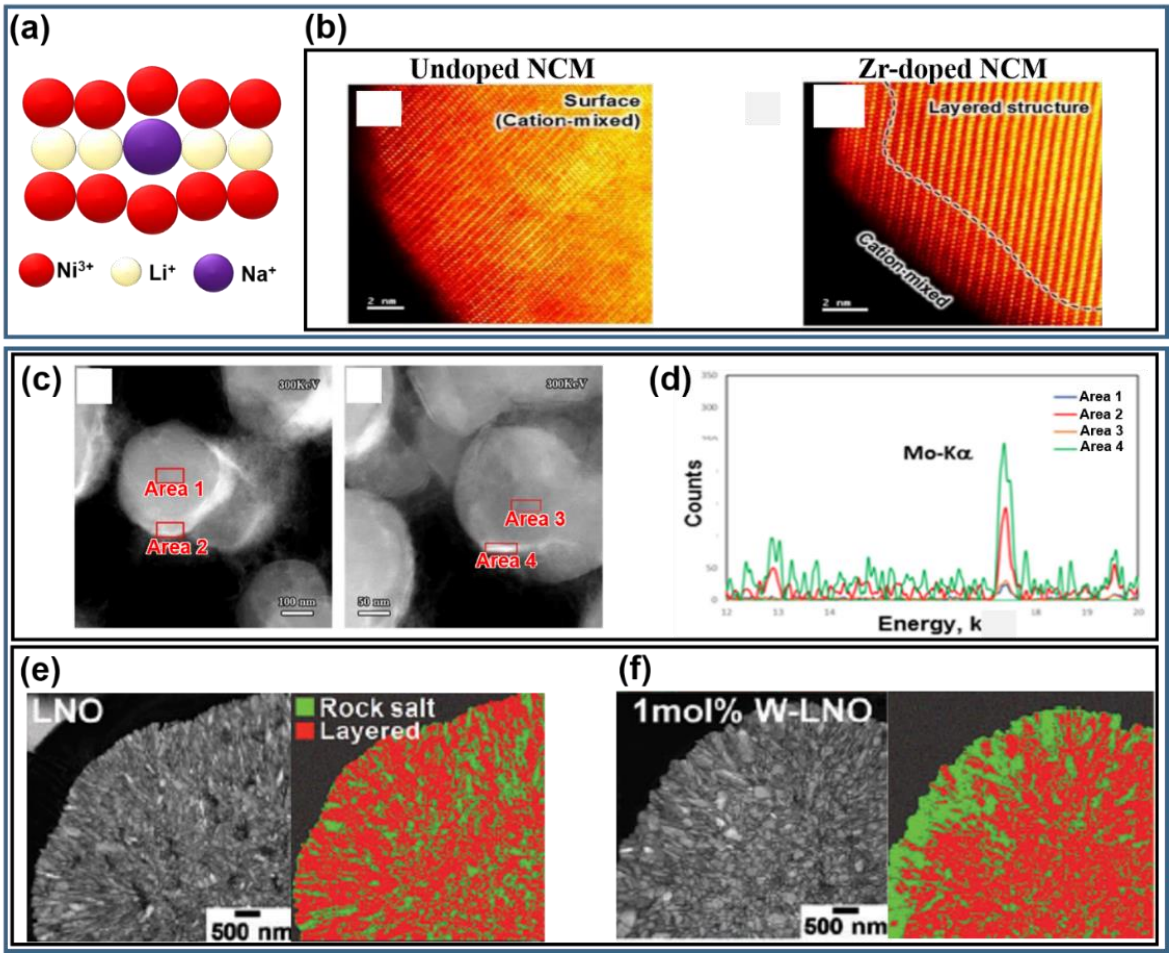

Figure 1.4.1. (a) Schematic illustration of the Na doping effect in NCA 811, (b) HAADF images of undoped and Zr-doped NCM after cycling. Reproduced with permission [73]. Copyright 2019, Wiley, (c) HAADF images of the Mo-doped NCM 523. Different locations in the bulk and at the surface are indicated as areas 1, 3 and 2, 4, respectively, (d) EDS spectra acquired from areas 1-4. (c, d) Reproduced with permission [76]. Copyright 2018, American Chemical Society, and (e, f) bright field images and corresponding ASTAR TEM phase mapping for (e) undoped LNO and (f) W-doped LNO. (e, f) Reproduced with permission [78]. Copyright 2018, Royal Society of Chemistry.

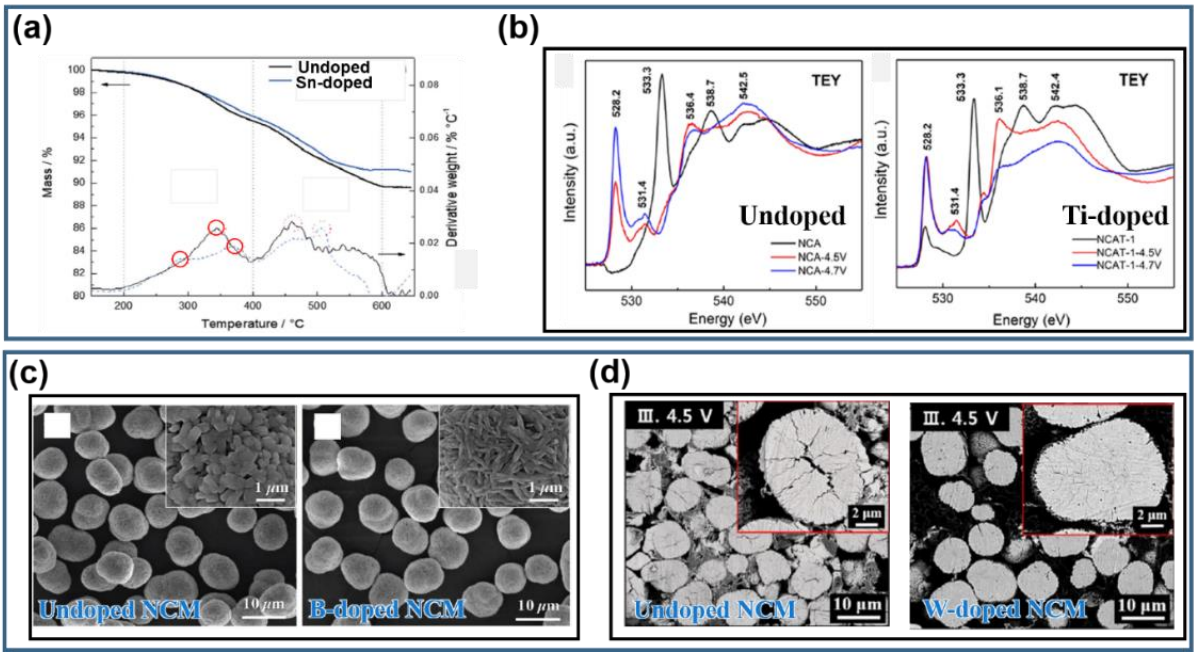

Figure 1.4.1.1 (a) TGA measurement of mass loss (thick line) and derivative of weight (thin line) of charged undoped and Sn-doped NCM 622. Reproduced with permission [79]. Copyright 2018, Elsevier, (b) soft XAS spectra of O K-edge for undoped and Ti-doped NCA 811. Reproduced with permission [72]. Copyright 2019, American Chemical Society, (c) SEM images of undoped and B-doped NCM 90. Reproduced with permission [83]. Copyright 2018, Wiley, and (d) cross-sectional SEM images of the 1st charged states at 4.5 V of undoped NCM 90 and W-doped NCM90. (d) Reproduced with permission [85]. Copyright 2019, Elsevier.

1.4.2. Coating methods

The main purpose of the coating strategies for the NCM is to prevent the direct contact of the electrode from the electrolyte in order to reduce the electrolyte/electrode side reactions [86, 87]. Furthermore, the surface stabilization effect by the coating method may also aid in suppressing the oxygen evolution of NCM during multiple cycles [86]. The coating materials include metal oxides, phosphates, and lithium salts [86-90]. In this review, we divided the coating materials into two groups, lithium-uncontained metal oxides and lithium-contained

compounds, according to the “elimination of residual lithium on NCM particle”, in which lithium-contained compounds successfully reduced the NCM residual lithium impurities that was not able for lithium-uncontained metal oxides.

Lithium-uncontained metal oxides such as Al_2O_3 and TiO_2 have been reported as an efficient protective layer material for NCM [86,87]. Shi et al. improved the electrochemical stability of NCM 523 by coating the surface with an ultrathin Al_2O_3 layer by ALD (Figure 1.4.2a) [86]. In order to effectively compare the cycling stability of bare and Al_2O_3-coated NCM 523, both materials were charged to a high voltage of 4.8 V. This is because the side reactions become much more severe at a high charge voltage due to the increased portion of highly reactive Ni^{4+} content of NCM. As a result, the Al_2O_3-coated NCM 523 demonstrated a higher capacity retention of 76.8% after 30 cycles at 1 C compared to the 58.4% capacity retention of bare NCM 523 due to the reduced electrode/electrolyte side reactions. Interestingly, Al_2O_3 coating also enhanced the thermal stability of NCM 523. The DSC measurements were conducted to investigate the oxygen released by the electrode/electrolyte reactions (Figure 1.4.2b) [86]. When charged to 4.8 V after 20 cycles, the bare NCM 523 exhibited an exothermic peak at 355 ℃ with a heat generation of 3600 J g^{-1}. Although the heat generation was the same, the thermal peak was delayed to 367 ℃ for Al_2O_3-coated NCM 523, indicating the improved thermal stability.

TiO_2 coating is other method to enhance the cycle life of NCM. Kim et al. researched the TiO_2-coated NCM 622 and proved the enhanced electrochemical performance after coating [87]. The TiO_2-coating suppressed the growth of the cathode-electrolyte interface (CEI) layer, which improved the cyclability of NMC 622. As a result, TiO_2-coated NCM 622 demonstrated a higher capacity retention of 65.52% (116.7 mAh g^{-1}) compared to the 39.63% (66.9 mAh g^{-1}) of the undoped NCM 622 after 200 cycles at 1 C rate with a high cutoff voltage of 4.5 V.

Even though the coating lithium-uncontained metal oxides on the NCM is an effective way to shield the active material from the electrolyte, they possess electrochemically and electrically inactive characteristics which might impede the lithium ion transfer on the particle surface [88]. As an alternative coating material, lithium-containing or lithium-reactive compounds were proposed [88-90]. This layer not only protects the cathode material from the electrolyte but also act as a lithium ion conductor, which can facilitate the lithium ion diffusion. Furthermore, these compounds react with the residual lithium on the surface of NCM, thus reducing the hazardous effects caused by the impurities.

For the comparison between lithium-uncontained metal oxide and lithium-contained metal oxide as a coating material, Liu et al. prepared both Al_2O_3-coated NCM 622 (Al-O-2) and $LiAlO_2$-coated NCM 622 (Li-Al-O-2) via a sol-gel method [88]. When a cycling test with a cutoff voltage of 4.5 V was conducted, $LiAlO_2$-coated NCM 622 displayed the highest initial discharge capacity (bare NCM 622: 187.2 mAh g^{-1}, Al-O-2: 196.9 mAh g^{-1}, Li-Al-O-2: 206.8 mAh g^{-1}) (Figure 1.4.2c). Furthermore, $LiAlO_2$-coated NCM 622 exhibited the best capacity retention after 100 cycles at 0.2 C (bare NCM 622: 79.7%, Al-O-2: 84.5%, Li-Al-O-2: 87%) and superior rate capability compared to the bare NCM and Al-O-2 (Figure 1.4.2c ,d). Although Al_2O_3 coating did improve the electrochemical property of bare NCM 622, $LiAlO_2$ coating showed a more remarkable enhancement due to the lithium ion conducting properties.

The residual lithium on the surface of NCM 811 was successfully reduced by Li_3PO_4 coating. Zhu et al. synthesized Li_3PO_4-coated NCM 811 by adding the precursor $Ni_{0.8}Co_{0.1}Mn0.1(OH)_2$ into $(NH_4)_2HPO_4$ aqueous solution [89]. After lithiation by heating the precursor with $LiOH{\cdot}H_2O$, the PO_4^- polyanions reacted with the residual Li_2O/LiOH on the NCM surface, thus forming a Li_3PO_4 layer. The neutralization titiration results revealed that the 6237 ppm of residual lithium species (LiOH and Li_2CO_3) in the bare NCM 811 was reduced to 3935 ppm

after Li_3PO_4 coating. Furthermore, the Li_3PO_4 coating layer was also proved by Lee et al. to be effective to enhance the thermal stability of NCM by suppressing the phase transition during temperature increase [90]. Both bare NCM 622 and Li_3PO_4-coated NCM 622 (LP-NCM) were charged to 4.3 V and then examined by *in situ* time-resolved XRD while heating the samples from room temperature to 500 ℃ (Figure 1.4.2e, f). At the temperature range of 276-384 ℃, the bare material showed the phase transition from layered structure to disordered $LiMn_2O_4$-type spinel structure. The phase transition was completed at 324 ℃ for the bare NCM 622, while the phase transition temperature was delayed to 360 ℃ after Li_3PO_4 coating. Furthermore, the bare NCM 622 underwent the phase transition from the spinel structure to the rock salt phase at the temperature range of 394-500 ℃, while no rock salt phase peaks were detected for LP-NCM. The results above proved that Li_3PO_4 coating is an effective method to enhance the thermal stability of NCM due to the reduction of residual lithium impurities and suppressed the phase transition at high temperature.

As the primary particle within the secondary particle undergoes microcracks for Ni-rich NCM during cycling, the surface coating on secondary particle cannot prevent the electrolyte penetration along the cracks, which results in the unwanted parasitic reactions between in-grain primary particle and electrolyte [42]. Recently, a new coating strategy was proposed, rather than just covering the secondary particle surface. The coating layer was infused through the gaps between the grain boundaries of the cathode, thus coating the material from outside to inside [91-93]. This methodology of coating acts as a glue-like filler which stabilizes the overall surface and bulk structure of the cathode.

This glue-like filler coating concept was first proposed by Kim et al. [91]. NCA 811 was added into an ethanol solution including dissolved lithium and cobalt acetate (Figure 1.4.2g). Therefore, ionized coating sources infiltrated into the gaps between particles of NCA 811 and

formed a spinel-like Li_xCoO_2 (LCO) structure between the grains. As the LCO filled the void gap between the NCA primary particles facets, the strong bond strength of the NCA/LCO interface increased the overall mechanical strength of the NCA material. The cross sectional STEM images revealed the shattered grains of the pristine material after 300 cycles while the LCO-infiltrated sample showed the rather intact secondary particles (Figure 1.4.2h). The LCO-infiltrated NCA 811 demonstrated the same initial discharge capacity of 200 mAh g^{-1} as the bare counterpart and showed a high capacity retention of 87% after 300 cycles at 60 ℃ (charge rate: 0.5 C, discharge rate: 1 C).

A solid electrolyte Li_3PO_4 (LPO) was infused through the grain boundaries of NCM 811 by Yan et al. in order to suppress the crack formation and increase the surface kinetics [92]. The LPO on the surface of the secondary particle and between the grains blocked the electrolyte from penetrating the grain boundaries, thus mitigating the thick SEI layer formation on the surface and along the grain boundaries. Additionally, the infused LPO enabled the fast lithium-ion transport throughout the cathode, therefore enhancing the rate capability.

The enhanced structural integrity of NCM 333 with the surface coating on primary particle level was reported by Xu and co-workers [93]. An electronically conductive ion-permeable poly(3,4-ethyl-enedioxythiophene) (PEDOT) layer was coated on both the secondary and primary particles of NCM 333. During high voltage cycling, the PEDOT method proved to be effective to suppress the phase transition of perfect layered structure (R-3m) to spinel structure (Fd-3m) which is usually accompanied by the oxygen loss. The suppression of oxygen evolution and phase transition by PEDOT reduced the micro strain caused by the crystal structure mismatch between layered and spinel structure. The severe intergranular cracks that were found for uncoated NCM 333 after 200 cycles were not observed in the case of PEDOT coated NCM 333. Furthermore, PEDOT improved the thermal stability, in which the

exothermal peak of DSC of the delithiated bare NCM 333 was shifted to a 42 °C higher temperature after PEDOT coating.

To sum up, surface coating strategies seem to be a promising approach to improve the surface stability of NCM by reducing the reaction between electrode and electrolyte [86,87,91]. Especially for the coating strategy on primary particle level, the bulk stabilization effect could also be achieved, which successfully suppresses the crack formation during cycling. As coating on primary particle level resolves most of the deterioration factors of NCM, the strategy may seem like a promising solution for the improvement of NCM. However, the industrial electrode fabrication condition should not be overlooked as the coating on primary particle level requires an additional fabrication procedure after the coating process. The weighing between cost and effectiveness of the strategy should be considered for the commercialization of the method.

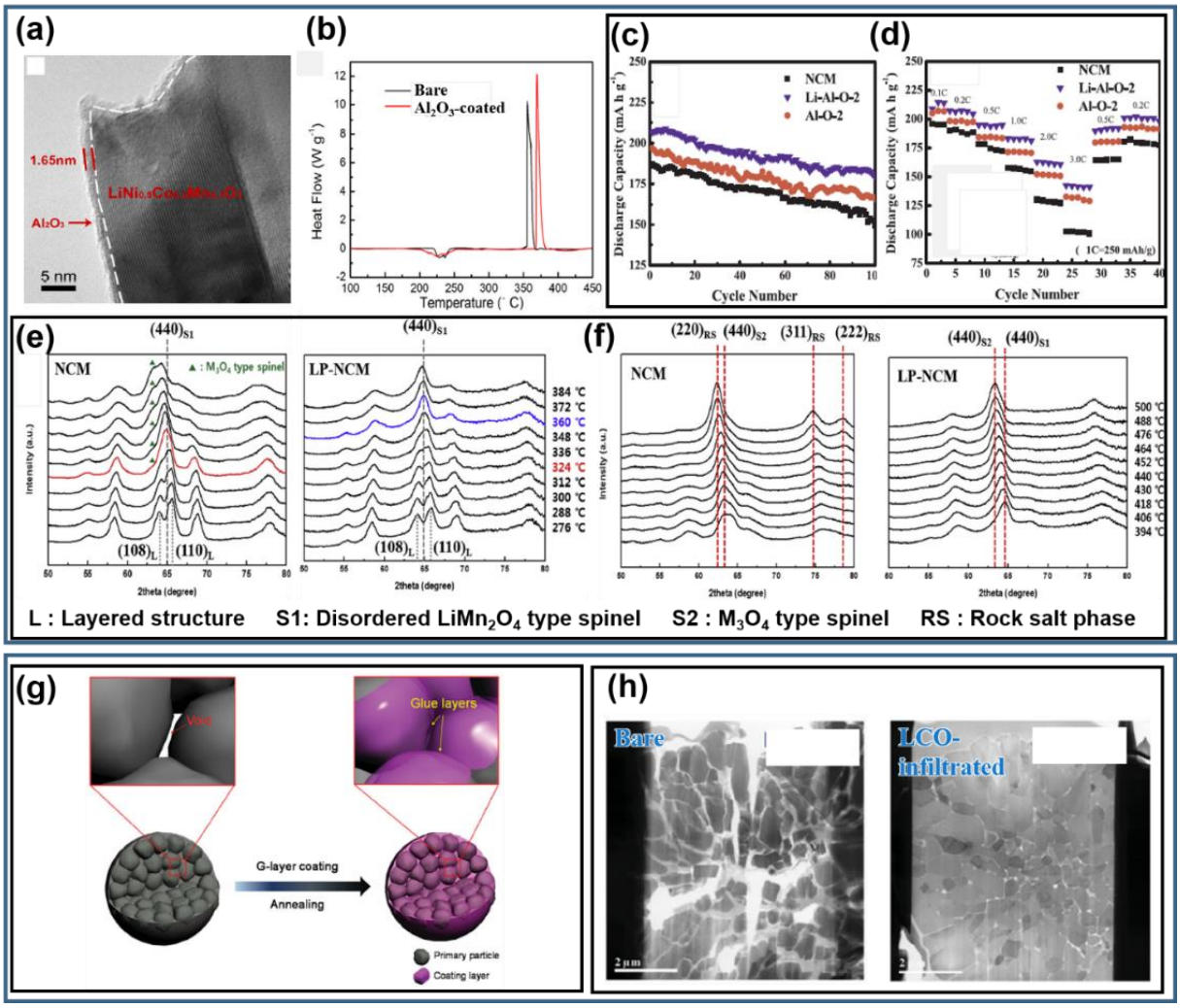

Figure 1.4.2. (a) HRTEM image of Al_2O_3-coated NCM 622. (b) DSC curves of bare and Al_2O_3-coated NCM 523. (a, b) Reproduced with permission [86]. Copyright 2016, Elsevier, (c) cycle performance and (d) rate capability of bare NCM 622, Li-Al-O-2, and Al-O-2. (c, d) Reproduced with permission [88]. Copyright 2018, Elsevier, (e, f) *in situ* XRD patterns for charged bare NCM and LP-NCM in the temperature range of (e) 276-384 ℃ and (f) 394-500 ℃. (e, f) Reproduced with permission [90]. Copyright 2017, Elsevier, (g) scheme of the formation of glue layer on NCA, and (h) STEM images of bare and LCO-infiltrated NCA after 300 cycles. (g, h) Reproduced with permission [91]. Copyright 2016, Wiley.

1.4.3. Other methods

Until recently, bulk doping and surface coating have been the two main strategies to enhance the NCM's electrochemical performance [70-73,86-88]. To successfully utilize Ni-rich cathode materials for practical devices, other measures were developed to solve the instability issues and increase the battery lifespan such as "core-shell structure", "single crystal", "gradient doping", and "epitaxial layered nanostructure coating" [94-101]. These strategies enhanced the NCM cycle life with different mechanisms, which will be discussed below.

The "core-shell" design indicates the Ni-rich NCM core encapsulated with the Ni-low NCM shell (Figure 1.4.3a). Therefore, this design takes advantage of the high capacity of the Ni-rich core and high thermal and mechanical stability of the Ni-low surface layer [94]. In order to design the core-shell structure, precise control of co-precipitation parameters and/or delivery of the precursor solution to the reactor are required [95]. The core-shell design with a composition of $LiNi_{0.85}Co_{0.1}Mn_{0.05}O_2$ was prepared by Lee et al. [94]. As for the specifics of the design, the thickness of the Ni-low surface layer was approximately 200 nm while the Ni concentration of the core and shell was 81 and 63%, respectively. Attributed by its structure, the core-shell NCM demonstrated the higher capacity retention of 82.3% after 150 cycles under an elevated temperature of 60 ℃ compared to that of the bare Ni-rich cathode (65.4%).

The core-shell design also proved to be effective in reducing the particle crack formation. Kim et al. prepared a core-shell NCM with a Ni-rich core with a composition of $Li[Ni_{0.94}Co_{0.038}Mn_{0.022}]O_2$ and a 1.5 μm thick Ni-deficient shell with the outermost surface composition of $Li[Ni_{0.841}Co_{0.077}Mn_{0.082}]O_2$ [95]. The Ni deficient outer shell restrained the irreversible H2→H3 phase transition, thus reducing the internal strain generated upon cycling

to 4.3 V. Therefore, the cross-sectional SEM images showed the less intergranular cracks for the core-shell NCM compared to the bare NCM after cycling for 1000 cycles at 1 C (Figure 1.4.3b). As a result, the core-shell NCM delivered a high initial discharge capacity of 229 mAh g^{-1} and exhibited a capacity retention of 88% even after 1000 cycles at 1 C. Consequently, the core-shell structure was proved be effective in enhancing the cycle life and structure stability of the NCM cathodes.

The main advantage of micron-sized "single-crystal" primary particles is the shortened lithium diffusion length and quick lithium transportation channel which lead to a rapid lithiation and delithiation rate [96]. Another advantage of the single-crystal structure NCM is the absence of grain boundary which acts as a nucleation site for microcracks during cycling [97]. In order to enhance the unsatisfactory rate performance of the poly-crystal NCM 622, Wang et al. prepared the sub-micron-sized single-crystal NCM 622 using a hydrothermal method followed by a calcination process (Figure 1.4.3c) [96]. The shortened lithium diffusion lengths lead to a high capacity retention of 89.93% after 100 cycles at 0.2 C rate along with an excellent rate capability.

The enhanced structure stability of the single-crystal NCM 811 (SC-NCM) compared with the poly-crystal NCM 811 was demonstrated by Fan et al. [97]. After 600 cycles at 1 C, the numerous intergranular cracks were observed in the poly-crystal NCM 811 while the SC-NCM remained rather intact without visible cracks (Figure 1.4.3d). Additionally, high-resolution TEM images revealed that the electrolyte infiltration through the intergranular cracks lead to the disordered rock-salt phase on the crack surface in the poly-crystal NCM 811 whereas the SC-NCM showed the less phase transition due to the absence of cracks. As a result, the reduced formation of cracks in the SC-NCM resulted in a higher capacity retention of 84.8% at 45 °C after 600 cycles at 1 C compared to the 58.7% capacity retention of poly-crystal NCM.

Surface modification is an effective way to prevent the direct contact between electrode and electrolyte. However, coating strategies cannot stabilize the internal structure of NCM as doping strategy does. As a result, NCM with a "concentration gradient doping" from the surface to the core was designed to simultaneously achieve the protection of the cathode by the high dopant concentration at the surface and the stabilization of the core by the infusion of the dopant into the structure (Figure 1.4.3e) [98-100].

Various deterioration factors were resolved with Cd gradient doping in NCA 811 by Li et al. [98]. Consequently, a CdO layer was formed on the surface while Cd^{2+} was doped into the material as a gradient form (Figure 1.4.3f, g). The CdO layer reduced the electrode/electrolyte side reactions while the Cd^{2+} inside the crystal lattice reduced the cation mixing and enlarged the crystal layer spacing. As a result, the Cd gradient doping improved the cycle stability and the rate performance of NCA 811.

In case of B gradient doping, oxide coating layer was formed on the outermost particle surface while inner surface of NCM was transformed into rock-salt phase [99]. Furthermore, boron was incorporated into tetrahedral site of layered cathode in gradient form, which stabilized the structure. As a result, the modified NCA 90 was consisted of $LiBO_2$, rock-salt phase (Fm-3m), and layered structure phase (R-3m) from the surface to the core. The concentration gradient B-doped NCM showed a higher reversibility of the H2→H3 phase transition compared to undoped NCM. As a result, the B-modified NCM showed higher initial discharge capacity (189.77 mAh g^{-1} vs. 188.93 mAh g^{-1}) and higher capacity retention (89.43% vs. 44.90%) than the undoped NCM after 200 cycles at 1 C.

Mn gradient doping was reported by Xu et al. to form a protective layer while stabilizing the structure of NCA 811 [100]. After gradient doping, the abundant Mn^{4+} at the outer surface of NCA 811 increased the Ni^{2+}/Ni^{3+} ratio by charge balance and formed a rock-salt phase which

was mostly segregated at the surface region. Consequently, the rock-salt phase shielded the electrode from the electrolyte. Furthermore, the Ni^{2+} occupying the Li slabs acted as a pillar to stabilize the structure, thus improving the capacity retention significantly. As a result, the Mn^{4+} gradient doped NCA 811 exhibited higher capacity retention of 80.0% at 5 C after 500 cycles compared to the 40.1% of undoped NCA 811.

The dissolution of TM from the NCM cathode material and migration toward anode side negatively affect the cycle performance of full-cell by creating a non-uniform and unstable SEI layer on the anode material. To suppress the dissolution of TM, Cho et al. took a full advantage of a nanosized cobalt hydroxide to prepare a "nanostructured stabilizer with an epitaxial structure" on the surface of NCM 811 (Figure 1.4.3h) [101]. The stabilizer was composed of spinel Co_3O_4, spinel Li_xCoO_2, and layered $LiCoO_2$ from the surface to the core (Figure 1.4.3h, i). The inactive spinel Co_3O_4 stabilized the NCM 811 surface while the spinel Li_xCoO_2 increased electronic conductivity due to its low band gap. The stabilized surface alleviated the nickel ion crossover from the cathode to the anode, creating a uniform and dense SEI layer on the graphite anode after 500 cycles (Figure 1.4.3j). As a result, the full-cell with the surface-modified NCM as a cathode and graphite as an anode exhibited a discharge capacity retention of ~51% after 500 cycles at 45 ℃ within a voltage range of 2.8-4.2 V (charge rate: 0.5 C, discharge rate: 1 C) while the bare-NCM/graphite full-cell exhibited a poor capacity retention of ~20%.

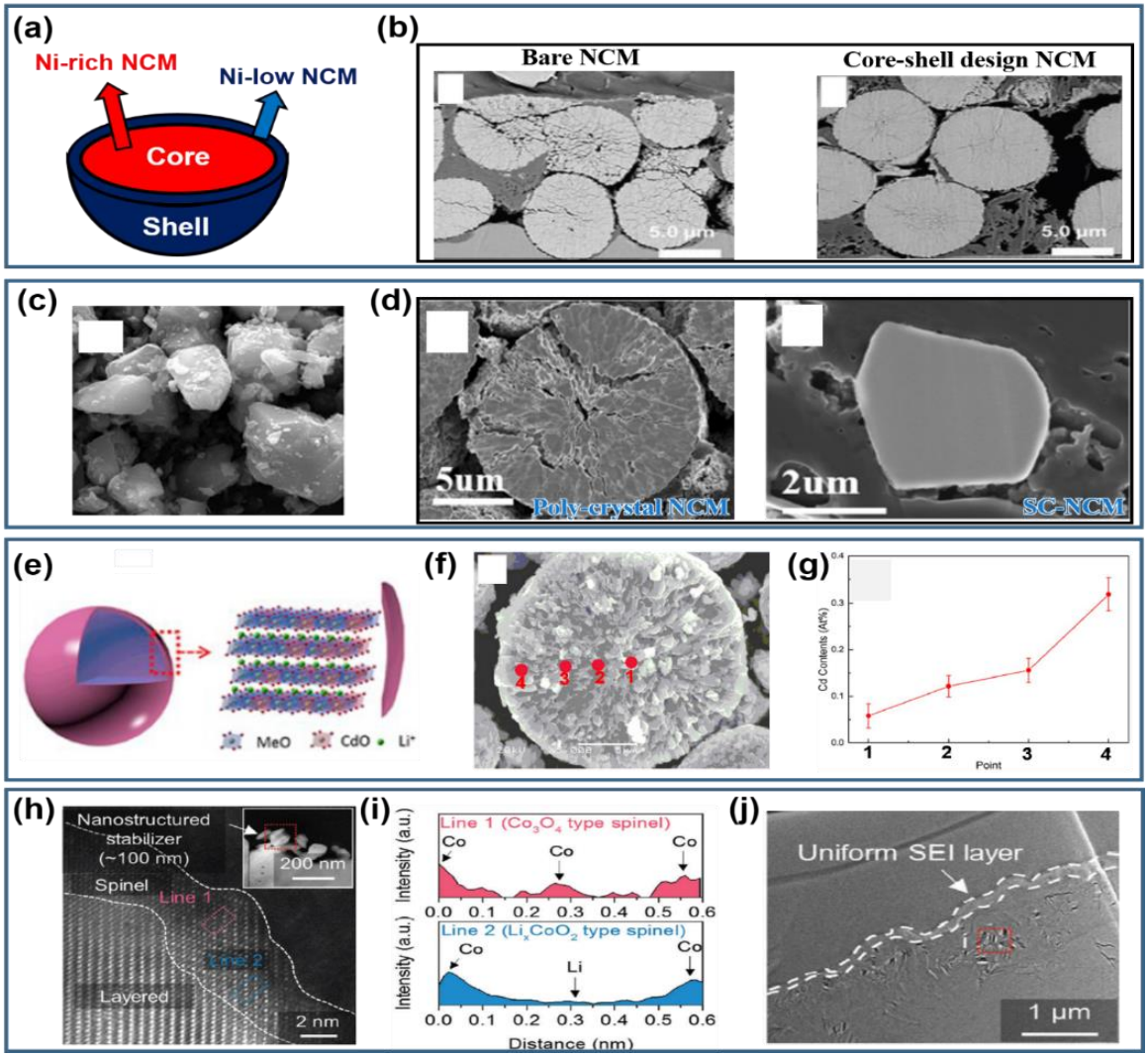

Figure 1.4.3. (a) Scheme of core-shell, (b) CP-SEM images of bare NCM and core-shell design NCM after cycles. (b) Reproduced with permission [95]. Copyright 2019, Wiley, (c) SEM image of single-crystal NCM 622. Reproduced with permission [96]. Copyright 2016, Elsevier, (d) CP-SEM images of poly-crystal NCM 811 and SC-NCM after cycles. (d) Reproduced with permission [97]. Copyright 2020, Elsevier, (e) scheme of Cd gradient doping, (f) CP-SEM images of Cd gradient doped-NCA 811, (g) EDS mapping analysis of Cd content from the region marked with red dots in (f). (e, f, g) Reproduced with permission [98]. Copyright 2020, Elsevier, (h) HAADF-STEM images of the stabilizer on the NCM surface, (i) corresponding HAADF signal profiles of the pink and blue boxes in (h), and (j) TEM image of the graphite anode after cycling test. (h, i, j) Reproduced with permission [101]. Copyright 2018, Royal Society of Chemistry.

1.5. Conclusion and future perspectives

In this review, we firstly introduced the various deterioration mechanisms and challenges of NCM cathodes that have to be faced for the successful applications. Although each degradation factor may seem separate, they are highly co-linked to each other. The surface phase transformation from layered structure to rock-salt phase, which arise from the Li-Ni exchange, accompanies oxygen evolution and electrolyte decomposition. The oxygen evolution at high voltages (or high SOC) induces the compressive stress that could lead to nano/micro particle cracks. Furthermore, the above mechanisms become much intense at high operational temperature due to thermally vulnerable characteristic of delithiated NCM. The notable deterioration factor that is receiving attention nowadays is the state-of-charge (SOC) heterogeneity within the particle, which is caused by the micrometer sized secondary particle of NCM that delays the lithium/charge transport. As far as we know, the profound understanding and strategies to resolve the SOC heterogeneity has yet not been clearly suggested.

In order to mitigate the deterioration factors, various NCM modifications were proposed. Modifications such as bulk doping to suppress the cation mixing degree or coating to protect the highly reactive Ni^{4+} from the electrolyte were extensively researched. The improved thermal stability could be achieved by doping metals that have a strong bonding strength with oxygen or by stabilizing the surface with coating. Apart from conventional doping and coating methods, other strategies such as core-shell structure, single-crystal structure, surface coating on primary particle level, gradient doping, and epitaxial layered nanostructure coating strategies were proposed.

Even though each of the proposed methodology resolves one or more deterioration factors

of NCM with different mechanisms, there still remain several considerations for the future development of Ni-rich NCM cathode materials. (1) Strategies to resolve the SOC heterogeneity are required as its phenomena accelerates the oxygen release and crack formation during NCM cycling. The primary particle modification might be the key for the resolution as the crystallographic orientation of primary particle could influence the SOC heterogeneity [54, 102]. (2) Further researches on multiple-element doping should be conducted as it is a promising way to improve the cycle performance of NCM. For instance, K and Cl dual doping proved to enhance the cycle life of NCM as the K reduced cation mixing and Cl increased the structure stability [71]. Additional researches on these kind of synergetic effects could reveal the new mechanism to resolve the deterioration factors. (3) Electrolyte modification should also be considered as the electrolyte decomposition during NCM charge process creates a CEI layer on the particle surface that could seriously impact the cathode electrochemical performance [103]. The research on the electrolyte chemical formula or modification of the electrolyte additive is required to form a uniform CEI layer with high ionic conductivity and stability [104]. (4) The industrial fabrication condition of the proposed strategies should not be overlooked. As each of the proposed strategy requires an extra fabrication process, the effect of the strategy compared to the cost increase should be considered for the industrial application.

Various variables have to be considered to develop the NCM cathode with high energy density and thermal stability, thus making it a difficult task. However, stabilization of NCM cathode is highly requisite to meet the increasing demand of energy storage devices and EVs every year. Therefore, to further enhance the electrochemical and thermal properties of NCM for its successful application, the degradation mechanisms as well as working mechanism of the proposed strategies should be thoroughly understood.

1.5. Reference

[1] G. E. Blomgren, J. Electrochem. Soc. 2017, 164, A5019-5025

[2] Y. Wang, B. Liu, Q. Li, S. Cartmell, S. Ferrara, Z. D. Deng, J. Xiao, J. Power Sources. 2015, 286, 330-345

[3] C.-H. Jung, J. Choi, W.-S. Kim, S.-H. Hong, J. Mater. Chem. A. 2018, 6 8013-8020

[4] J. Molenda, Solid State Ionics. 2005, 176, 1687-1694

[5] F.-D. Yu, L.-F. Que, Z.-B. Wang, Y. Zhang, Y. Xue, B.-S. Liu, D.-M. Gu, J. Mater. Chem. A. 2016, 4, 18416-18425

[6] Y. Wang, Q. Zhang, Z. -C. Xue, L. Yang, J. Wang, F. Meng, Q. Li, H. Pan, J.-N. Zhang, Z. Jiang, W. Yang, X. Yu, L. Gu, H. Li, Adv. Energy Mater. 2020, 10, 2001413

[7] Y. Xia, J. Zheng, C. Wang, M. Gu, Nano Energy. 2018, 49, 434–452

[8] R. Zhang, Y. Zheng, Z. Yao, P. Vanaphuti, X. Ma, S. Bong, M. Chen, Y. Liu, F. Cheng, Z. Yang, Y. Wang, ACS Sustainable Chem. Eng. 2020, 8, 9875−9884

[9] M. D. Radin, S. Hy, M. Sina, C. Fang, H. Liu, J. Vinckeviciute, M. Zhang, M. S. Whittingham, Y. S. Meng, A. Van der Ven, Adv. Energy Mater. 2017, 7, 1602888

[10] H. Maleki Kheimeh Sari, X. Li, Adv. Energy Mater. 2019, 9, 1901597

[11] I. Y. Kim, S. Y. Shin, J. H. Ko, K. S. Lee, S. P. Woo, D. K. Kim, and Y. S. Yoon, J. Korean Ceram. Soc. 2017, 54, 9-22

[12] S. Schweidler, L. d. Biasi, P. Hartmann, T. Brezesinski, J. Janek, ACS Appl. Energy Mater. 2020, 3, 2821−2827

[13] U.-H. Kim, L.-Y. Kuo, P. Kaghazchi, C. S. Yoon, Y.-K. Sun, ACS Energy Lett. 2019, 4, 576-582

[14] P. K. Nayak, E. M. Erickson, F. Schipper, T. R. Penki, N. Munichandraiah, P. Adelhelm,

H. Sclar, F. Amalraj, B. Markovsky, D. Aurbac, Adv. Energy Mater. 2018, 8, 1702397

[15] X. Han, L. Lu, Y. Zheng, X. Feng, Z. Li, J. Li, M. Quyang, eTransportation. 2019, 1, 100005

[16] J.-H. Kim, H.-H. Ryu, S. J. Kim, C. S. Yoon, Y.-K. Sun, ACS Appl. Mater. Interfaces. 2019, 11, 30936−30942

[17] W. Liu, P. Oh, X. Liu, M. -J. Lee, W. Cho, S. Chae, Y. Kim, J. Cho, Angew. Chem. Int. Ed. 2015, 54, 4440–4457

[18] G. Shang, Y. Tang, Y. Lai, J. Wu, X. Yang, H. Li, C. Peng, J. Zheng, Z. Zhang, J Power Sources. 2019. 423, 246-254

[19] X. Li, K. J. Zhang, M. S. Wang, Y. Liu, M. Z. Qu, W. Zhao, J. M. Zheng, Sustain. Energ. Fuels. 2018, 2, 413-421

[20] L. Wu, X. Tang, X. Chen, Z. Rong, W. Dang, Y. Wang, X. Li, L. Huang, Y. Zhang, J. Power Sources. 2020, 445, 227337

[21] S.-J. Sim, S.-H. Lee, B.-S. Jin, H.-S. Kim, Sci. Rep. 2019, 9, 8952

[22] K. Meng, Z. Wang, H. Guo, X. Li, D. Wang, Electrochim. Acta. 2016, 211, 822-831

[23] J. Kim, H. Kim, and K. Kang, J. Korean Ceram. Soc. 55, 21-35

[24] J. Ko, S. H. Kang, H. W. Cheong, and Y. S. Yoon, J. Korean Ceram. Soc. 2019, 56, 233-255

[25] X. Xu, H. Huo, J. Jian, L. Wang, H. Zhu, S. Xu, X. He, G. Yin, C. Du, X. Sun, Adv. Energy Mater. 2019, 9, 1803963

[26] J. Li, C. Cao, X. Xu, Y. Zhu, R. Yao, $LiNi_{1/3}Co_{1/3}Mn_{1/3}O_2$ J. Mater. Chem. A. 2013, 1, 11848-11852

[27] Y, Gao, Z. Wang, G. Lu, J. Mater. Chem. A. 2019, 7, 2619-2625

[28] M. D. Radin, A. V. d. Ven, Chem. Mater. 2016, 28, 7898-7904

[29] J. Choi, K.-H. Kim, C.-H. Jung, S.-H. Hong, Chem. Commun. 2019, 55, 11575-11578

[30] T. He, L. Chen, Y. Su, Y. Lu, L. Bao, G. Chen, Q. Zhang, S. Chen, F. Wu, J Power Sources. 2019, 441, 227195

[31] H. Sun, K. Zhao, J. Phys. Chem. C. 2017, 121, 6002−6010

[32] M. Li, T. Liu, X. Bi, Z. Chen, K. Amine, C. Zhong, J. Lu, Chem. Soc. Rev. 2020, 49, 1688-1705

[33] A. Manthiram, B. Song, W. Li, Energy Storage Mater. 6, 125–139

[34] X. Zheng, X. Li, Z. Wang, H. Guo, Z. Huang, G. Yan, D. Wang, Electrochim. Acta. 2016, 191, 832-840

[35] H.-H. Sun, W. Choi., J. K. Lee, I.-H. Oh, H.-G. Jung, J. Power Sources. 2015, 275, 877-883

[36] C. Liang, F. Kong, R. C. Longo, C. Zhang, Y. Nie, Y. Zheng, K. Cho, J. Mater. Chem. A. 2017, 5, 25303-25313

[37] D. Streich, C. Erk, A. Guéguen, P. Müller, F. -F. Chesneau, E. J. Berg, J. Phys. Chem. C. 2017, 121, 13481−13486

[38] J. Zhu, S. Sharifi-Asl, J. C. Garcia, H. H. Iddir, J. R. Croy, R. Shahbazian-Yassar, ACS Appl. Energy Mater. 2020, 3, 4799−4811

[39] K. Min, K. Kim, C. Jung, S.-W. Seo, Y. Y. Song, H. S. Lee, J. Shin, E. Cho, J Power Sources. 2016, 315, 111-119

[40] W. E. Gent, Y. Li, S. Ahn, J. Lim, Y. Liu, A. M. Wise, C. B. Gopal, D. N. Mueller, R. Davis, J. N. Weker, J.-H. Park, S.-K. Doo, W. C. Chueh, Adv. Mater. 2016, 28, 6631–6638

[41] U.-H. Kim, L.-Y. Kuo, P. Kaghazchi, C. S. Yoon, Y.-K. Sun, ACS Energy Lett. 2019, 4, 576−582

[42] P. Yan, J. Zheng, M. Gu, J. Xiao, J.-G. Zhang, C.-M. Wang, Nat. Commun. 2017, 8, 14101

[43] S.-K. Jung, H. Gwon, J. Hong, K.-Y. Park, D.-H. Seo, H. Kim, J. Hyun, W. Yang, K. Kang, Adv. Energy Mater. 2014, 4, 1300787

[44] F. Kong, C. Liang, L. Wang, Y. Zheng, S. Perananthan, R. C. Longo, J. P. Ferraris, M. Kim, K. Cho, Adv. Energy Mater. 2019, 9, 1802586

[45] J. Zhu, S. Sharifi-Asl, J. C. Garcia, H. H. Iddir, J. R. Croy, R. Shahbazian-Yassar, G. Chen, ACS Appl. Energy Mater. 2020, 3, 4799−4811

[46] S. Sharifi-As, F. A. Soto, A. Nie, Y. Yuan, H. Asayesh-Ardakani, T. Foroozan, V. Yurkiv, B. Song, F. Mashayek, R. F. Klie, K. Amine, J. Lu, P. B. Balbuena, R. Shahbazian-Yassar, Nano Lett. 2017, 17, 2165−2171

[47] K. -W. Nam, S.-M. Bak, E. Hu, X. Yu, Y. Zhou, X. Wang, L. Wu, Y. Zhu, K.-Y. Chung, X.-Q. Yang, Adv. Funct. Mater. 2013, 23, 1047–1063

[48] S.-M. Bak, E. Hu, Y. Zhou, X. Yu, S. D. Senanayake, S. J. Cho, K.-B. Kim, K. Y. Chung, X.-Q. Yang, K.-W. Nam, ACS Appl. Mater. Interfaces. 2014, 6, 22594−22601

[49] D.-H. Cho, C.-H. Jo, W. Cho, Y.-J. Kim, H. Yashiro, Y.-K. Sun, S.-T. Myung, J. Electrochem. Soc. 2014, 161, A920-A926

[50] H.-J. Noh, S. Youn, C. S. Yoon, Y.-K. Sun, J. Power Sources. 2013, 233, 121-130

[51] N. P. W. Pieczonka, Z. Liu, P. Lu, K. L. Olson, J. Moote, B. R. Powell, J.-H. Kim, J. Phys. Chem. C. 2013, 117, 15947−15957

[52] N. V. Faenza, Z. W. Lebens-Higgins, P. Mukherjee, S. Sallis, N. Pereira, F. Badway, A. Halajko, G. Ceder, F. Cosandey, L. F. J. Piper, G. G. Amatucci, Langmuir. 2017, 33, 9333-9353

[53] C. Tian, Y. Xu, D. Nordlund, F. Lin, J. Liu, Z. Sun, Y. Liu, M. Doeff, Joule. 2018, 2, 464-477

[54] Z. Xu, Z. Jiang, C. Kuai, R Xu, C. Qin, Y. Zhang, M. M. Rahman, C. Wei, D. Nordlund, C.-J. Sun, X. Xiao, X. -W. Du, K. Zhao, P. Yan, Y. Liu, F. Lin, Nat. Commun. 2020, 11, 83

[55] Q. Xie, W. Li, A. Manthiram, Chem. Mater. 2019, 31, 938-946

[56] H. Li, P. Zhou, F. Liu, H. Li, F. Cheng, J. Chen, Chem. Sci. 2019, 10, 1374-1379

[57] C. S. Yoon, D.-W. Jun, S.-T. Myung, Y.-K. Sun, ACS Energy Lett. 2017, 2, 1150−1155

[58] S. Xia, L. Mu, Z. Xu, J. Wang, C. Wei, L. Liu, P. Pianetta, K. Zhao, X. Yu, F. Lin, Y. Liu, Nano Energy. 2018, 53. 753–762

[59] H.-H. Ryu, K.-J. Park, C. S. Yoon, Y.-K. Sun, Chem. Mater. 2018, 30, 1155−1163

[60] W. Li, H. Y. Asl, Q. Xie, A. Manthiram, J. Am. Chem. Soc. 2019, 141, 5097−5101

[61] A. O. Kondrakov, H. Geßwein, K. Galdina, L. d. Biasi, V. Meded, E. O. Filatova, G. Schumacher, W. Wenzel, P. Hartmann, T. Brezesinski, J. Janek, J. Phys. Chem. C. 2017, 121, 24381−24388

[62] P. Yan, J. Zheng, T. Chen, L. Luo, Y. Jiang, K. Wang, M. Sui, J. -G. Zhang, S. Zhang, C. Wang, Nat. Commun. 2018, 9, 2437

[63] L. Mu, R. Lin, Rong Xu, L. Han, S. Xia, D. Sokaras, J. D. Steiner, T. -C. Weng, D. Nordlund, M. M. Doeff, Y. Liu, K. Zhao, H. L. Xin, F. Lin, Nano Lett. 2018, 18, 3241-3249

[64] S. Ahmed, A. Pokle, S. Schweidler, A. Beyer, M. Bianchini, F. Walther, A. Mazilkin, P. Hartmann, T. Brezesinski, J. Janek, K. Volz, ACS Nano. 2019, 13, 10694−10704

[65] W. M. Seong, K. -H. Cho, J.-W. Park, H. Park, D. Eum, M. H. Lee, I. -S. Stephen Kim, J. Lim, Kisuk Kang, Angew. Chem. Int. Ed. 2020, 59, 18662-18669.

[66] R. Jung, M. Metzger, F. Maglia, C. Stinner, H. A. Gasteiger, J. Phys. Chem. Lett. 2017, 8, 4820-4825.

[67] D. Eum, B, Kim, S, J, Kim, H, Park, J, Wu, S.-P. Cho, G. Yoon, M. H. Lee, S. -K. Jung, W. Yang, W. M. Seong, K. Ku, O. Tamwattana, S. K. Park, I. Hwang, K. Kang, Nat. Mater. 2020, 19, 419–427.

[68] W. Zuo , M. Luo , X. Liu , J. Wu , H. Liu , J. Li , M. Winter , R. Fu , W. Yang, Y. Yang,

Energy Environ. Sci. 2020, DOI:10.1039/D0EE01694B.

[69] N. Li, S. Sallis, J. K. Papp, J. Wei, B. D. McCloskey, W. Yang, W. Tong, ACS Energy Lett. 2019, 4, 2836–2842.

[70] H. B. Xie, K. Du, G. R. Hu, Z. D. Peng, Y. B. Cao, J. Phys. Chem. C. 2016, 120, 3235-3241

[71] Z. Y. Chen, X. L. Gong, H. L. Zhu, K. F. Cao, Q. M. Liu, J. Liu, L. J. Li, J. F. Duan, Front. Chem. 2019, 6, 643

[72] Q. Q. Qiu, Z. Shadike, Q.C. Wang, X. Y. Yue, X. L. Li, S. S. Yuan S-S, F. Fang, X. J. Wu, A. Hunt, I. Waluyo, S. M. Bak, X. Q. Yang, Y. N. Zhou, ACS Appl. Mater. Interfaces. 2019, 11, 23213-23221

[73] J. H. Choi, S. Y. Lee, S. M. Yoon, K. H. Kim, M. Kim, S. H. Hong, ChemSusChem. 2019, 12, 2439-2446

[74] W. He, D. Yuan, J, Qian, X. Ai, H. Yang, Y. Cao, J. Mater. Chem. A. 2013, 1, 11397−11403

[75] F. Schipper, M. Dixit, D. Kovacheva, M. Talianker, O. Haik, J. Grinblat, E. M. Erickson, C. Ghanty, D. T. Major, B. Markovsky, D. Aurbach, J. Mater. Chem. A. 2016, 4, 16073-16084

[76] O. Breuer, A. Chakraborty, J. Liu, T. Kravchuk, L. Burstein, J. Grinblat, Y. Kauffman, A. Gladkih, P. Nayak, M. Tsubery, A.I. Frenkel, M. Talianker, D.T. Major, B. Markovsky, D. Aurbach, ACS Appl. Mater. Interfaces. 2018, 10, 29608-29621

[77] C. S. Yoon, U. H. Kim, G. T. Park, S. J. Kim, K. H. Kim, J. Kim, Y. K. Sun, ACS Energy Lett. 2018, 3, 1634-1639

[78] U. H. Kim, D. W. Jun, K. J. Park, Q. Zhang, P. Kaghazchi, D. Aurbach, D. T. Major, G. Goobes, M. Dixit, N. Leifer, C. M. Wang, P. Yan, D. Ahn, K. H. Kim, C. S. Yoon, Y. K. Sun, Energy Environ. Sci. 2018, 11, 1271-1279

[79] M. Eilers-Rethwisch, S. Hildebrand, M. Evertz, L. Ibinga, T. Daggera, M. Winter, F. M.

Schappacher, J. Power Sources. 2018, 397, 68-78

[80] M. D. Dixit, B. Markovsky, D. Aurbach, D. T. Major, J. Electrochem. Soc. 2017, 164, A6359-A6365

[81] P. Xiao, Z. Deng, A. Manthiram, G. Henkelman, J. Phys. Chem. C. 2012, 116, 23201

[82] S. J. Do, P. Santhoshkumar, S. H. Kang, K. Prasanna, Y. N. Jo, C. W. Lee, Ceram. Int. 2019, 45, 6972-6977

[83] K. J. Park, H. G. Jung, L. Y. Kuo, P. Kaghazchi, C. S. Yoon, Y. K. Sun, Adv. Energy Mater. 2018, 8, 1801202

[84] H. H. Ryu, G. T. Park, C. S. Yoon, Y. K. Sun, J. Mater. Chem. A. 2019, 7, 18580-18588

[85] G. T. Park, H. H. Ryu, N. Y. Park, C. S. Yoon, Y. K. Sun, J. Power Sources. 2019, 442, 227242

[86] Y. Shi, M. H. Zhang, D. N. Qian, Y. S. Meng, Electrochim. Acta. 2016, 203, 154-161

[87] H. Kim, J. Jang, D. Byun, H. S. Kim, W. Choi, ChemSusChem. 2019, 12, 5253-5264

[88] W. Liu, X. F. Li, D. B. Xiong, Y. C. Hao, J. W. Lia, H. R. Kou, B. Yan, D. J. Lia, S. G. Lu, A. Koo, K. Adair, X. L. Sun, Nano Energy. 2018, 44, 111–120

[89] J. Zhu, Y. Li, L. Xue, L. L. Xue, Y. X. Chen, T. X. Lei, S. Y. Deng, G. L. Cao, J. Alloys Compd. 2019, 773, 112-120

[90] S. W. Lee a, M. S. Kim, J. H. Jeong, D. H. Kim, K. Y. Chung, K. C. Roh, K. B. Kim, J. Power Sources. 2017, 360, 206-214

[91] H. J. Kim, S. H. Lee, H. Cho, J. H. Kim, J. Lee, S. H. Park, S. H. Joo, S. H. Kim, Y. G. Cho, H. K. Song, S. K. Kwak, J. P. Cho, Adv. Mater. 2016, 28, 4705–4712

[92] P. F. Yan, J. M. Zheng, J. Liu, B. Q. Wang, X. P. Cheng, Y. F. Zhang, X. L. Sun, C. M. Wang, J. G. Zhang, Nat. Energy. 2018, 3, 600–605

[93] G. L. Xu, Q. Liu, K. K. S. Lau, Y. Liu, X. Liu, H. Gao, X. Zhou, M. H. Zhuang, Y. Ren, J.

D. Li, M. H. Shao, M. G. Ouyang, F. Pan, Z. H. Chen, K. L. Amine, G. H. Chen, Nat. Energy. 2019, 4, 484–494

[94] Y. Lee, H. Kim, T. Yim, K. Y. Lee, W. Choi, J. Power Sources. 2018, 400, 87-95

[95] U. H. Kim, H. H. Ryu, J. H. Kim, R. B. Mücke, P. Y. Kaghazchi, C. S. Yoon, Y. K. Sun, Adv. Energy Mater. 2019, 9, 1803902

[96] L. Wang, B. Wu, D. Mu, X. Liu, Y. Peng, H. Xu, Q. Liu, L. Gai, F. Wu, J. Alloys Compd. 2016, 674, 360-367

[97] X. M. Fan, G. R. Hu, B. Zhang, X. Ou, J. F. Zhang, W. G. Zhao, ,H. P. Jia, L. F. Zou, P. Li, Y. Yang, Nano Energy. 2020, 70, 104450

[98] Y. J. Li, S. Wang, Y. Chen, T. X. Lei, S. Deng, J. Zhu, J. P. Zhang, J. Guo, Mater. Chem. Phys. 2020, 240 122029

[99] W. Yang, W. Xiang, Y. X. Chen, Zh. G. Wu, W. B. Hua, L. Q., F. R. He, J. Zhang, B. H. Zhong, X. D. Guo, ACS Appl. Mater. Interfaces. 2020, 12, 10240−10251

[100] C. L. Xu, W. Xiang, Z. G. Wu, Y. D. Xu, Y. C. Li, M. Z. Chen, G. XiaoDong, G. P. Lv, J. Zhang, B. H. Zhong, ACS Appl. Mater. Interfaces. 2018, 10, 27821−27830

[101] J. H. Kim, H. S. Ma, H. Y. Cha, H. Y. Lee, J. Y. Sung, M. H. Seo, P. G. Oh, M. J. Park, J. P. Cho, Energy Environ. Sci. 2018, 11, 1449-1459.

[102] H. H. Sun, H. H. Ryu, U. H. Kim, J. A. Weeks, A. Heller, Y. K. Sun, and C. B. Mullins, ACS Energy Lett. 2020, 5, 1136-1146.

[103] W. G. Zhao, J. M. Zheng, L. F. Zou, H. P. Jia, B. Liu, H. Wang, M. H. Engelhard, C. M. Wang, W. Xu, Y. Yang, J. G. Zhang, Adv. Energy Mater. 2018, 8, 1800297.

[104] J. H. Li, X. R. Yang, X. C. Guan, R. D. Guo, Y. X. Che, J. L. Lan, L. D. Xing, M. Q. Xu, W. Z. Fan, W. S. Li, Electrochim. Acta. 2020, 354, 136722.

Chapter 2.

Intrinsic design of Ni-rich layered cathode for Lithium ion batteries

2.1. Mitigation of Oxygen Oxidation through Zr Doping in Ni-rich Layered Oxide

2.1.1. Introduction

With the advent of electrical vehicles (EVs), there is a pressing demand to develop the lithium-ion battery (LIB) cathode materials with a high specific energy at a reduced cost [1,2]. In this sense, three-component $LiNi_xCo_yMn_{1-x-y}O_2$ (LNCM), which has the same crystal structure as the state-of-the-art $LiCoO_2$ layered oxide, has solidified its status as a cathode material of choice for EV battery systems [3,4]. To further boost the practical capacity of LNCM, research efforts are now focused on developing the LNCM materials with a high Ni content ($x \geq 0.9$), that is, Ni-rich layered oxides [5].

Nevertheless, the practical implementation of Ni-rich layered oxides is currently hindered by their continuous capacity fading and especially, the deterioration becomes increasingly severe with the increase of Ni content or at a high state of charge (SOC) [6,7,8]. Extensive researches have been performed to unveil the Ni-rich LNCM degradation mechanisms, which are reported to be abrupt anisotropic lattice contraction upon deep charge [9], structure and chemical instability [10,11], and electrolyte decomposition [12]. All of the above mechanisms concurrently operate from the particle surface to the bulk and jeopardize the successful application of Ni-rich LNCM.

As the mechanistic link between these failure mechanisms remains ambiguous, they have been perceived as independent phenomena; however, many reports have proposed and provided the evidence of the correlation between each mechanism when viewed on the atomic scale [13,14]. In particular, the instability of lattice oxygen upon deep charge is being

considered as the origin of the general capacity fading mechanism in layered oxides [15,16,17]. From the perspective of the crystal/electronic structure of layered oxides, cubic-closed-packed (ccp) oxygen layers serve as the backbone of the layered crystal structure while the Li and transition metal (TM) occupy the intestinal sites along the $[111]_{cubic}$ direction ($[001]_{hexagonal}$ direction) [18]. In this way, the 2p orbital of the oxygen ligand hybridizes with the TM 3d orbitals along the linear Li–O–TM configuration under octahedral symmetry [19]. By virtue of the TM(3d)–O(2p) hybridization, d holes generated on O 2p orbitals upon high SOC lead to the depletion of oxygen charge density and resultant oxygen instability [20-23], which accelerates the oxygen gas release [24], electrolyte oxidation [12,25], surface-reconstructed-layer (SRL) formation [26,27], sudden lattice contraction [28], and mechanical damage [14,29]. In this sense, it can be postulated that the stabilization of the lattice oxygen upon deep charge might be critical to improve the cycle life of Ni-rich layered cathodes.

Numerous strategies have been considered to promote the layered cathode cycle life including foreign doping [30], surface treatment [31], microstructure control [32], and compositional gradients [33]. Among the proposed strategies, the lattice doping is one of the most prevailing and suitable methodologies to address the aforementioned issues of Ni-rich LNCM. Despite some controversy surrounding the doping mechanisms, various dopants from low-valent Mg^{2+} to high-valent W^{6+} have been investigated for the layered cathodes [34,35]. In particular, Zr doping has been widely adopted for the layered oxides with various Ni contents, which is attributed to its effectiveness in improving the battery performance and its low cost [34, 36-40]. Even though the previous studies have verified the positive effect of Zr doping on the cathode electrochemical performance, there remains a significant lack of understanding the beneficial effects of Zr doping mechanism on Ni-rich layered oxides. Specifically, an in-depth study of the effects of Zr doping on the lattice oxygen stability upon deep charge has not yet

been performed. As detailed mechanistic investigations of the role of Zr incorporation are rare, unveiling of its fundamental origin in Ni-rich layered oxides is needed for the future design of cathode materials.

In this study, we provide the comprehensive analyses of the Zr doping effects in a $LiNi_{0.92}Co_{0.04}Mn_{0.04}O_2$ LIB cathode material with a focus on unveiling the critical origin of its mechanism. First, by combining spectroscopy and microscopy techniques, we show that Zr doping enhances the electrochemical performance of LNCM by affecting the abrupt c-axis contraction, particle cracks, oxygen evolution, electrolyte decomposition, and Li–Ni disorder, thus alleviating the diverse LNCM degradation factors. Then, the fundamental role of Zr doping is systematically investigated with the aid of state-of-the-art Squid-VSM, resonant inelastic X-ray scattering (RIXS), and scanning transmission X-ray microscopy (STXM) analyses. According to the measurements, it is revealed that Zr doping suppresses the oxygen oxidation upon high SOC, which is associated with the oxygen instability and the aforementioned degradation factors. These experimental findings are further collaborated by first-principles calculations showing that the Zr doping was effective in alleviating the oxygen charge depletion upon high SOC. Based on the obtained results, we focus on discovering the true mechanism of Zr cation doping on Ni-rich layered cathodes for its future successful application.

2.1.2. Results and discussion

The crystal structure of as-synthesized undoped and Zr-doped $LiNi_{0.92}Co_{0.04}Mn_{0.04}O_2$ powders (denoted as U-LNCM and Zr-LNCM, respectively) was determined using high resolution powder diffraction (HRPD) (Figure 2.1a, b). All the

diffraction peaks were indexed based on the hexagonal α-$NaFeO_2$-type layer structure (space group R-3m) without a secondary phase [35]. The Rietveld refinement results indicated that the lattice parameters and unit-cell volume slightly increased with Zr doping, indicating that Zr^{4+} was successfully incorporated into the LNCM lattice (Figure 2.1c). The increase of lattice constants can be attributed to the larger ionic radius of Zr^{4+} (0.72 Å , CN (coordination number) = 6) compared with that of Ni^{2+} (0.69 Å), Co^{3+} (0.545 Å), and Mn^{4+} (0.53 Å) with CN=6 [37,41]. The relative mole fraction of Ni: Co: Mn was close to the nominal composition of 92: 4: 4 in both LNCM powders, and the Zr doping concentration was estimated to be approximately 1 mol% by the ICP-AES measurements. The SEM images of as-synthesized U-LNCM and Zr-LNCM revealed that both powders were more or less spherical with a diameter of 7–8 μm and were composed of densely packed primary particles of ~500 nm (Figure 2.1d, e). Apparently, Zr doping had no effect on the morphology and size of the primary/secondary particles. The EDS mapping on the cross-sectioned polished particles showed that Zr was homogeneously distributed throughout the particles (Figure 2.1f), indicating that Zr was uniformly incorporated into the LNCM crystal structure.

After confirming the Zr doping, as-synthesized powders were prepared into a slurry and coated on Al foil using the doctor blade method for the electrochemical testing. The electrochemical reactions of U-LNCM and Zr-LNCM electrodes were evaluated using 2032 coin-type half-cells in the potential range of 2.5–4.4 V (vs. Li/Li^+) (Figure 2.2). The electrodes had similar initial charge/discharge voltage profiles and delivered similar initial discharge capacities (U-LNCM: 230.1 mAh g^{-1} and Zr-LNCM: 225.2 mAh g^{-1}) at a current density of 0.1 C (1 C= 200 mA g^{-1}) (Figure 2.2a). The slightly lower discharge capacity of Zr-LNCM electrode was resulted from the incorporation of electrochemically inactive Zr [39]. However, the capacity retention of U-LNCM electrode was significantly improved with the introduction

of Zr. After 100 cycles at a current density of 0.3 C, approximately 83% of the initial capacity was retained in the Zr-LNCM electrode, whereas the U-LNCM electrode retained only 68% of its initial capacity (Figure 2.2b). When the current density was lowered to 0.1 C at the last cycle, the U-LNCM electrode delivered a capacity of 177.5 mAh g^{-1}, whereas the Zr-LNCM electrode delivered a much higher capacity of 220.4 mAh g^{-1}. In addition, 0.5, 1.5, and 2.0 mol% Zr-doped LNCM powders were prepared, and their cycle performance was investigated (Figure 2.2c). After 100 cycles at 0.3 C, the reversible capacity was highest for the 1.0 mol% Zr-doped LNCM electrode, and thus, the subsequent analysis was conducted on this electrode. Furthermore, Zr doping improved the rate capability of LNCM, as shown in Figure 2.2d. The discharge capacity of both electrodes steadily decreased with the stepwise increase of current density; however, the Zr-LNCM electrode delivered a higher discharge capacity at all the current densities, exhibiting the enhanced rate performance compared to the U-LNCM electrode. In particular, at the high current density of 2 C, the Zr-LNCM electrode delivered a high discharge capacity of 162.2 mAh g^{-1}, whereas the U-LNCM electrode only delivered a discharge capacity of 110.4 mAh g^{-1}. To determine the reason for the superior rate capability of Zr-LNCM electrode, the lithium-ion diffusion coefficient (D_{Li}^{+}) was measured using the galvanostatic intermittent titration technique (GITT). The GITT measurement was performed by applying a current pulse of 0.2 C for 10 min to obtain the closed-circuit voltage (CCV) and subsequently resting for 1 h to obtain the quasi-open-circuit voltage (QOCV). Compared to the U-LNCM electrode, the Zr-LNCM electrode exhibited higher D_{Li}^{+} at all potentials (Figure 2.2e). In particular, the sudden decrease of D_{Li}^{+} at ~4.15 V was significantly alleviated in the Zr-LNCM electrode; that is, ~90% of the lithium mobility decreased in U-LNCM, whereas only 54% decreased in the Zr-LNCM electrode. As the sudden decrease of D_{Li}^{+} at high potential was induced by the collapse of Li slab during the H2→H3 phase transition [28,35], the GITT

results indicate that Zr doping alleviated the abrupt c-axis contraction during the phase transition, which positively contributed to the enhanced kinetics as well as cycle stability.

As the electrochemical stability of Ni-rich layered oxides is closely associated with the phase transitions during the charging process, *in-situ* XRD analysis was conducted to monitor the phase and structure evolution during delithiation (Figure 2.3a). The electrodes were charged to 4.4 V (vs. Li/Li^+) at a current density of 0.2 C using the modified coin-type cell with 3 mm hole at its center sealed with mylar film. The electrodes were pre-cycled before the measurements, and the diffraction patterns were recorded every 10 min. During an early stage of delithiation, the $(003)_{H1}$ peak gradually shifted to lower 2θ for both electrodes. The shift of $(003)_{H1}$ peak to a lower 2θ indicates an enlargement of the c-axis, which is attributed to the increase of oxygen–oxygen repulsion due to a diminishing lithium-screening effect within the Li slab [44]. However, upon further delithiation, the $(003)_{H2}$ peak rapidly shifted toward higher 2θ, which implies the sudden lattice collapse along the c-axis direction. The U-LNCM electrode exhibited a peak shift of 1.06° at high SOC, whereas a smaller peak shift of 0.88° was observed for the Zr-LNCM electrode. Thus, Zr doping effectively alleviated the c-axis contraction at high SOC, implying that the incorporation of Zr into the crystal lattice noticeably mitigated the intrinsic structural change associated with the multiple phase transitions during charging. Furthermore, as the sudden lattice contraction localizes the stress within the secondary particle that could lead to the particle crack formation/propagation, it is expected that the Zr-LNCM electrode would be more resistant against the mechanical fracture [45]. Thus, to visualize the effect of Zr incorporation on the crack formation, the microstructures of pristine and cycled electrodes were investigated using the cross-sectional SEM. For both U-LNCM and Zr-LNCM pristine electrodes, no obvious crack or disintegration was observed and the primary particles were closely attached to each other (Figure 2.3b). However, a manifest difference

between U-LNCM and Zr-LNCM was observed after multiple cycling (Figure 2.3c). For the cycled U-LNCM, primary particles were disintegrated from each other, and some of the cracks were propagated from the particle surface toward the inner bulk. These cracks provide a pathway for the electrolyte infiltration, and the direct exposure of in-grain primary particles to the electrolyte would provoke the unwanted parasitic reactions within the inner bulk and thus increase the cell impedance [9,46]. In contrast, no visible structural collapse was detected for the cycled Zr-LNCM, and only minor particle disintegration was observed, which is attributed to the alleviation of sudden c-axis contraction upon high SOC. These results indicate the superior effects of Zr doping in stabilizing the intrinsic and extrinsic structural collapse of LNCM that are associated with the sudden c-axis contraction during the multiple cycling.

As the Ni-rich layered oxides are deteriorated by multiple degradation mechanisms besides the structural collapse, further analyses were conducted employing STEM-EELS, DEMS, and STEM imaging to elucidate the origin of the enhanced cycle performance in the Zr-LNCM electrode. Considering the strong correlation between surface degradation and cathode deterioration, we first examined the electronic states of the cycled electrodes using electron energy loss spectroscopy (EELS). The change of the oxidation states was determined by probing the TM L-edge and O K-edge EELS spectra [47]. Specifically, the change of the peak position in the TM L spectrum and the absence/decrease of the pre-edge peak in the O K spectrum can be utilized to trace the change of the TM valence state and detect the oxygen loss from the particle, respectively [48,49]. Among the TM L-edges, only Ni L-edge was examined as Ni is more than 92% in this study and acts as a main culprit for the continuous capacity fading in Ni-rich layered cathodes. The EELS spectra were obtained by performing the line scan from the surface to the bulk in the 50^{th} cycled U-LNCM and Zr-LNCM electrodes along the same crystallographic orientation. For both U-LNCM (Figure 2.4a) and Zr-LNCM (Figure

2.4b), the surface L_3 peaks of the Ni L-edge were positioned at lower energy compared with that of the bulk, indicating the reduction of the Ni valence state at the particle surface [48]. The L-edge peaks smoothly shifted toward higher energy when scanning from the surface to the bulk, and the bulk values were obtained at 8–9 nm and 4 nm from the surface for U-LNCM and Zr-LNCM, respectively. This result implies that U-LNCM had undergone more severe Ni reduction at the particle surface than Zr-LNCM. Likewise, the O pre-edge peak was absent at the surface, which was clearly different with the bulk peak. However, the pre-edge peak gradually evolved and the intensity increased when moving from the surface to the bulk. The O pre-edge peak recovered its bulk peak at 8–9 and 4 nm from the surface for U-LNCM and Zr-LNCM, respectively. Thus, the intensity reduction of the O K pre-edge peak corresponded well to the shift of the L_3-edge peak position in both electrodes. As the oxygen vacancy formation is accompanied by the TM reduction for charge balance [50], both EELS Ni L-edge and O K-edge spectra imply that Zr-LNCM was more resistant to the oxygen-vacancy formation during cycling than U-LNCM. After confirming the positive effect of Zr doping on the oxygen-vacancy formation, *operando* differential electrochemical mass spectrometry (DEMS) was conducted to compare the gas evolution rate during the charge process. The DEMS measurements were performed at a current density of 0.1 C with a high mass loading of ~10 mg cm^{-2}. For both cathodes, the O_2 gas was detected after the H2 phase, and the gas evolution increased upon further increasing the charge potential (Figure 2.4c). The rapid increase of gas evolution upon increasing the charge potential is due to the unstable LNCM layered structure in the high delithiated state [25]. Furthermore, the CO2 gas, which is produced by the electrolyte decomposition from the released singlet oxygen from LNCM [12,17], was concurrently evolved with the O_2 gas, and the rate also increased with increasing the charge voltage (Figure 2.4d). Meanwhile, the Zr doping delayed the onset time of gas evolution and

reduced the rate of O_2 gas evolution compared to those for U-LNCM (Figure 2.4c). In addition, the CO_2 gas evolution was mitigated, indicating that the chemical oxidization of the electrolyte was effectively suppressed by the Zr doping (Figure 2.4d). Thus, the *operando* DEMS results further confirmed that Zr doping of LNCM alleviated the oxygen gas release as well as the electrolyte decomposition. Finally, the surface of the cycled LNCM electrodes were examined using atomic-resolution STEM to reveal the structure transformation resulting from the oxygen loss. After 50 cycles at 0.3 C, the bulk retained its original R-3m layered structure for both electrodes; however, the SRL on the particle surface significantly propagated toward the inner bulk, which was indexed as the NiO-like rock salt (Fm-3m) phase using the fast Fourier transform (FFT) pattern (Figure 2.4e, f). The thickness of the SRL was estimated to be ~8 and ~4 nm for U-LNCM and Zr-LNCM, respectively; thus, Zr doping also alleviated the detrimental cation mixing during cycling.

Overall, by adopting various analysis techniques, we have uncovered that Zr doping enhanced the LNCM electrochemical performance by alleviating the diverse LNCM degradation factors, including abrupt c-axis contraction, microcrack formation, oxygen release, electrolyte decomposition, and Li–Ni cation mixing. These factors continuously degraded the LNCM during the multiple cycles and resulted in the impedance rise, as confirmed by the EIS measurements (Figure 2.5). The charge-transfer resistance (R_{ct}) of U-LNCM progressively increased from 334 Ω (5^{th} cycle) to 2122 Ω (100^{th} cycle at 0.3 C), whereas that of Zr-LNCM marginally increased from 258 Ω (5^{th} cycle) to 723 Ω (100^{th} cycle at 0.3 C). Therefore, the EIS measurements further confirmed the positive effect of Zr doping on alleviating the degradation of the Ni-rich layered cathode.

So far, we have shown that Zr doping substantially enhanced the cycle and rate performance of LNCM, and by combining microscopy and spectroscopy techniques, we revealed that the Zr

dopant alleviated most of well-known degradation factors of Ni-rich layered cathodes. Our discussion mainly focuses on determining the fundamental origin of the Zr doping mechanism in Ni-rich layered cathodes. The instability of lattice oxygen upon deep charge has been proposed as one of the critical origins of the general capacity decay in the layered oxides. The lattice oxygen instability is due to the oxygen charge depletion ($O^{2-} \rightarrow O^{-2+\delta}$) resulting from the O→Ni charge transfer mechanism, which activates the Li–O collapse (lattice contraction along the c-axis) and oxygen gas evolution [12,16,17,28]. The sudden Li–O collapse localizes the stress within the secondary particle, which could develop into the microcrack formation [45]. The release of oxygen gas leaves an oxygen vacancy within the layered oxide, providing a Ni migration pathway that accelerates the cation mixing [51]. Furthermore, the released oxygen is in the highly reactive singlet oxygen gaseous state that reacts and chemically decomposes the electrolyte [17]. Therefore, as the instability of lattice oxygen triggers the various degradation mechanisms of Ni-rich layered oxides and can be considered as the critical degradation origin, the investigation of Zr doping on the oxygen stability is needed to fully understand the Zr doping on the layered cathodes.

To obtain insight into the oxygen charge transfer involved in the delithiation process, the magnetic moment of the charged samples was collected by Squid-VSM analysis. Note that Squid-VSM analysis detects the bulk magnetic moment of the sample [52]. The paramagnetic effective moment (μ_{eff}) of the charged sample can be extracted from the temperature dependence of the reciprocal magnetic susceptibility $\chi^{-1}(T)$ [53-56]. Briefly, an increase of the slope in the curve of χ^{-1} vs. T indicates a decrease of the magnetic moment of the sample [56-58]. In Ni-rich LNCM, Ni acts as a main redox center with the oxidation state Ni^{3+} (electronic configuration: $t_{2g}^6 e_g^1$) for the pristine electrode, whereas it oxidizes to Ni^{4+} (electronic configuration: $t_{2g}^6 e_g^0$) during delithiation. Therefore, as the unpaired electron in the e_g band is

removed from Ni during the delithiation process, it is expected that the magnetic moment of the sample would decrease upon charge, thereby increasing the slope in the χ^{-1} vs. T curve. The SOC positions at which the measurements were taken are shown in Figure 2.6a. From the obtained χ^{-1} vs. T measurements, the samples followed the Curie–Weiss law $\chi=C/(T-\Theta)$, where C is the Curie constant and Θ is the Curie−Weiss temperature (Figure 2.6b, c). Based on the previous reports, the temperature region of 100–250 K was fitted to the Curie–Weiss law to obtain the paramagnetic effective moment [56,57]. As expected, during the early stage of delithiation, the slope of $\chi^{-1}(T)$ curve increased with increasing SOC for both U-LNCM (Figure 2.6b) and Zr-LNCM (Figure 2.6c). However, when the SOC reached x=0.88 ($Li_{1-x}MO_2$, x=0.88 corresponds to the capacity obtained when 4.4 V charged), a sudden decrease of the slope was observed for U-LNCM. The calculated paramagnetic effective moment (μ_{eff}) steeply increased over 40% at x=0.88 for U-LNCM (Figure 2.6d). Several scenarios were considered (cation-mixing or cobalt redox), and it was determined that the increase of the magnetic moment can be explained by the oxygen charge transfer mechanism, which produces the abundant unpaired electrons within oxygen and nickel that could contribute to the dramatic increase of μ_{eff} (Figure 2.6e) [53,56,59]. In contrast, for Zr-LNCM, the increase of slope at x=0.88 was not dramatic compared to that of U-LNCM, showing only a 14% increase of μ_{eff} (Figure 2.6c, d). The above results indicate that Zr doping effectively restrained the charge transfer between O and Ni.

The above Squid-VMS results are further evidenced by mapping of resonant inelastic X-ray scattering (mRIXS) (Figure 2.7a), which has been demonstrated as a tool-of-choice to detect the oxidized oxygen in the bulk lattice of battery cathodes due to its ability to deconvolute the oxidized oxygen and TM-O hybridization signals [60-64]. In particular, the feature around 531.0 and 523.7 eV excitation and emission energy (marked by pink arrows), respectively, is a fingerprint of oxidized oxygen in the battery electrodes. Additionally, this fingerprint feature

always shows up together with the enhanced intensity close to the elastic peak (marked by yellow arrows) [60-64]. The mRIXS results showed that the oxidized oxygen feature was not observed until x=0.8 ($Li_{1-x}MO_2$) for both U-LNCM and Zr-LNCM, but emerged at x=0.88 for U-LNCM; in contrast, Zr-LNCM showed a negligible feature even at high SOC (Figure 2.7a). Moreover, the low energy loss feature (marked by yellow arrows) close to the elastic peak of U-LNCM electrode displayed the enhanced intensity than the Zr-LNCM electrode at x=0.88. For a more direct comparison, super-partial fluorescence yield (sPFY) spectra, which are obtained by integrating the intensity within the emission energy window around 523.7 eV ± 1 eV of mRIXS data [63,64], has been conducted at x=0.88. As shown in Figure 2.7b, the fingerprinting peak of oxidized oxygen at 531 eV was clearly observed for U-LNCM whereas it was hardly observed in Zr-LNCM, further implying that more oxidized oxygen was present in U-LNCM compared to Zr-LNCM at high SOC. After confirming the difference in the oxidized oxygen between U-LNCM and Zr-LNCM, we investigated the change of the Ni valence state during delithiation. Figure 2.7c shows the variation of the Ni L_3-edge absorbance spectra obtained using scanning transmission X-ray microscopy (STXM). When charged from x=0 ($Li_{1-x}MO_2$) to x=0.8, the intensity of the peak at ~855 eV increased for both U-LNCM and Zr-LNCM, indicating an increase of the Ni valence state [65]. However, upon deep charge at x=0.88, the intensity of the peak at 855 eV significantly decreased compared to that at x=0.8 in U-LNCM, whereas a minimal peak change was observed for Zr-LNCM. These results indicate that Ni in U-LNCM underwent a severe valence reduction at x=0.88, where the oxidized oxygen was present. Overall, by combining mRIXS and STXM analyses, it is evident that the O→Ni charge transfer is involved in U-LNCM upon delithiation and that Zr doping effectively mitigated this phenomenon.

To gain a fundamental understanding of Zr doping effect on the oxygen charge evolution of

LNCM cathodes, we performed the first-principles calculations using the projector augmented wave (PAW) method. The $Li_{1-x}NiO_2$ model system was used for the density functional theory (DFT) calculations as the Ni content was over 90% in this study. Zr was positioned on the Ni site according to the previous reports [38,41]. The evolution of oxygen charge density was evaluated by varying the lithium content in the $Li_{1-x}NiO_2$ system and the oxygen charge density was compared between oxygen atoms near Zr atom and those far from Zr atom. The number around the oxygen atoms in Figure 2.7e and Figure 2.7f indicates the oxygen charge loss upon delithiation. On deep charging (x=0.84), O atoms are under a charge deficiency state compared to that at x=0 (pristine state) (Figure 2.7e, f), which matches well with the previous reports [28,66]. However, the calculation results showed that O atoms near Zr atom (Figure 2.7f) lost less charge density compared to those of O atoms far from Zr atom (Figure 2.7e). Therefore, the DFT calculations were consistent with the experimental results, showing that Zr doping was effective in restraining the oxygen charge loss upon deep charge. Previous first-principles calculations revealed that high-valent dopants (W, Ta, Ti, etc.) can stabilize the lattice oxygen owing to the strong electron hybridization effect with the oxygen in the layered oxide system [67,68]. In addition, experimental studies have shown that these dopants enhanced the Ni-rich layered cathode cyclability by alleviating the lattice contraction, crack propagation, oxygen evolution, and surface reconstruction [2-5]. In particular, the stabilization of lattice oxygen by Ti doping has been previously evidenced by mRIXS and DFT calculation, with similar results as those for Zr doping [66]. Based on these results, the effect of Zr doping on the oxygen stability can be rationalized as strong Zr–O hybridization through high-valent Zr^{4+}.

Thus far, we have unveiled that the oxygen charge-transfer mechanism was involved in the high SOC state of LNCM and that Zr doping successfully mitigated this phenomenon. When the charge is transferred from O→Ni, a hole resides on the oxygen that leads to the instability

of lattice oxygen. Furthermore, the instability of lattice oxygen can provoke lattice collapse and oxygen evolution, which can additionally cause particle cracking and electrolyte decomposition, eventually leading to the capacity fading. However, as the Zr doping effectively mitigates the oxygen charge transfer, the oxidation of oxygen at high SOC could be relatively suppressed compared to the undoped cathode, thus possibly alleviating the following-up degradation mechanisms. To prove this, the temperature-resolved heating XRD analysis was performed for both 4.4 V charged U-LNCM and Zr-LNCM electrodes. For U-LNCM, the sample was fully decomposed at 480 ℃ while the decomposition temperature was delayed to 520 ℃ in Zr-LNCM (Figure 2.8). As the thermal decomposition of the charged cathode is induced by the instability of the lattice oxygen framework [13,69], the delay of decomposition through Zr doping indicates a relatively stabilized lattice structure by the relaxation of oxygen charge transfer. Therefore, by combining the obtained results in this study, we propose “lattice oxygen stabilization” as the potential origin of the Zr doping mechanism.

2.1.3. Conclusion

Herein, an in-depth study was conducted to unveil the Zr doping mechanism in Ni-rich layered cathodes for LIBs. First, by combining various spectroscopic techniques, we showed that Zr doping enhanced the Ni-rich LNCM electrochemical performance by alleviating most of the well-known LNCM degradation factors starting from the surface to the bulk. Then, to determine the true origin of the doping mechanism, Squid-VSM along with state-of-the-art mRIXS were selected as the tools of choice to clarify the role of Zr doping. From the analysis, we uncovered that the oxygen charge-transfer mechanism was involved in the LNCM deep charge state, causing sudden lattice contraction as well as other degradation factors. However,

when Zr was incorporated into the LNCM crystal structure, the oxygen charge transfer was effectively mitigated, thus aiding in suppressing the subsequent degradation mechanisms to enhance the cathode cycle life. Therefore, the obtained results suggest the importance of examining the relationship between dopant and lattice oxygen stability to unveil its mechanism. This work enhances our understanding of the doping effects in Ni-rich layered oxides and provides insight for further improvements in state-of-the-art Li ion battery cathode materials

2.1.4. Experimental procedure

Materials preparation

$Ni_{0.92}Co_{0.04}Mn_{0.04}(OH)_2$ hydroxide was synthesized by a co-precipitation method using $NiSO_4 \cdot 6H_2O$ (Daejung Chemical Co.), $CoSO_4 \cdot 7H_2O$ (Daejung Chemical Co.), $MnSO_4 \cdot H_2O$ (Daejung Chemical Co.), NaOH (Daejung Chemical Co.), and NH_4OH (Daejung Chemical Co.). The mixed solution (Ni: Co: Mn= 92: 4: 4 in molar ratio) was pumped into the reactor containing a solution of NaOH (aq) and NH_4OH (aq) under N_2 atmosphere. Simultaneously, NaOH (molar ratio of NaOH/TM=2.0) and NH_4OH (molar ratio of NH_4OH/TM=1.2) were separately fed into the reactor. Afterwards, the hydroxide precursor was obtained by filtering, washing, and vacuum drying the precipitate for overnight. To prepare the undoped LNCM (U-LNCM), the hydroxide precursor was mixed with $LiOH \cdot H_2O$ (precursor: Li=1: 1.03 in molar ratio) and calcined at 740 °C for 12 h under an oxygen flow. For the synthesis of Zr-doped LNCM (Zr-LNCM), the hydroxide precursor was first coated with Zr source using zirconium butoxide solution (Sigma-Aldrich) and acetylacetone (Sigma-Aldrich). In detail, zirconium butoxide solution and acetylacetone (1: 4 in mole ratio) was first homogenously mixed in dehydrated ethanol for 30 min. Then, the hydroxide precursor (Zr: NCM=1: 99 in mole ratio)

was added into the solution, stirred for 30 min, filtered, and then, dried under 100 °C overnight. Finally, to obtain the Zr-LNCM, the dried powder was mixed $LiOH \cdot H_2O$ with a molar ratio of 1: 1.03 and calcined at the same conditions with the U-LNCM.

Characterization

The chemical composition of the prepared LNCM was determined by inductively coupled plasma-atomic emission spectroscopy (ICP-AES) (OPTIMA 4300DV, PerkinElmer). The crystal structure and lattice parameters were determined by synchrotron radiation powder X-ray diffraction (HRRD), which was collected at room temperature from the 9B HRPD beamline at the Pohang Accelerator Laboratory (PAL). Fullprof program was used for the Rietveld refinement. The *in-situ* battery cell X-ray diffractometer (R-AXIS IV, RIGAKU) was used to observe the phase transitions during charging with a modified coin-type cell (3 mm hole at its center sealed with mylar film). The electrodes were pre-cycled before the measurement. The *in-situ* XRD was conducted by charging the voltage up to 4.4 V vs Li/Li^+ with a 0.2 C current density while the diffraction patterns were recorded every 10 min. For the after cycled analyses (temperature-resolved XRD, SEM, TEM, EELS, Squid-VSM, STXM, mRIXS, and sPFY), the coin-cells were dissembled in a glove box after the cells reached the designated SOC (x=0.8, x=0.88, $Li_{1-x}NiO_2$) or after 50 cycles. Then, the dissembled electrodes were washed in DMC (dimethyl carbonate) to remove the residual lithium salt. For the temperature-resolved XRD (X'Pert PRO, KIST) measurement, the XRD patterns were collected while heating the sample from room temperature to 600 °C with a heating rate of 8 °C /min under the He carrier-gas flow. The SEM (SU-70, Hitachi) and TEM (JEM-2100F, JEOL) were used to observe the particle morphology. The high-resolution STEM images and electron energy loss spectroscopy (EELS) data were collected from the double aberration-corrected JEOL-ARM 200CF microscope with

a cold-field emission gun operated at an acceleration voltage of 200 kV. The cross sectioned samples were prepared by FIB (Helios Nano Lab450, FEI) and cross-section polisher (IB-19510CP, JEOL) for TEM and SEM analyses, respectively. For Squid-VSM analysis (QM02, magnetic property measurement system), the cathode material was scratched off from the current collector and ~20 mg of powders was used for the analysis. The temperature-dependent magnetic moment was measured by varying the temperature from 5 K to 300 K. The magnetic susceptibility was calculated by dividing the magnetization by the magnetic field. To obtain the Ni L_3-edge spectra, scanning transmission X-ray microscopy (STXM) analysis was performed at beamline 10A at the PAL. For the STXM analysis, DMC washed electrodes were scarapped of the electrodes and further sonicated in DMC solvent for ~30 min. Then, the solvent was drop-cast onto carbon-coated Cu TEM grid for the STXM measurement. Mapping of resonant inelastic X-ray scattering (mRIXS) was measured in iRIXS endstation at BL8.0.1 of the Advanced Light Source at Lawrence Berkeley National Laboratory. The emission and excitation energy resolutions were about 0.3 and 0.2 eV, respectively, without considering the core-hole life time broadening. Data were collected with an excitation energy step of 0.2 eV across the whole O K-edge range. O-K mRIXS-sPFY data were collected by integrating the mRIXS intensity within the emission energy from 523 to 525 eV.

Electrochemical Test

The electrochemical properties were analyzed with 2032 coin-type cells (Welcos, Korea), which were fabricated in Ar-filled glove box. The positive electrodes were prepared by casting a slurry mixed with active material, Super P, and polyvinylidene fluoride (PVDF) binder (85:8:7 in weight ratio) onto an Al foil with a mass loading of ~8 mg cm^{-2}. The cell was fabricated using Li-metal as a counter electrode with a separator film (Celgard) filled with

$LiPF_6$ (1.2 M) solution dissolved in an ethyl carbonate-ethyl methyl carbonate mixture (3:7 *v*/*v*). The half-cells were tested at voltage between 2.5 and 4.4 V vs Li/Li^+ at room temperature using automatic battery cycler (WBCS 3000S WonATech). The current density of 1 C represents 200 mA g^{-1}. For the galvanostatic intermittent titration technique (GITT) measurement, the half-cell was applied 0.2 C current for 10 min and subsequently rested for 1 h (voltage range 2.5~4.4 V). The EIS (ZIVE SP1 potentiostat/galvanostat/EIS) analysis were taken in a frequency range of 1000 kHz~5 mHz with an AC amplitude of 10 mV. To prepare the electrodes for the differential electrochemical mass spectrometry (DEMS) analysis, the obtained powders were prepared into the slurry and casted onto the Al mesh (AL008772, Goodfellow) with ~10 mg cm^{-2} mass loading. Then, the cathodes were fabricated in a glove box using Li metal as counter electrode. The details for DEMS experimental setup are provided elsewhere [70]. For the DEMS analysis, the cell was charged to 4.8 V with a 0.1 C current density.

First Principles Calculations (DFT)

All calculations in this work were performed based on spin-polarized density functional theory (DFT) implemented in Vienna ab-initio simulation package (VASP) [71]. Projector augmented wave (PAW) pseudo-potentials were used and all energies were calculated within spin-polarized generalized gradient approximation with Hubbard-U (GGA+U) parametrization using Perdew-Burke-Ernzerhof (PBE functional) [72,73]. The onsite Coulomb parameter U of 6.4 was applied to nickel 3d electrons according to the value in the previous works [74]. A kinetic energy cutoff of the plane-wave basis set was 500 eV and a 2×2×1 k-points monkhorst-pack grids were utilized for the bulk relaxation ($Li_{12}Ni_{11}Zr_1O_{24}$) so that the structures were fully

relaxed within the interatomic forces smaller than 0.02 eV/Å. To describe the delithiated states ($Li_2Ni_{11}Zr_1O_{24}$ and $Li_4Ni_{11}Zr_1O_{24}$), the 30 lowest energy configurations were chosen for each delithiated state using Ewald summation [75,76].

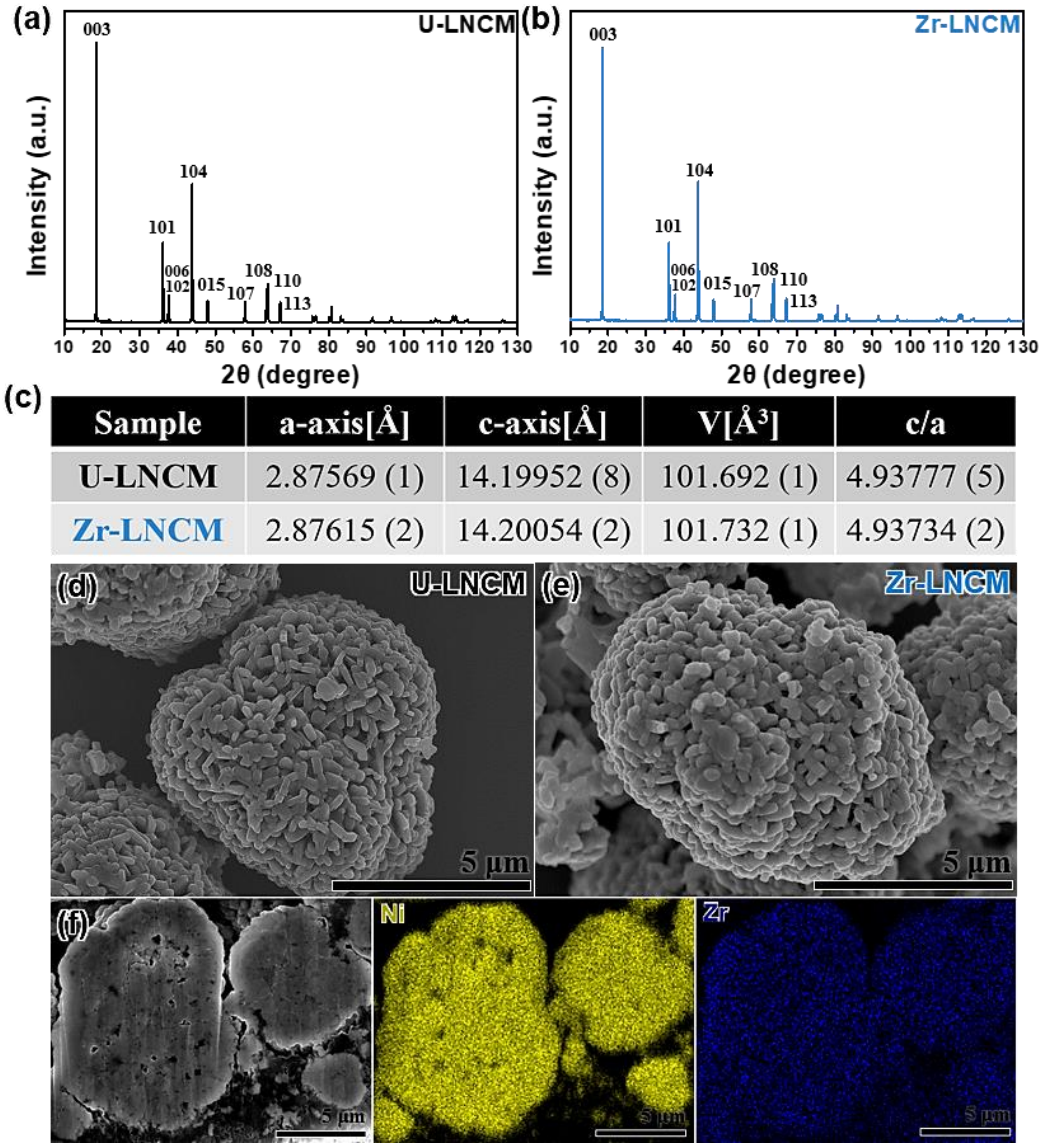

(c)

Sample	a-axis[Å]	c-axis[Å]	V[Å³]	c/a
U-LNCM	2.87569 (1)	14.19952 (8)	101.692 (1)	4.93777 (5)
Zr-LNCM	2.87615 (2)	14.20054 (2)	101.732 (1)	4.93734 (2)

Figure 2.1. HRPD patterns of as-synthesized (a) U-LNCM and (b) Zr-LNCM powders. (c) The Reteiveld refinement results of as-syntheiszed powders. SEM images of (d) U-LNCM and (e) Zr-LNCM. (f) Cross-sectioned polished SEM image of Zr-LNCM and its EDS mapping data.

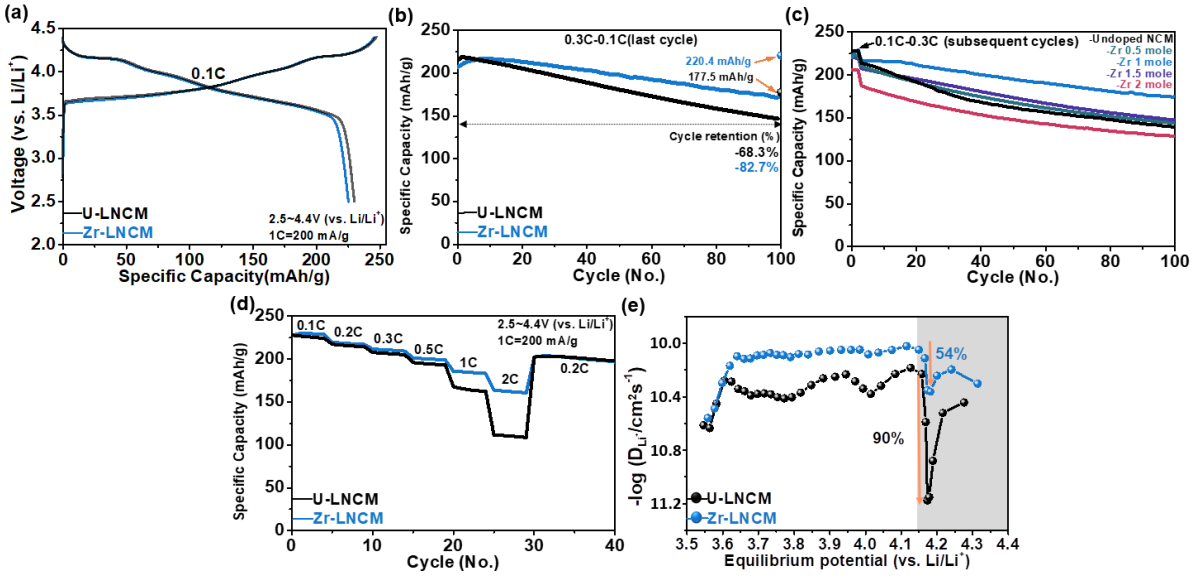

Figure 2.2. (a) Initial charge-discharge voltage profiles for U-LNCM and Zr-LNCM electrodes between 2.5 and 4.4 V (vs. Li^+/Li) at the current density of 0.1 C (1 C= 200 mA g^{-1}). (b) Cycle performance of U-LNCM and Zr-LNCM electrodes at the current density of 0.3 C for 100 cycles, while 0.1 C current density was applied at 101^{th} cycle. (c) Cycle comparision between the various Zr mole % doped LNCM. (d) Rate performance of the electrodes by varying the current density from 0.1 to 2 C. (e) The calculated lithium ion mobility of U-LNCM and Zr-LNCM by using GITT analysis.

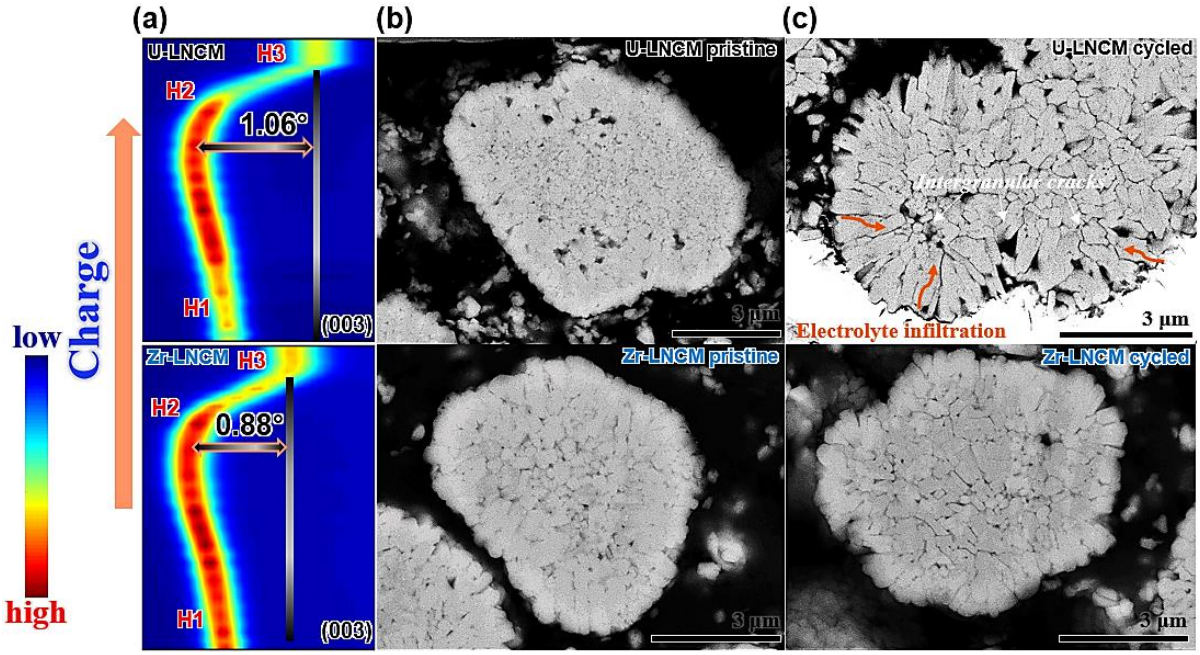

Figure 2.3. (a) *In situ* XRD patterns of U-LNCM and Zr-LNCM electrodes during charge process at current density of 0.2 C. Cross-sectioned polished SEM images of (b) pristine U-LNCM, Zr-LNCM and after 50th cycled (c) U-LNCM, Zr-LNCM electrodes. The upper data corresponds to U-LNCM while the below are Zr-LNCM data.

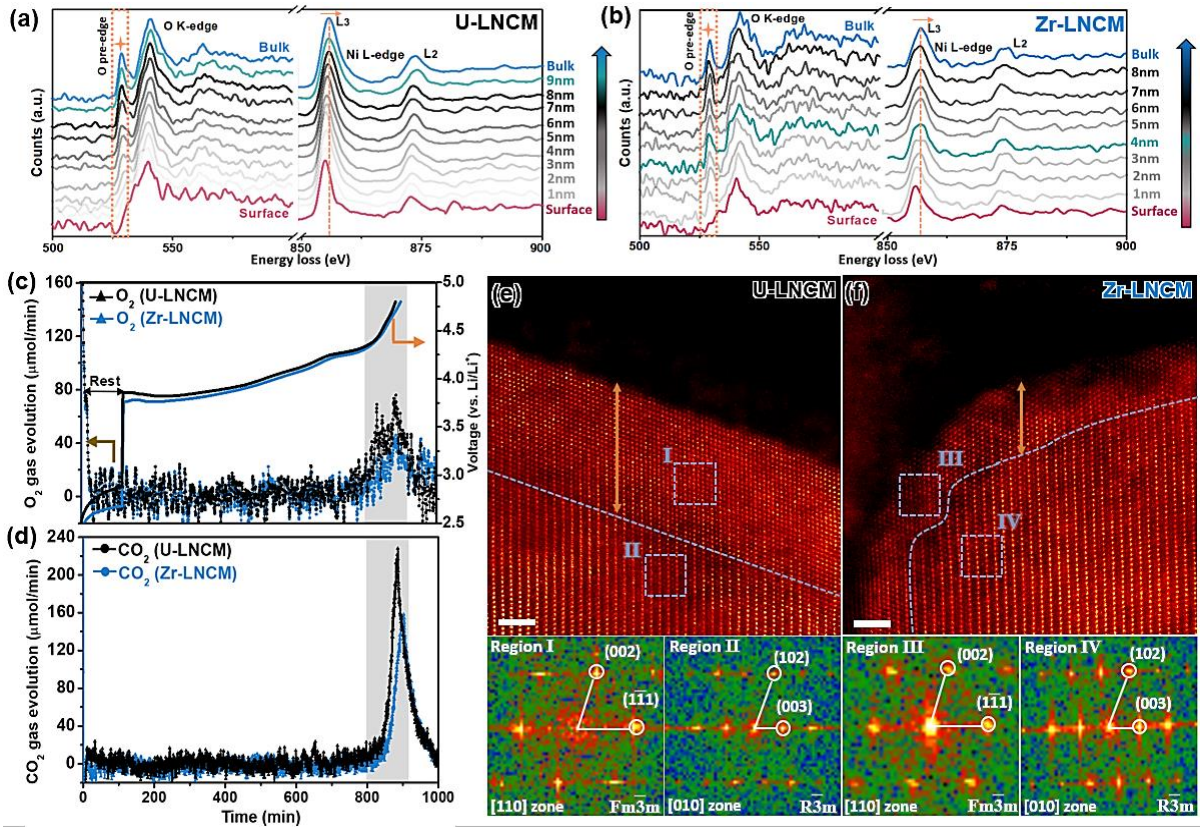

Figure 2.4. Line-scanning EELS spectra of O K-edge and Ni L-edge (as-labeled) for after cycled (a) U-LNCM and (b) Zr-LNCM. Differential electrochemical mass spectrometry (DEMS) spectra of (c) U-LNCM and (d) Zr-LNCM electrodes when charged to 4.8 V at 0.1 C current density. Atomic-resolution STEM images of after 50th cycled (e) U-LNCM and (f) Zr-LNCM. Scale bars are 2 nm.

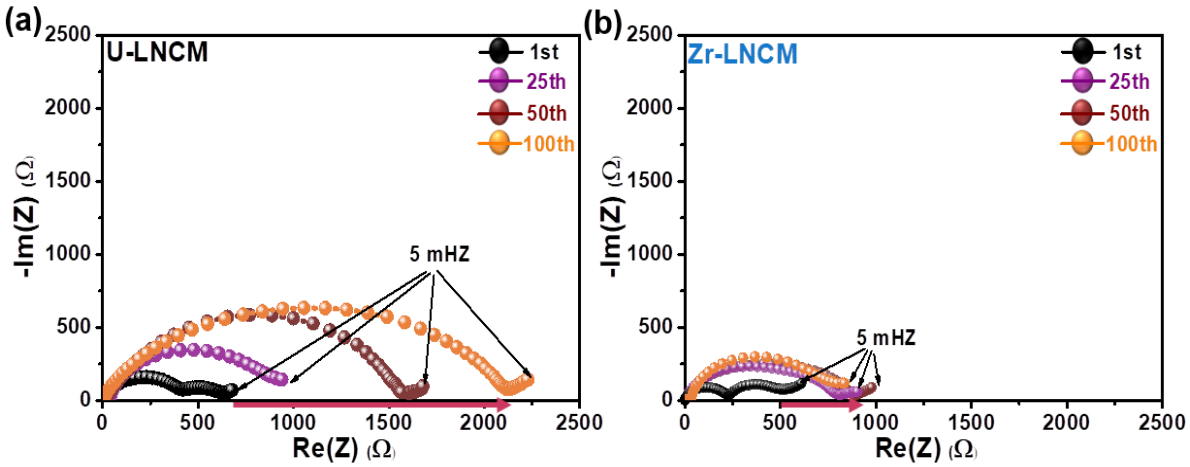

Figure 2.5. EIS measurements of the charged samples for (a) U-LNCM and (b) Zr-LNCM upon cycling from 1st to 100th

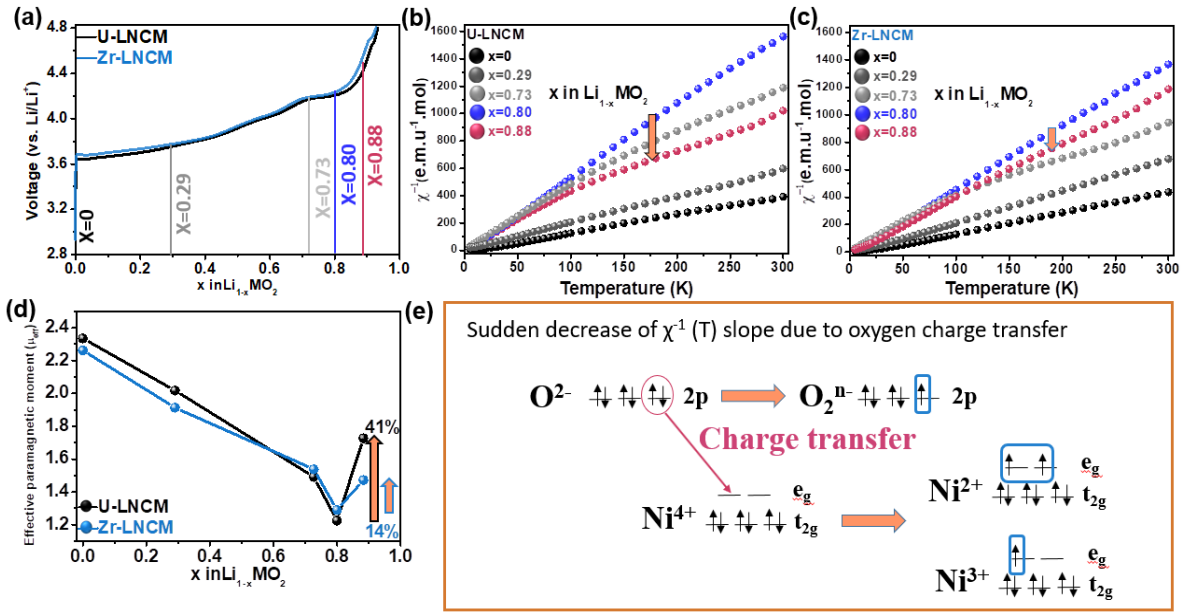

Figure 2.6. (a) Galvanostatic graphs of U-LNCM and Zr-LNCM with the points indicating the SOC states in which Squid-VSM analyses have been taken. Susceptibility versus temperature graph for the (b) U-LNCM and (c) Zr-LNCM samples. (d) Calculated effective paramagnetic moment of the samples depending on the SOC. (e) Schematic illustration of the sudden increase of magnetic moment upon high SOC.

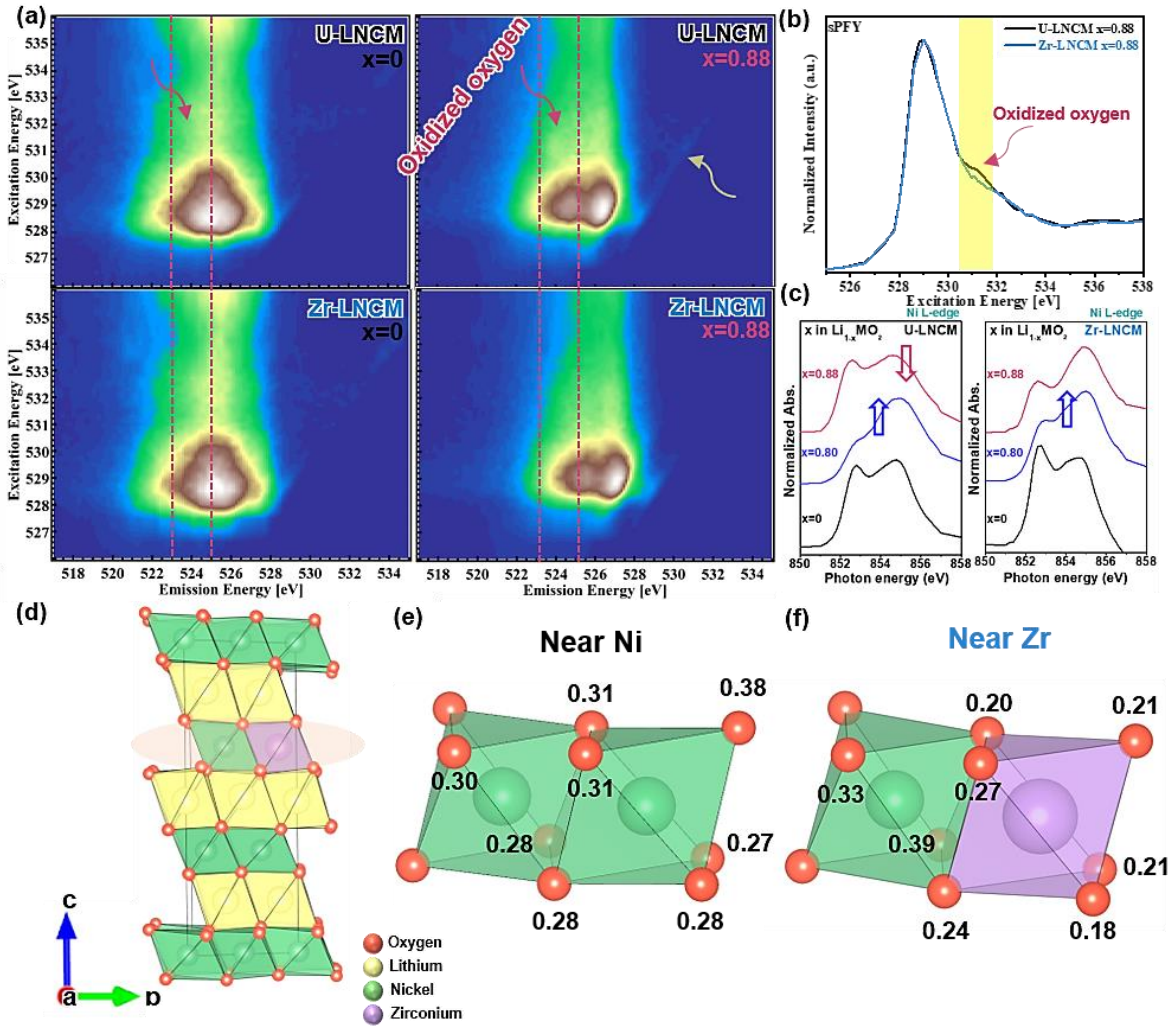

Figure 2.7. (a) O K-edge mRIXS analysis of U-LNCM and Zr-LNCM during first cycle delithiation (x, $Li_{1-x}MO_2$). (b) O-K mRIXS-sPFY analysis of U-LNCM and Zr-LNCM at x=0.88 state, where the peak on the shaded area around 530~532 eV indicates the oxidized oxygen. (c) Ni L-edge STXM results of U-LNCM and Zr-LNCM during first cycle delithiation (x, $Li_{1-x}MO_2$). (d) Atomic structure of $Li_{12}Ni_{11}ZrO_{24}$, (e) atomic structure near Ni atom, and (f) atomic structure near Zr atom. The number on (e) and (f) indicates the charge loss of corresponding oxygen when delithiated from $Li_{12}Ni_{11}ZrO_{24}$ to $Li_2Ni_{11}ZrO_{24}$, which is obtained by the Badar charge analysis.

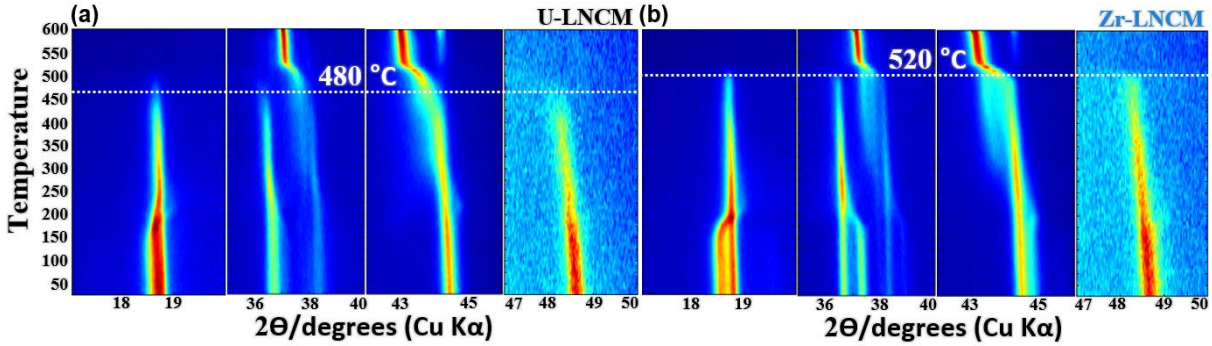

Figure 2.8. Temperature-resolved heating XRD patterns of 4.4 V charged (a) U-LNCM and (b) Zr-LNCM. The thermal decomposition temperature of the electrode is 480 and 520 °C for U-LNCM and Zr-LNCM, respectively.

2.1.5. Reference

[1] J. Wang, Y. Yamada, K. Sodeyama, C. H. Chiang, Y. Tateyama and A. Yamada, Nat. Commun. 2016, 7, 12032

[2] G. -L. Xu, X. Liu, A. Daali, R. Amine, Z. Chen, K Amine, Adv. Funct. Mater. 2020, 30, 2004748

[3] W. Li, E. M. Erickson, A. Manthiram, Nat. Energy. 2020, 5, 26-34

[4] C. -H. Jung, H. Shim, D. Eum, S. -H. Hong, J. Korean Ceram. Soc, 2021, 58, 1-27

[5] Y. Xia, J. Zheng, C. Wang, M. Gu, Nano Energy. 2018, 49, 434-452

[6] U. -H. Kim, G. -T. Park, B. -K. Son, G. W. Nam, J. Liu, L. -Y. Kuo, P. Kaghazchi, C. S. Yoon, Y. -K. Sun, Nat. Energy. 2020, 5, 860-869

[7] H. -H. Ryu, K. -J. Park, C. S. Yoon, Y. -K. Sun, Chem. Mater. 2018, 30, 1155-1163

[8] Q. Xie, W. Li, A. Manthiram, Chem. Mater. 2019, 31, 938-946

[9] U. H. Kim, D. W. Jun, K. J. Park, Q. Zhang, P. Kaghazchi, D. Aurbach, D. T. Major, G. Goobes, M. Dixit, N. Leifer, C. M. Wang, P. Yan, D. Ahn, K. H. Kim, C. S. Yoon, Y. K. Sun, Energy Environ. Sci. 2018, 11, 1271-1279

[10] S.-K. Jung, H. Gwon, J. Hong, K.-Y. Park, D.-H. Seo, H. Kim, J. Hyun, W. Yang, K. Kang, Adv. Energy Mater. 2014, 4, 1300787

[11] N. Li, S. Sallis, J. K. Papp, J. Wei, B. D. McCloskey, W. Yang, W. Tong, ACS Energy Lett. 2019, 12, 2836–2842

[12] R. Jung, M. Metzger, F. maglia, C. Stinner, H. A. Gasteiger, J. Phys. Chem. Lett. 2017, 8, 4820-4825

[13] S. Sharifi-Asl, J. Lu, K. Amine, R. Shahbazian-Yassar, Adv. Energy Mater. 2019, 9, 1900551

[14] L. Mu, R. Lin, Rong Xu, L. Han, S. Xia, D. Sokaras, J. D. Steiner, T. -C. Weng, D. Nordlund, M. M. Doeff, Y. Liu, K. Zhao, H. L. Xin, F. Lin, Nano Lett. 2018, 18, 3241-3249

[15] S. Lee, W. Jin, S. H. Kim, S. H. Joo, G. Nam, P. Oh, Y. -K. Kim, S. K. Kwak, J. Cho, Angew. Chem. Int. Ed. 2019, 58, 2-10

[16] W. Li, H. Y. Asl, Q. Xie, A. Manthiram, J. Am. Chem. Soc. 2019, 141, 5097-5101

[17] J. Wandt, A. T. S. Freiber, A. Ogrodnik, H. A. Gasteiger, Mater. Today. 2018, 21, 825-833

[18] M. D. Radin, S. Hy, M. Sina, C. Fang, H. Liu, J. Vinckeviciute, M. Zhang, M. S. Whittingham, Y. S. Meng, A. Van der Ven. Adv. Energy Mater. 2017, 7, 1602888

[19] D. -H. Seo, J. Lee, A. Urban, R. Malik, S. Kang, G. Ceder, Nat. Chem. 2016, 8, 692-697

[20] C. F. Petersburg, Z. Li, N. A. Chernova, M. S. Whittingham, F. M. Alamgir, J. Mater. Chem. A. 2012, 22, 19993-20000

[21] M. Yoon, Y. Dong, Y. Yoo, S. Myeong, J. Hwang, J. Kim, S. -H. Choi, J. Sung, S. J. Kang, J. Li, Jaephil Cho, Adv. Funct. Mater. 2019, 30, 1907903

[22] S. Sharifi-Asl, F. A. Soto, T. Foroozan, M. Asadi, Y. Yuan, R. Deivanayagam, R. Rojaee, B. Song, X. Bi, K. Amine, J. Lu, A. Salehi-khojin, P. B. Balbuena, R. Shahbazian-Yassar, Adv. Funct. Mater. 2019, 29, 1901110

[23] K. Luo, M. R. Roberts, R. Hao, N. Guerrini, D. M. Pickup, Y. -S. Liu, K. Edstrom, J. Guo, A. V. Chadwick, L. C. Duda, P. G. Bruce, Nat. Chem. 2016, 8, 684-691

[24] Q. Xie, W. Li, A. Dolocan, A. Manthiram, Chem. Mater. 2019, 31, 8886-8897

[25] R. Jung, M. Metzger, F. Maglia, C. Stinner, H. A. Gasteiger, J. Electrochem. Soc. 2017, 164, A1361-A1377

[26] C. Sun, X. Liao, F. Xia, Y. Zhao, L. Zhang, S. Mu, S. Shi, Y. Li, H. Peng, G. V. Tendeloo, K. Zhao, J. Wu, ACS Nano. 2020, 14, 6181-6190

[27] Z. Zhu, D. Yu, Z. Shi, R. Gao, X. Xiao, I. Waluyo, M. Ge, Y. Dong, W. Xue, G. Xu, W. -

K. Lee, A. Hunt, J. Li, Energy Environ. Sci. 2020, 13, 1865-1878

[28] A. O. Kondrakov, H. Geßwein, K. Galdina, L. d. Biasi, V. Meded, E. O. Filatova, G. Schumacher, W. Wenzel, P. Hartmann, T. Brezesinski, J. Janek, J. Phys. Chem. C. 2017, 121, 24381-24388

[29] P. Yan, J. Zheng, T. Chen, L. Luo, Y. Jiang, K. Wang, M. Sui, J. -G. Zhang, S. Zhang, C. Wang, Nat. Commun. 2018, 9, 2437

[30] K. Zhou, Q. Xie, B. Li, A. Manthiram, Energy Storage Mater. 2021, 34, 229-240

[31] W. Liu, X. F. Li, D. B. Xiong, Y. C. Hao, J. W. Lia, H. R. Kou, B. Yan, D. J. Lia, S. G. Lu, A. Koo, K. Adair, X. L. Sun, Nano Energy. 2018, 44, 111–120

[32] X. Xu, H. Huo, J. Jian, L. Wang, H. Zhu, S. Xu, X. He, G. Yin, C. Du, X. Sun, Adv. Energy Mater. 2019, 9, 1803963

[33] U. H. Kim, H. H. Ryu, J. H. Kim, R. B. Mücke, P. Y. Kaghazchi, C. S. Yoon, and Y. K. Sun, Adv. Energy Mater. 2019, 9, 1803902

[34] T. Weigel, F. Schipper, E. M. Erickson, F. A. Susai, B. Markovsky, D. Aurbach, ACS Energy Lett. 2019, 4, 508-516

[35] H. -H. Ryu, G. -T. Park, C. S. Yoon, Y. -K. Sun, J. Mater. Chem. A. 2019, 7, 18580-18588

[36] Q. Li, Z. Li, S. Wu, Z. Wang, X. Liu, W. Li, N. Li, J. Wang, W. Zhuang, ACS Appl. Energy Mater. 2020, 3, 11741-11751

[37] J. H. Choi, S. Y. Lee, S. M. Yoon, K. H. Kim, M. Kim, S. H. Hong, ChemSusChem. 2019, 12, 2439-2446

[38] F. Schipper, M. Dixit, D. Kovacheva, M. Talianker, O. Haik, J. Grinblat, E. M. Erickson, C. Ghanty, D. T. Major, B. Markovsky, D. Aurbach, J. Mater. Chem. A. 2016, 4, 16073-16084

[39] F. Schipper, H. Bouzaglo, M. Dixit, E. M. Erickson, T. Weigel, M. Talianker, J. Grinblat, L. Burstein, M. Schmidt, J. Lampert, C. Erk, B. Markovsky, D. T. Major, D. Aurbach, Adv.

Energy Mater. 2018, 8, 1701682

[40] C. S. Yoon, U. -H. Kim, G. -T. Park, S. J. Kim, K. -H. Kim, J. Kim, Y. -K. Sun, ACS Energy Lett. 2018, 3, 1634-1639

[41] Y. Kim, Phys. Chem. Chem. Phys. 2019, 21, 12505-12517

[42] J. -H. Kim, H. -H. Ryu, S. J. Kim, C. S. Yoon, Y. -K. Sun, ACS Appl. Mater. Interfaces. 2019, 11, 30936-30942

[43] A. Manthiram, B. Song, W. Li, Energy Storage Mater. 2017, 6, 125-139

[44] H. Li, P. Zhou, F. Liu, H. Li, F. Cheng, J. Chen, Chem. Sci. 2019, 10, 1374-1379

[45] H. -H. Ryu, N. -Y. Park, J. H. Seo, Y. -S. Yu, M. Sharma, R. Mucke, P. Kaghazchi, C. S. Yoon, Y. -K. Sun, Mater. Today. 2020, 36, 73-82

[46] S. Xia, L. Mu, Z. Xu, J. Wang, C. Wei, L. Liu, P. Pianetta, K. Zhao, X. Yu, F. Lin, Y. Liu, Nano Energy. 2018, 53, 753-762

[47] P. Yan, J. Zheng, Z. -K. Tang, A. Devaraj, G. Chen, K. Amin, J. -G. Zhang, L. -M. Liu, C. Wang, Nat. Nanotech. 2019, 14, 602-608

[48] K. Jarvis, C. -C. Wang, M. Varela, R. R. Unocic, A. Manthiram, P. J. Ferreira, Chem. Mater. 2017, 29, 7668-7674

[49] S. Sharifi-As, F. A. Soto, A. Nie, Y. Yuan, H. Asayesh-Ardakani, T. Foroozan, V. Yurkiv, B. Song, F. Mashayek, R. F. Klie, K. Amine, J. Lu, P. B. Balbuena, R. Shahbazian-Yassar, Nano Lett. 2017, 17, 2165-2171

[50] D. Qian, B. Xu, M. Chi, Y. S. Meng, Phys. Chem. Chem. Phys. 2014, 16, 14665-14668

[51] F. Kong, C. Liang, L. Wang, Y. Zheng, S. Perananthan, R. C. Longo, J. P. Ferraris, M. Kim, K. Cho, Adv. Energy Mater. 2019, 9, 1802586

[52] Y. R. Song, F. Yang, M. -Y. Yao, F. Zhu, L. Miao, J. -P. Xu, M. -X. Wang, H. Li, X. Yao, F. Ji, S. Qiao, Z. Sun, G. B. Zhang, B. Gao, C. Liu, D. Qian, C. L. Gao, J. -F. Jia, Appl. Phys.

Lett. 2012, 100, 242403

[53] G. Klinser, M. Stuckler, H. Kren, S. Koller, W. Goessler, H. Krenn, R. Wurschum, J. Power Sources. 2018, 396, 791-795

[54] J. Sugiyama, Y. Ikedo, K. Mukai, H. Nozaki, M. Månsson, O. Ofer, M. Harada, K. Kamazawa, Y. Miyake, J. H. Brewer, E. J. Ansaldo, K. H. Chow, I. Watanabe, T. Ohzuku , Phys. Rev. B. 2010, 82, 224412

[55] S. Topolovec, H. Kren, G. Klinser, S. Koller, H. Krenn, R. Wurschum, J Solid State Electrochem. 2016, 20, 1491-1496

[56] M. Freire, N. V. Kosova, C. Jordy, D. Chateigner, O. l. Lebedev, A. Maignan, V. Pralong, Nat. Mater. 2016, 15, 173-177

[57] N. A. Chernova, M. Ma, J. Xiao, M. S. Whittingham, J. Breger, C. P. Grey, Chem. Mater. 2007, 19, 4682-4693

[58] M. Labrini, F. Scheiba, A. Almaggoussi, M. Larzek, M. H. Braga, H. Ehrenberg, I. Saadoune, Solid State Ionics. 2016, 289, 207-213

[59] C. F. Petersburg, Z. Li, N. A. Chernova, M. S. Whittingham, F. M. Alamgir, J. Mater. Chem. 2012, 22, 19993-20000

[60] W. Yang, T. P. Devereaux, J. Power Sources. 2018, 389, 188-197

[61] G. -H. Lee, J. Wu, D. Kim, K. Cho, M. Cho, W. Yang, Y. -M. Kang, Angew. Chem. Int. Ed. 2020, 59, 8681-8688

[62] N. Li, S. Sallis, J. K. Papp, J. Wei, B. D. McCloskey, W. Yang, W. Tong, ACS Energy Lett. 2019, 4, 2836-2842

[63] J. Wu, Z. Zhuo, X. Rong, K. Dai, Z. Lebens-Higgins, S. Sallis, F. Pan, L. F. J. Piper, G. Liu, Y. -d. Chuang, Z. Hussain, Q. Li, R. Zeng, Z. -X. Shen, W. Yang, Sci. Adv. 2020, 6, eaaw3871

[64] K. Dai, J. Wu, Z. Zhuo, Q. Li, S. Sallis, J. Mao, G. Ai, C. Sun, Z. Li, W. E. Gent, W. C. Chueh, Y. -D. Chuang, R. Zeng, Z. -X. Shen, F. Pan, S. Yan, L. F. J. Piper, Z. Hussain, G. Liu, W. Yang, Joule. 2019, 3, 518-541

[65] D. Eum, B, Kim, S, J, Kim, H, Park, J, Wu, S.-P. Cho, G. Yoon, M. H. Lee, S. -K. Jung, W. Yang, W. M. Seong, K. Ku, O. Tamwattana, S. K. Park, I. Hwang, K. Kang, Nat. Mater. 2020, 19, 419-427

[66] J. -N. Zhang, Q. Li, C. Ouyang, X. Yu, M. Ge, X. Huang, E. Hu, C. Ma, S. Li, R. Xiao, W. Yang, Y. Chu, Y. Liu, H. Yu, X. -Q. Yang, X. Huang, L. Chen, H. Li, Nat. Energy. 2019, 4, 594-603

[67] J. Cheng, L. Mu, C. Wang, Z. Yang, H. L. Xin, F. Lin, K. A. Persson, J. Mater. Chem. 2020, 8, 23293-23303

[68] H. Yang, H. -H. Wu, M. Ge, L. Li, Y. Yuan, Q. Yao, J. Chen, L. Xia, J. Zheng, Z. Chen, J. Duan, K. Kisslinger, X. C. Zeng, W. -K. Lee, Q. Zhang, J. Lu, Adv. Funct. Mater. 2019, 29, 1808825

[69] K. -W. Nam, S.-M. Bak, E. Hu, X. Yu, Y. Zhou, X. Wang, L. Wu, Y. Zhu, K.-Y. Chung, X.-Q. Yang, Adv. Funct. Mater. 2013, 23, 1047-1063

[70] J. Hong, H. -D. Lim, M. Lee, S. -W. Kim, H. Kim, S. -T. Oh, G. -C. Chung, K. Kang, Chem. Mater. 2012, 24, 2692-2697

[71] G. Kresse, J. Furthmuller, Phys. Rev. B. 1996, 54, 11169

[72] G. Kresse, D. Joubert, Phys. Rev. B. 1999, 59, 1758

[73] V. I. Anisimov, J. Zaanen, O. K. Andersen, Phys. Rev. B. 1991, 44, 943

[74] L. Wang, T. Maxisch, G. Ceder, Phys. Rev. B. 2006, 73, 195107

[75] A. Y. Toukmaji, J. A. Board, Comput. Phys. Commun. 1996, 95, 73-92

[76] S. P. Ong, W. D. Richards, A. Jain, G. Hautier, M. Kocher, S. Cholia, D. Gunter, V. L.

Chevrier, K. A. Persson, G. Ceder, Comput. Mater. Sci. 2013, 68, 314-319

Chapter 3.

Extrinsic design of Ni-rich layered cathode for Lithium ion batteries

3.1. Kinetically Stabilizing the Mother Texture Inherited Ni-rich Layered Oxide via Doping Strategy

3.1.1. Introduction

Microstructure control and design have been widely applied in the material synthesis for catalyst, electronics, optics, and energy storage applications due to the size and/or shape dependent properties [1-4]. Furthermore, tuning the materials to certain geometric configuration have been shown to exhibit high reversibility by accommodating the extreme environmental changes [5]. In this respect, its methodology has successfully have paved the way to the introduction of new anode materials for lithium-ion batteries (LIBs), while the horizon is expanding toward the cathode materials to reconcile the issues they have encountered [6-9].

Layered ternary oxides such as $LiNi_xCo_yMn_{1-x-y}O_2$ (LNCM) or $LiNi_xCo_yAl_{1-x-y}O_2$ (LNCA) have gained much attention as promising cathode materials to improve the energy density and lower the battery cost [10]. Both industrial and academic focus is to increase the Ni-content in layered oxide cathode materials in order to further increase their practical capacity [11]. Unfortunately, the multiple degradation mechanisms that operates during battery cycling induce the fast capacity decay and safety concern, which in turn impede their successful application [12]. Among the degradation factors, mechanical crack is considered as one of the most threatening issue that obstructs the Ni-rich layered cathode practical implantation [13-15]. Mechanical degradation is provoked by the sudden c-axis contraction upon deep charge, which

builds up the localized strain that is eventually released through the particle disintegration [16,17]. These cracks provide the electrolyte infiltration pathway and provoke the unwanted parasitic reactions between freshly exposed surface and electrolyte, resulting in the rapid impedance rise. Thus, regulating the mechanical crack is considered as an essential prerequisite for the future design of Ni-rich layered cathode materials.

While intrinsic lattice change and consequent mechanical strain are unavoidable during electrochemical cycling, the structural integrity of Ni-rich layered cathode can be preserved through a rational microstructure design [19,20]. In particular, the radially arranged plate-like primary particles with high crystalline texture allow the particles to shrink/expand evenly, thereby alleviate the internal stress accumulation and prevent the crack nucleation [21]. Furthermore, microstructure texturing of Ni-rich layered oxide can remarkably enhance the cathode kinetics by providing the 3D Li^+ ion channels from particle surface to inner bulk [19]. Such microstructure configuration has been previously adopted by boron/phosphorus doping [22,23], concentration gradient [24], and modified coprecipitation methods [25,26]. Especially, the microstructure control through doping is gaining much attention as this approach can modify the Ni-rich layered oxide structure in a simple manner. The origin of Ni-rich layered oxide crystalline texture via B doping has been attributed to the surface energy modification through first-principle calculations, where a lattice inserted boron lowered the (003) surface energy compared to other planes and thereby producing the primary particles with (003) facet [21,27]. However, the previous reports have evidenced that when boron or phosphorus is introduced in the layered oxide, not only its elements are incorporated into the layered oxide lattice, but also partially exists on the particle surface as a form of amorphous layer or glass phase [28,29]. It is well established that the presence of amorphous layer or glass phase at the grain boundary modifies the microstructure of sintered body through grain growth suppression

or recrystallization mechanism [30-33]. This strongly suggests that the existence of such layer though B or P doping may have played significant role in the textured microstructure development of Ni-rich layered oxides. Moreover, when considering that there is a structural relationship between layered oxide product and hydroxide precursor [34,35], there is a further possibility that such texture configuration of Ni-rich layered oxide might have originated from the precursor morphology. Overall, besides the surface energy modification through dopant incorporation, it is speculated that the layer development during doping process or precursor morphology could have critically contributed to the Ni-rich layered oxide textured microstructure.

In this work, microstructure evolution was comparatively investigated during the synthesis of undoped, B-doped, and P-doped $LiNi_{0.92}Co_{0.04}Mn_{0.04}O_2$ (LNCM) layered oxides starting from the $Ni_{0.92}Co_{0.04}Mn_{0.04}(OH)_2$ (NCM) hydroxide precursor, particularly focusing on the texture (primary particles aligned along the radial direction) development in B- and P-doped LNCMs (Scheme 3.1). In the synthesis of undoped LNCM, the plate-like NCM hydroxide was topotactically transformed to the LNCM oxide with retaining the layered framework, however upon further heating to reach optimum synthesis temperature, textured microstructure was transformed into randomly oriented polygonal primary particles by the occurrence of recrystallization process. On the other hand, when B/P were introduced into the layered oxide system, the plate-like morphology of primary particles was maintained up to the higher optimum synthesis temperature. Thus, the textured microstructure of B- and P-doped LNCMs was inherited from the NCM precursor morphology while addition of B/P served as a kinetic barrier during synthesis. Then, the role of B/P doping was systemically investigated by combining the state-of-the art atom probe tomography (APT) analysis with STEM and TOF-SIMS instruments. By the results, it was revealed that the amorphous layer was present on the

surface of primary particles in B- and P-doped LNCMs, and through the experimental design, it was found that such layer acted as a kinetic barrier that delayed the recrystallization process. Finally, in addition to revealing the role of B/P addition on the LNCM microstructure texturing, we also present the consequence of recrystallization process on the layered oxide secondary/primary particles crystallographic orientation that can have a significant impact on battery performance. This finding will shed light on the design of Ni-rich layered oxide with the desired morphology that can positively mitigate the structural damage during battery cycles.

3.1.2. Results

The optimum synthesis condition for undoped-$LiNi_{0.92}Co_{0.04}Mn_{0.04}O_2$ (U-LNCM) was determined by varying the calcination temperature from 600 to 840 ºC and selecting the temperature at which the U-LNCM exhibited the highest discharge capacity. All the investigated U-LNCMs exhibited the hexagonal α-$NaFeO_2$-type layer structure (space group: R-3m), and the U-LNCM electrode prepared with the powder calcined at 740 ºC showed the highest discharge capacity of ~230 mAh g^{-1} within the potential range of 2.5 ~ 4.4 V (vs. Li/Li^+) at a current density of 0.1 C (Figure 3.1.1). Thus, 740 ºC was chosen as an optimum synthesis temperature. The phosphorus-doped and boron-doped LNCMs (denoted as P-LNCM and B-LNCM, respectively) calcined at 740 ºC were the single phase LNCM layered oxides without an impurity phase (Figure 3.1.2), and their diffraction peaks slightly shifted to lower 2Θ values compared to those of U-LNCM indicating that both P and B were successfully incorporated into the LNCM lattice [22,23].

The scanning electron microscopy (SEM) images of NCM precursor and U-LNCM, P-LNCM, and B-LNCM calcined at 740 ºC are shown in Figure 1. The NCM precursor powder was more

or less spherical with an average diameter of ~10 μm, and the high magnification and cross-sectional SEM images revealed that each secondary particle was composed of numerous radially aligned plate-like primary particles (Figure 3.1.3a). After calcination (lithiation), the morphology of secondary particles was conserved, but the microstructure of primary particles was noticeably distinguished between the undoped and P/B doped. The U-LNCM primary particles were slightly elongated polygonal shaped particles, which were randomly oriented (Figure 3.1.3b), but P-LNCM (Figure 3.1.3c) and B-LNCM (Figure 3.1.3d) displayed the plate-like morphology of primary particles, which were radially aligned toward the surface of the secondary particles. The plate-like morphology of NCM precursor and doped-LNCMs was similar, but the thickness of plates significantly increased in doped-LNCMs. It is well known that the NCM hydroxide is topotactically transformed to LNCM oxide with preserving the layered framework of hydroxide precursor during the solid-state synthesis [36]. Consequently, the morphological resemblance between NCM precursor and doped LNCMs was resulted from the topotactic transformation process, and the radial orientation of plate-like primary particles in P-LNCM and B-LNCM was inherited from the NCM hydroxide morphology. However, the distinct morphology of U-LNCM implies that the topotactically transformed U-LNCM oxide has undergone another microstructural change (recrystallization) during the synthesis.

To confirm the topotactic transformation from NCM precursor to doped-LNCMs, the crystallographic orientation was examined by scanning transmission electron microscopy (STEM) analysis with using cross-sectional specimens prepared by focused ion beam (FIB). The cross-sectioned specimens of the NCM and doped-LNCMs displayed similar rod-like morphology (Figure 3.1.4 a a, b, c). At high magnification, both NCM and doped-LNCMs revealed similar layered local structure with the a-axis of crystallographic orientation aligned toward outer direction (Figure 3.1.4 d, e, f). The selected area electron diffraction (SAED)

patterns indexed NCM and doped-LNCMs as P-3m1 and R-3m space group, respectively, with each basal plane indexed into (001) and (003) plane, respectively. Considering the high crystallographic correlation between the (001) plane P-3m1 and the (003) plane of R-3m, the STEM results confirmed that doped-LNCMs were topotactically transformed from NCM hydroxide for both bulk and local structure (Figure 3.1.4g).

To seek whether the microstructure resemblance between the doped product and the precursor was coincidental, we have synthesized LNCM powders by using other NCM precursors that have different morphology as well as the compositional ratio. To do so, we have selected $Ni_{0.6}Co_{0.2}Mn_{0.2}(OH)_2$ (NCM 622) and $Ni_{0.8}Co_{0.1}Mn_{0.1}(OH)_2$ (NCM 811) as starting precursor, which have different morphology when compared with $Ni_{0.92}Co_{0.04}Mn_{0.04}(OH)_2$ (NCM 9244) precursor. As shown in Figure 3.1.5, the synthesized P- and B-LNCM powders also resembled NCM precursor morphology for both LNCM 622 (Figure 3.1.5a) and LNCM 811 (Figure 3.1.5b) case, while only U-LNCM showed distinct morphology. Thus, we have confirmed that P- and B-LNCM morphology originated from the NCM precursor morphology, while the radially aligned texture microstructure of P- and B-LNCM (9244) was enabled by NCM 9244 precursor morphology.

Afterwards, systematic investigations have been conducted to unveil the two phenomena we have observed; (1) origin of U-LNCM distinct morphology compared to P-LNCM, B-LNCM, and NCM precursor, (2) the role of phosphorous or boron doping on the morphology similarity between doped LNCMs and NCM precursor. To prove, *ex-situ* SEM analysis have been conducted to view the morphology evolution upon NCM→LNCM synthesis by varying the synthesis time or temperature. Further analysis from now on was performed by using NCM 9244 precursor.

Firstly, we controlled the synthesis time from 0 minutes to 12 hours while fixing the annealing

temperature to 740 °C (Figure 3.1.6). In case of U-LNCM-0 min-[740 °C], two different shape of primary particles were combined, that is, plate-alike primary particles and ellipse-alike primary particles. While plate-alike primary particles originated from the NCM precursor particles, newly formed ellipse-alike particles are indication of recrystallization during annealing process [34,35]. Therefore, the combination of two kinds of primary particles implies that U-LNCM-0 min-[740 °C] sample is under microstructure transformation process by the occurrence of recrystallization. When annealing time was increased from 0 min toward 12 h, the ellipse-alike nuclei grew into polygonal morphology and eventually showed randomly distributed primary particles for U-LNCM-12 h-[740 °C]. Therefore, the distinct microstructure of as-synthesized U-LNCM compared to NCM precursor was derived from the nucleation and growth process that occurred during thermal annealing. In contrast, both P-LNCM-0 min-[740 °C] and B-LNCM-0 min-[740 °C] showed same morphology with NCM precursor that was constituted of plate-alike primary particles. Its plate-alike form was maintained when increasing the annealing time from 0 min toward 12 h while only the thickness varied. Therefore, these results indicate that microstructure resemblance between the doped LNCMs and NCM precursor was attributed by the inhibition of recrystallization process during 740 °C annealing. Then, obtained powders were analyzed by XRD to investigate whether the U-LNCM microstructure transformation was related to the crystal structure evolution during thermal annealing (Figure 3.1.7). The crystal structure of U-LNCM-0 min-[740 °C] was indexed to $LiNiO_2$ oxide (SG: R-3m) while no NCM hydroxide peak (SG:P-3m1) was observed (Figure 3.1.7). Thus, NCM hydroxide have fully transformed into LNCM layered oxide even by annealing at 740 °C 0 minutes. With increasing the annealing time, the peaks grew quickly and became narrower, suggesting an increase of crystallinity [36]. With similarity, P-LNCM-0 min-[740 °C] and B-LNCM-0 min-[740 °C] also showed hexagonal layered structure while the

crystallinity increased with annealing time and thus, displaying a similar trend with U-LNCM XRD results (Figure 3.1.7b, c). Based on the XRD analysis, it appears that the microstructure transformation of U-LNCM or the morphology disparity between U-LNCM and doped LNCMs was not aroused by the crystal structure evolution during thermal annealing.

Then, morphology evolution was observed by controlling the annealing temperature from 600 ºC to 840 ºC while fixing the annealing time to 12 hours (Figure 3.1.8). The U-LNCM-600 ºC-[12 h] retained its original NCM hydroxide morphology (Figure 3.1.8). When the temperature was increased to 650 ºC, U-LNCM-650 ºC-[12 h] showed combination of plate-alike primary particles and ellipse-alike primary particles, which implies the occurrence of recrystallization process at fixed temperature. Newly formed nuclei grew with the annealing temperature and eventually displayed randomly distributed compact primary particles for U-LNCM-840 ºC-[12 h]. In case of P-LNCM and B-LNCM, only plate-alike primary particles were observed from 600 ºC to 740 ºC and no signs of recrystallization process was observed. These results are consistent with the time varied *ex-situ* SEM results in which P-LNCM and B-LNCM suppressed the recrystallization process and maintained NCM precursor morphology up to 740 ºC. However, when temperature reached 840 ºC, both the P-LNCM-840 ºC-[12 h] and B-LNCM-840 ºC-[12 h] showed same morphology with U-LNCM-840 ºC-[12 h], with constituting of massively grown polygonal primary particles. It is speculated that the recrystallization process eventually occurred for the P-LNCM and B-LNCM within the temperature range of 740 ºC ~840 ºC. Considering that recrystallization occurred at low temperature of ~650 ºC for U-LNCM, the above results indicate that P or B additive acted as a kinetic barrier on delaying the recrystallization onset temperature, and enabled the LNCM to maintain its NCM precursor morphology up to a higher temperature. To seek the relevance of microstructure transformation with crystal structure evolution, the obtained powders were

further analyzed by XRD. XRD profiles of the temperature varied powders showed similar tendency with the time varied XRD results, where 600 °C 12hour annealed U-LNCM & P-LNCM & B-LNCM powders were indexed to $LiNiO_2$ oxide (SG: R-3m) while the crystallinity increased with the temperature, therefore, further confirming the irrelevance of microstructure transformation with the phase evolution (Figure 3.1.9).

Finally, to unveil the phosphorous and boron origin acting as a kinetic barrier on delaying the recrystallization process, further STEM investigation had been conducted for B-LNCM and P-LNCM that have been annealed at 740 °C 12h (Figure 3.1.10). Surprisingly, the STEM images showed that B-LNCM (Figure 3.1.10a) and P-LNCM (Figure 3.1.10b) primary particles were uniformly covered with an amorphous layer that was not observable in U-LNCM primary particles. To analyze the composition of the amorphous layer, energy dispersive spectroscopy (EDS) mapping and electron energy loss spectroscopy (EELS) were conducted on P-LNCM. The investigation was not conducted on B-LNCM as the light-element boron is hardly detected by using above spectroscopies [37,38]. Firstly, uniform coverage of the primary particles with the phosphorous element can be viewed by P-LNCM EDS mapping, suggesting that the amorphous layer was composed of phosphorous element (Figure 3.1.10c). Furthermore, on the EELS spectrum, the P L-edge was detected from coating layer to particle bulk, while the Ni L-edge appeared only on the inner primary particle (Figure 3.1.10d). This indicates that phosphorous was doped into LNCM crystal structure and also, partially existed on the particle surface as an amorphous layer. Therefore, the above results demonstrated that presence of amorphous layer on the primary particles was due to the phosphorus and boron addition during annealing. We want to emphasize that these amorphous layers were only detected on the inner part the of the FIB specimen. Absent of such layer on the FIB outer part is expected to be the result of high-energy milling process that might have etched away the mechanically-weak

amorphous layer during FIB preparation. In the field of sintering academic, it is well known that passivation layer on the particle surface can delay the sintering onset temperature by suppressing the surface diffusion during thermal annealing [39-43]. This suggests that the surface layer act as kinetic barrier that can prevent atomic diffusion upon heating. Considering our results as well as previous studies, it is expected that the amorphous layer on P-LNCM and B-LNCM primary particles also acted as a kinetic barrier in our results, inhibiting the diffusion of substances and delaying the recrystallization onset temperature, thereby enabling the LNCM to maintain its NCM precursor morphology up to a higher temperature. To prove, we intentionally increased the thickness of the amorphous layer by increasing the phosphorous and boron additive concentration from 1 mole % to 5 mole %. The thickness of amorphous layer increased from ~10 nm to ~100 nm with the additive concentration (Figure 3.1.11), whereas the as-synthesized P-LNCM (5 mole %) and B-LNCM (5 mole %) showed highly similar microstructure to the NCM precursor compared to 1 mol% doped LNCMs (Figure 3.1.10e). This indicates that atom diffusion was more effectively inhibited with the increase of amorphous layer thickness, which consequently aided on showing the LNCM morphology closer to the NCM precursor. Thus, obtained results confirmed that formation of amorphous layer acted as a kinetic barrier role.

So far, systematic investigation has been conducted to elucidate the origin of radially aligned texture shape through P or B doping in Ni-rich LNCM. By diversifying the synthesis conditions, we showed that such microstructure was enabled by the delay of recrystallization through doping, while the origin was a formation amorphous layer on the particle surface that suppressed the surface diffusion during annealing. Furthermore, in order to acquire a such structure, we found that two variables have to be significantly considered: synthesis temperature and the morphology of the NCM precursor. These results may explain why the

textured microstructure via P or B doping was not observed in Ni-low LNCM as in previous reports. Firstly, it is well known that the optimum synthesis temperature of LNCM depends on the Ni content while higher temperature is required for the synthesis of Ni-low LNCM (reported optimum temperature for LNCM 811: ~800 ºC, LNCM 622: ~850 ºC, and LNCM 333: ~950 ºC) [44,45]. Thus, as recrystallization onset temperature can only be delayed to 740 ~ 840 ºC according to our results, recrystallization process will proceed during Ni-low LNCM synthesis regardless of P or B addition. Secondly, morphology of NCM precursor depends on transition metal ratio and especially, only the Ni-rich NCM hydroxide possess an urchin-like texture shape [46-48]. Therefore, even if the synthesis temperature is lowered to prevent the recrystallization and maintain the precursor morphology, the final product of P- and B- doped Ni-low LNCM cannot have radial aligned texture microstructure due to the precursor morphology.

3.1.3. Discussion

On our previous research, we have evidenced that crystallite orientation of as-synthesized U-LNCM (annealed condition: 740 ºC 12h) primary particles were randomly distributed, while P-LNCM and B-LNCM primary particles showed strong crystallographic texture with a-axis of the primary particles aligning toward outer direction [27]. This research demonstrated that such configuration of the doped LNCMs was the result of inheritance of NCM structure that possessed textured microstructure. In contrast, the random crystallographic orientation of U-LNCM primary particles is expected to be a result of the recrystallization process upon synthesis, however, yet unknown. Furthermore, to the best of our knowledge, the influence of recrystallization process on the crystallographic orientation of the layered oxide have not been

studied. Therefore, on the discussion, we focused on seeking the consequence of recrystallization on the U-LNCM secondary/primary particles crystallographic orientation. To do so, additional STEM studies were performed on the U-LNCM 650 ºC 12h sample to investigate the detailed structure of newly formed nuclei. Such powder, which contained the original plate-alike primary particles and newly formed ellipse-alike primary particles, were cross-sectioned by FIB and STEM analyzed (Figure 3.1.12a). Figure 3.1.11b and Figure 3.1.12c shows the original plate-alike and newly formed ellipse-alike particle, respectively. STEM image revealed that plate-alike particle has layered structure (SG: R-3m), with the a-axis of crystallographic orientation aligned toward outer direction (Figure 3.1.12d, h). As the plate-alike particle had undergone phase transformation (NCM→LNCM) while retaining their original NCM hydroxide morphology, the plate-shaped particles showed the same orientation as the NCM precursor, which is the similar result with the P-LNCM and B-LNCM STEM images (Figure 3.1.4). In contrast, the newly formed particles displayed clearly distinct orientation compared to plate-alike particle. While these particles also showed layered structure with same R-3m space group (Figure 3.1.12i, j), the a-axis of the particle orientation were not aligned toward the outer direction. Instead, a-axis of particle B and particle C were aligned horizontally (Figure 3.1.12e) and diagonally (Figure 3.1.12f), respectively, thus exhibiting completely random orientation. As these particles grow with annealing temperature (Figure 3.1.13), the nuclei with such a random orientation eventually will evolve into a polygonal morphology that maintains its random orientation behavior. Therefore, the above STEM results indicate that the random orientation of as-synthesized U-LNCM primary particles was the result of a recrystallization process that produced randomly distributed nuclei during annealing.

In addition, it was found that the recrystallization process not only causes random behavior between primary particles, but also affects the internal structure of the final product of primary

particles. To seek the consequence of recrystallization process on the internal structure of U-LNCM primary particle, ASTAR (automatic crystal orientation and phase mapping package for TEM) and STEM analysis have been measured and compared with P-LNCM and B-LNCM primary particle. 740 ºC 12hour annealed powders were selected for the analysis as U-LNCM have undergone recrystallization process in this condition while P- and B-LNCM have not. In order to acquire disorientation angles inside the primary particles, nanobeam electron diffraction (NBM) patterns were scanned and collected around 1.5 μm*1.5 μm area by using TEM equipped with ASTAR tool. Interestingly, relatively high degrees of disorientation angle revealed to exists within the U-LNCM primary particle (Figure 3.1.14a). Considering that the disorientation angle error by ASTAR measurement is within the range of ~1º [49,50], the relatively high angle misorientation exceeding ~6º suggests that U-LNCM primary particles are polycrystalline rather than a single crystal. Several particles were investigated for the reproducibility and revealed the comparable results. For P- and B-LNCM, only low angle disorientation below ~2 º was presented (Figure 3.1.14b, c), which is clearly different behavior with the U-LNCM and suggests the single crystal nature of P- and B-LNCM primary particles. To prove the disorientation results, we further examined the primary particles by STEM imaging. In local scale, all three powders possessed same crystal structure with showing (003) plane of rhombohedral layered oxide (SG: R-3m). However, in a wide view, U-LNCM (Figure 3.1.14d) showed grain boundary (GB) within the primary particle that was consisted of tilted grains arranged in different directions. In contrast, the P-LNCM (Figure 3.1.14e) and B-LNCM (Figure 3.1.14f) showed no evidence of GB within the primary particle. Thus, STEM results corresponded with the disorientation results and confirmed the polycrystal and single crystal nature of U-LNCM and doped LNCMs primary particles, respectively. Previously, the polycrystalline nature of the primary particles has been also demonstrated for the as-

synthesized LNCM 333 and LNCM 811 layered oxide [51]. While the phenomenon has been proposed as a result of orient attachment between the newly formed nuclei during LNCM synthesis, no clear evidence has been provided so far. Furthermore, in terms of cathode performance, in addition to microcracks between the primary particles, GB within the primary particle is also known to act as crack nucleation site during electrochemical cycles [52-54]. Therefore, this study evidenced that the polycrystalline nature of the primary particles is the result of recrystallization process during annealing and suggests that detrimental GBs within the primary particle can be avoided by delaying the recrystallization onset temperature through P or B doing.

3.1.4. Conclusions

Herein, systematic investigation has been conducted to reveal the origin of Ni-rich layered oxide texture microstructure through B or P doping. Firstly, we showed that the unique crystallographic texture of B/P doped layered oxide was inherited from the NCM hydroxide precursor morphology. To reveal its relationship, *ex-situ* SEM analysis has been conducted to observe the microstructure development upon NCM→LNCM synthesis and compared between the undoped, P-doped, and B-doped. In case U-LNCM, recrystallization process occurred around ~650 ℃, which transformed initial plate-alike NCM precursor morphology into a polygonal LNCM microstructure. While the phenomenon occurred regardless of P- and B-doping, the onset temperature of the recrystallization was delayed to 740~840 ℃ through doping and thus, enabling to maintain its NCM precursor microstructure up to a higher temperature. Finally, by adopting STEM analysis, we have revealed that its mechanistic role as a kinetic barrier was the formation of an amorphous layer on the particle surface that

suppressed the surface diffusion during annealing. This study will enhance our insight into the morphology design of electrode materials that can positively impact the battery performance.

3.1.5. Experimental procedure

Materials preparation

$Ni_{0.92}Co_{0.04}Mn_{0.04}(OH)_2$ hydroxide (NCM) was synthesized by using a co-precipitation method with $NiSO_4 \cdot 6\,H_2O$ (Daejung Chemical Co.), $CoSO_4 \cdot 7\,H_2O$ (Daejung Chemical Co.), $MnSO_4 \cdot H_2O$ (Daejung Chemical Co.), NaOH (Daejung Chemical Co.), and NH_4OH (Daejung Chemical Co.) as a chemical source. The details for the hydroxide preparation are provided elsewhere. To synthesize the undoped LNCM (U-LNCM), the obtained NCM precursor were mixed with $LiOH \cdot H_2O$ (precursor: Li=1:1.03 molar ratio) and calcined with oxygen gas flow. For the synthesis of P doped LNCM (P-LNCM) and B doped LNCM (B-LNCM), the NCM precursor was mixed with $LiOH \cdot H_2O$ and 1 mole % of $NH_4H_2PO_4$ (Sigma-Aldrich) or 1 mole % of B_2O_3 (Sigma-Aldrich) as phosphorus and boron source, respectively and annealed with oxygen gas flow. The annealing temperature or time were varied from 600 ºC~840 ºC or 0 h~12h, respectively. Before the analysis, the as-synthesized powders were sonicated in dehydrated ETOH to remove the unreacted residual lithium.

Characterization

The phase evolution was investigated by X-ray diffraction (XRD, Rigaku, D-MAX2500-PC) with Cu Kα radiation. The SEM (SU-70, Hitachi) and TEM (JEM-2100F, JEOL) were used to observe the particle morphology. The morphology was examined by field emission scanning electron microscopy (FESEM, Hitachi SU-70). The STEM images, energy dispersive spectroscopy (EDS), electron energy loss spectroscopy (EELS) analysis were obtained from

the double aberration-corrected JEOL-ARM 200CF microscope with a cold-field emission gun operated at an acceleration voltage of 200 kV. The cross-sectional SEM specimens were prepared by a cross-section polisher (IB-19510CP, JEOL), while the cross-sectional TEM specimens were prepared using FIB (Helios Nano Lab450, FEI). The disorientation angles were obtained with a JEM-2100F with a voltage of 200 kV equipped with an ASTAR (NanoMEGAS) device. The surface area and pore volume were characterized by nitrogen adsorption-desorption process at 77 K by using a BET (BELSORP-mini 11).

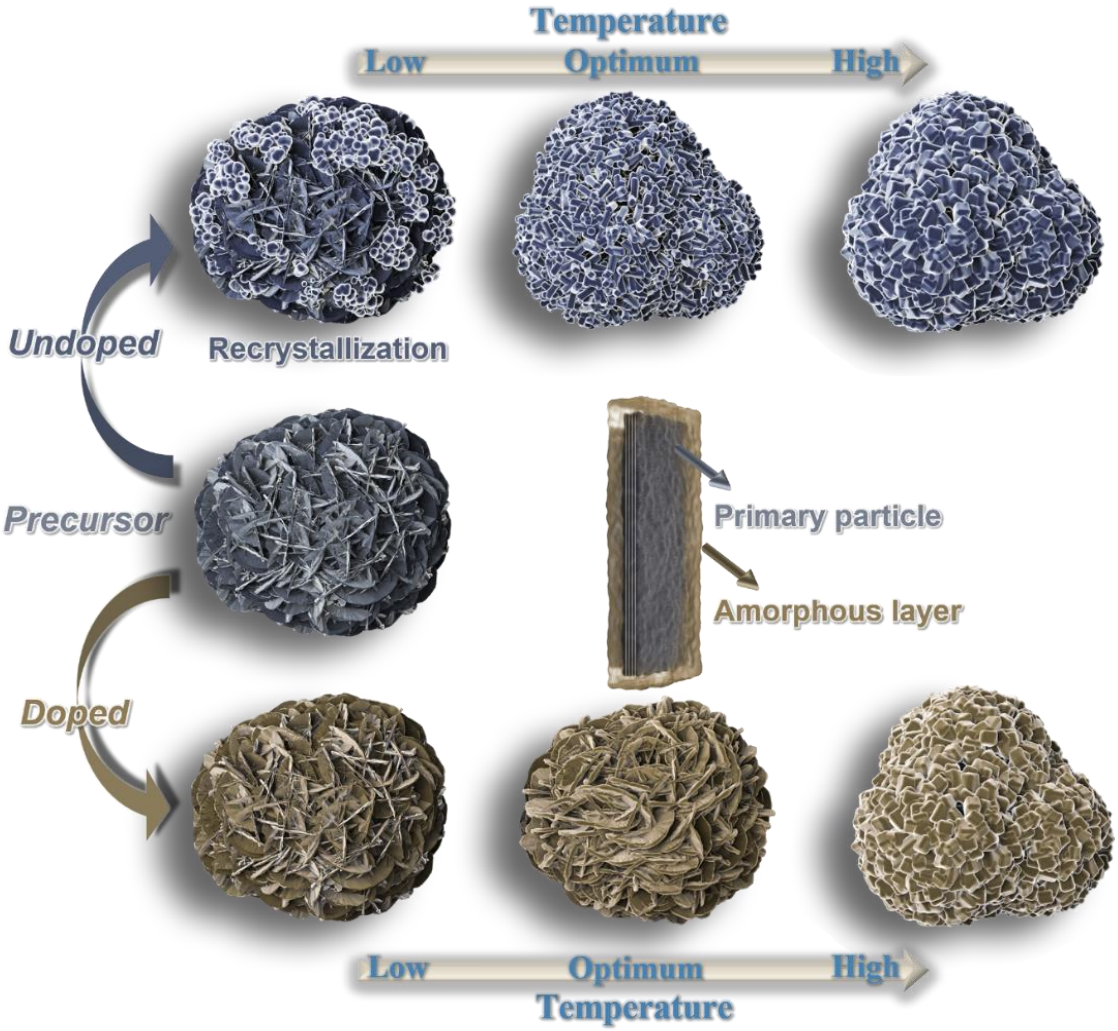

Scheme 3.1. Schematic illustration of comparing the microstructure evolution upon NCM hydroxide→ LNCM oxide synthesis between the undoped LNCM and doped-LNCMs.

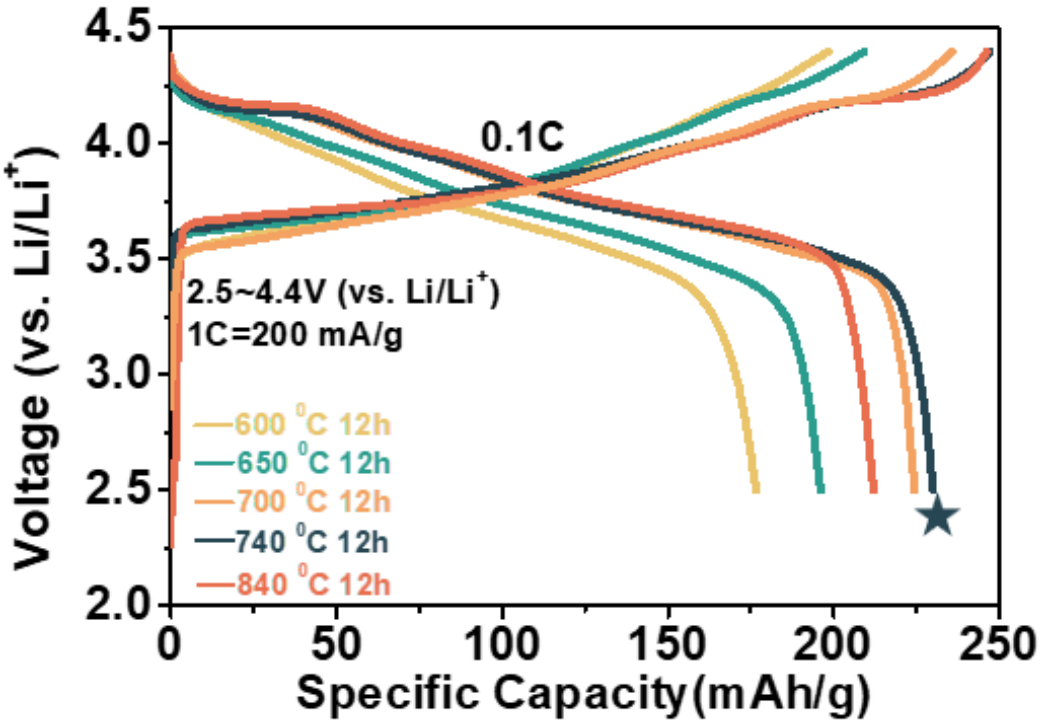

Figure 3.1.1. Galvanostatic graph of temperature varied as-synthesized U-LNCM. 740 ℃ 12h annealed showed the highest discharge capacity (~230 mAh/g) and thus, selected as optimum syntheis condition.

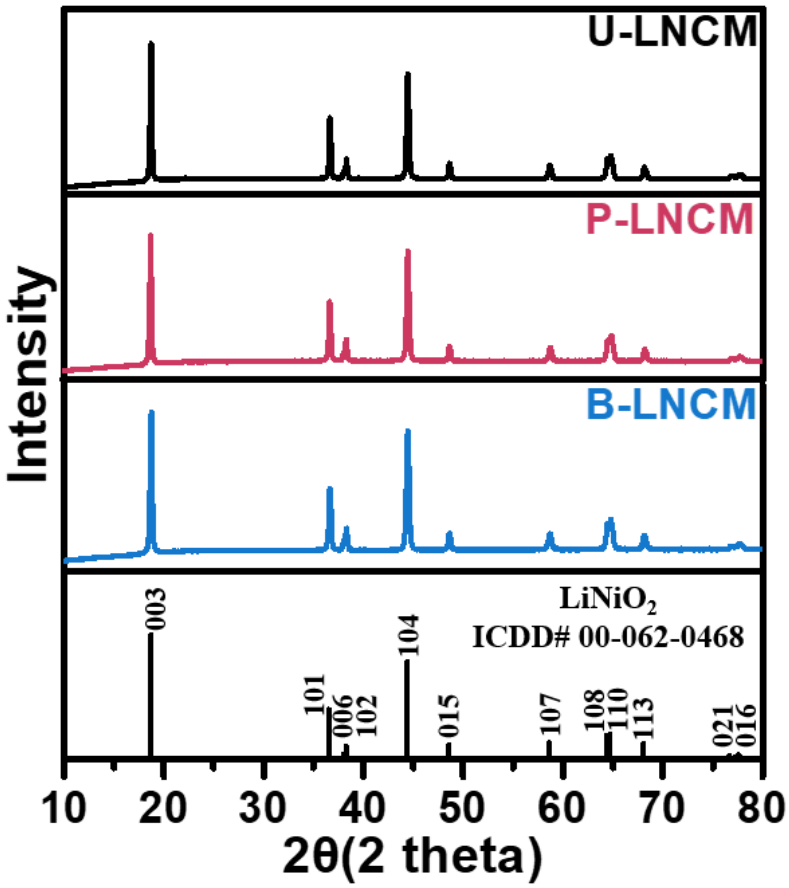

Figure 3.1.2. X-ray diffraction patterns of as-synthesized U-LNCM, P-LNCM, and B-LNCM powders, which was annealed at 740 ℃ 12h.

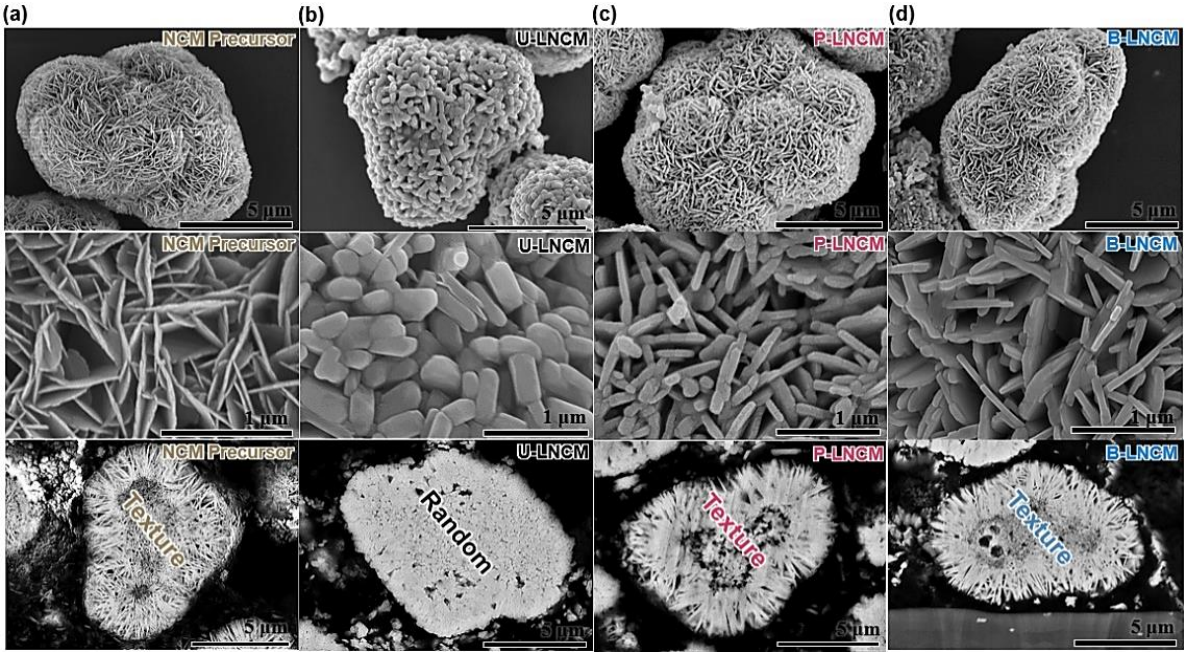

Figure 3.1.3. Low magnification, high magnification, and cross-sectioned polished SEM images of (a) NCM precursor, (b) U-LNCM, (c) P-LNCM, and (d) B-LNCM.

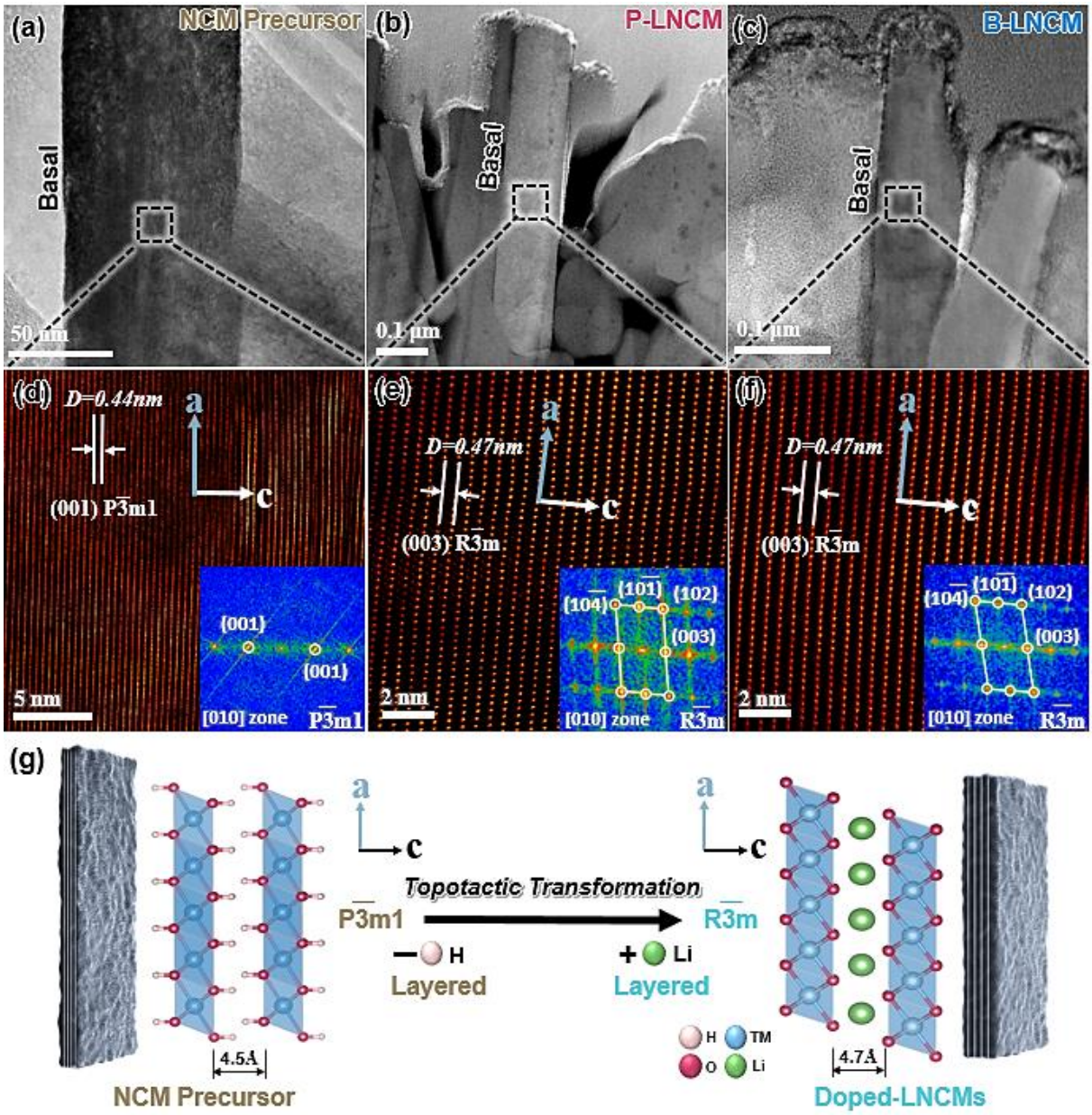

Figure 3.1.4. HRTEM image of (a) NCM precursor, (b) P-LNCM, and (c) B-LNCM. STEM image of (d) NCM precursor, (e) P-LNCM, and (f) B-LNCM. (g) Schematic illustration of topotactic transformation from the NCM hydroxide to doped-LNCMs.

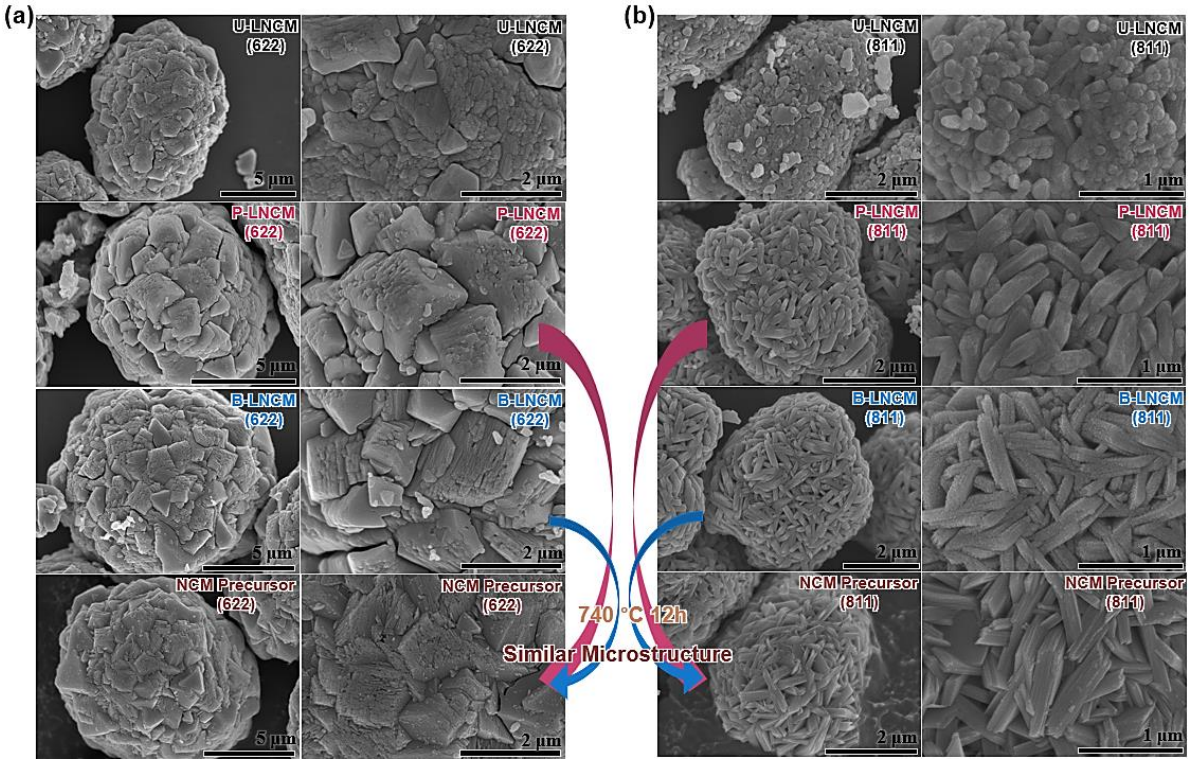

Figure 3.1.5. Microstructure comparison between the as-synthesized U-LNCM, P-LNCM, B-LNCM, and NCM precursor particles by using (a) NCM 622 precursor and (b) NCM 811 precursor.

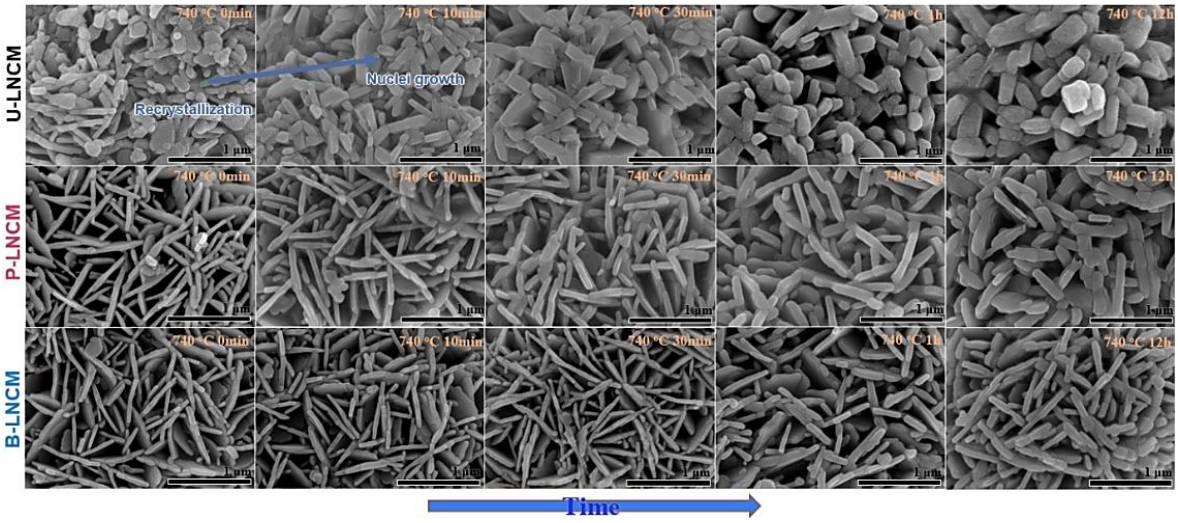

Figure 3.1.6. Synthesis time varied *ex-situ* SEM analysis of the as-synthesized powders. Synthesis time was varied from 0 minutes to 12 hours, while the annealing temperature was fixed to 740 ℃.

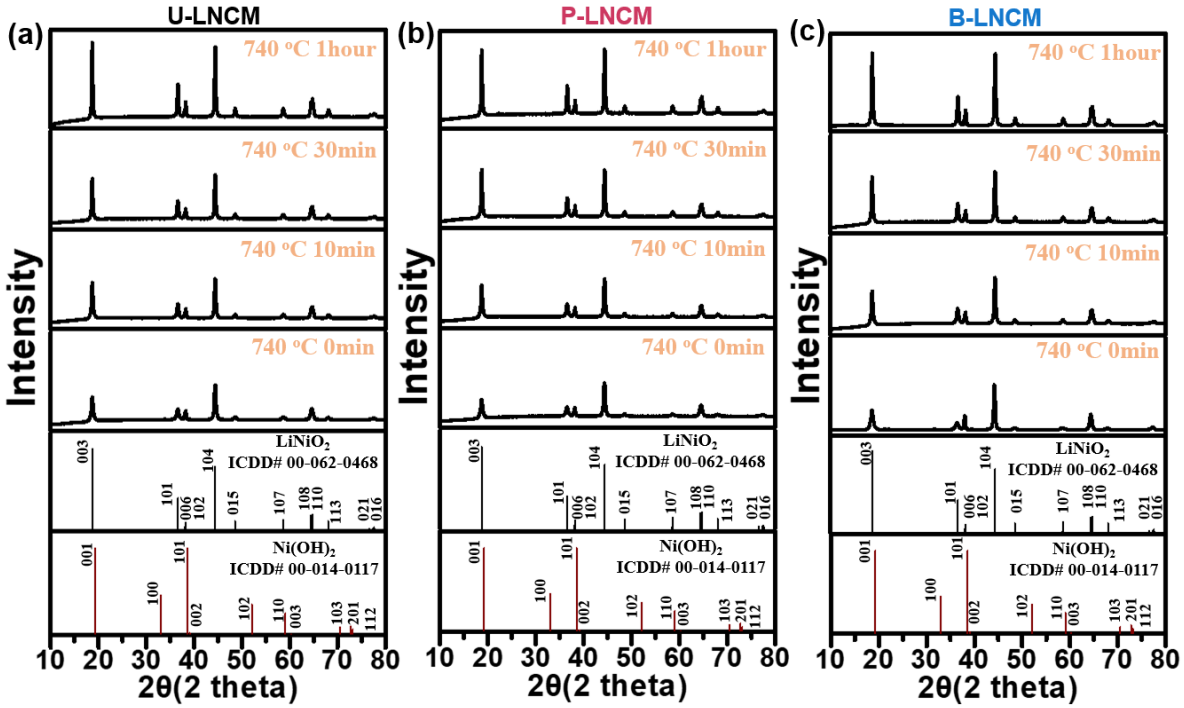

Figure 3.1.7. Synthesis time varied *ex-situ* XRD analysis of the as-synthesized (a) U-LNCM, (b) P-LNCM, and (c) B-LNCM powders. Synthesis time was varied from 0 minutes to 12 hours, while the annealing temperature was fixed to 740 ℃.

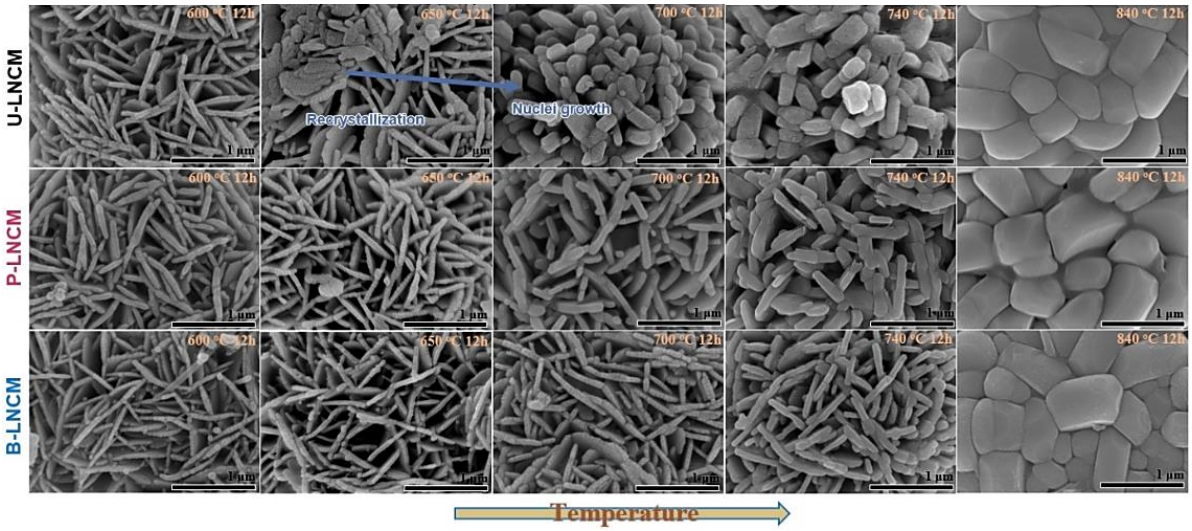

Figure 3.1.8. Synthesis temperature varied *ex-situ* SEM analysis of the as-synthesized powders. Synthesis temperature was varied from 600 ℃ to 840 ℃, while the annealing time was fixed to 12 hours.

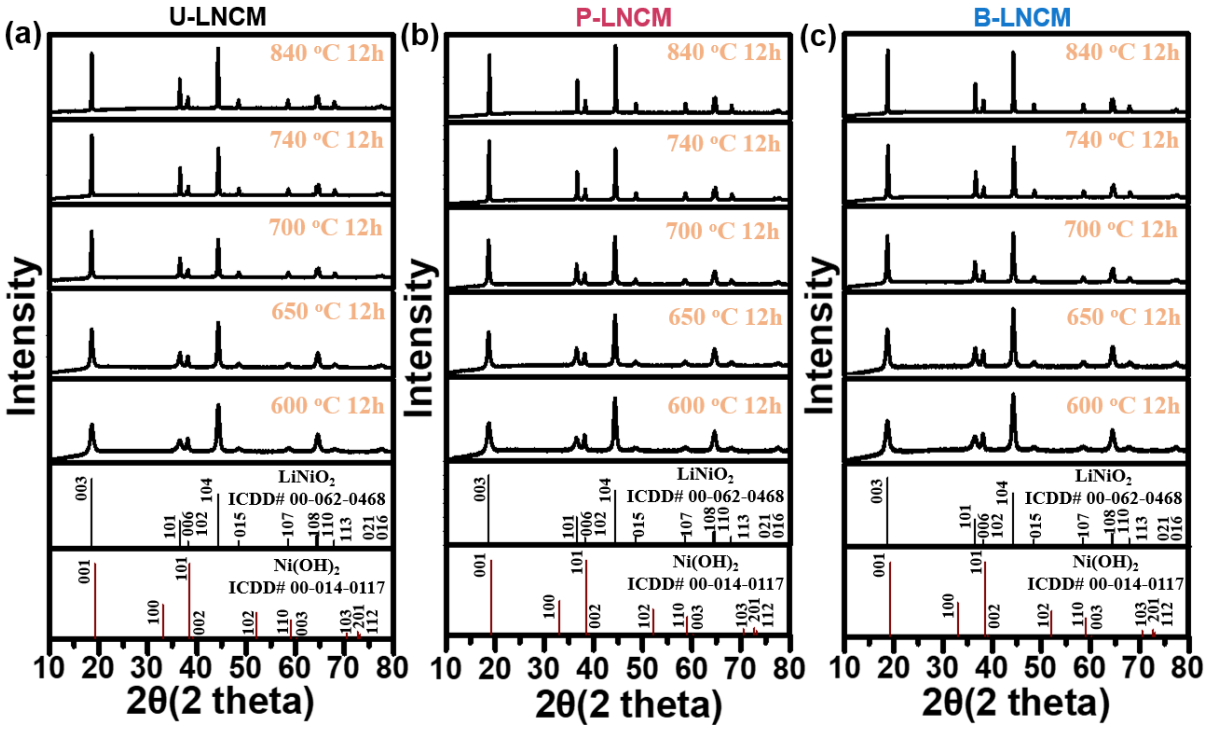

Figure 3.1.9. Synthesis temperature varied *ex-situ* XRD analysis of the as-synthesized (a) U-LNCM, (b) P-LNCM, and (c) B-LNCM powders. Synthesis temperature was varied from 600 ℃. To 840 ℃., while the annealing time was fixed to 12 hours.

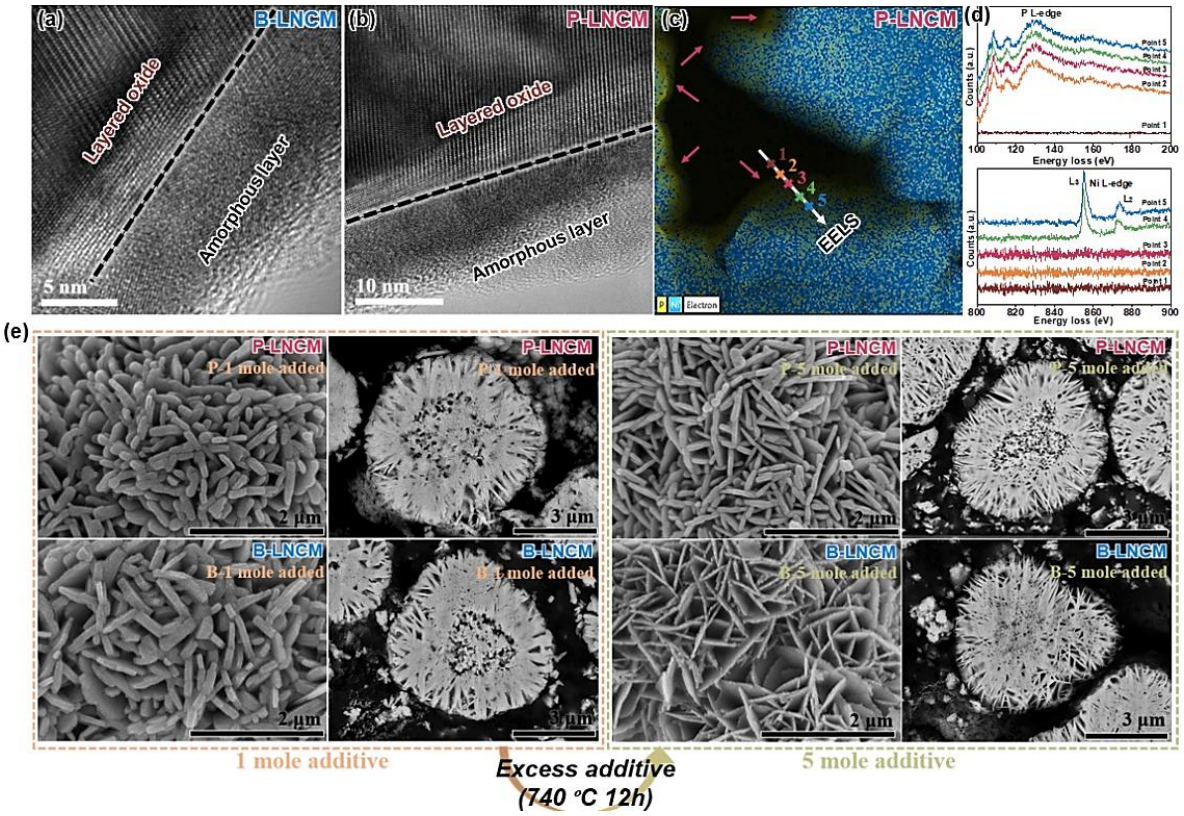

Figure 3.1.10. HRTEM image of FIB cross-sectioned (a) B-LNCM and (b) P-LNCM, which showed the amorphous layer covering the particle surface. (c) EDS mapping and (d) EELS analysis of P-LNCM. (e) Microstructure comparison between the 1 mole % doped P- and B-LNCM with the 5 mole % doped P- and B-LNCM.

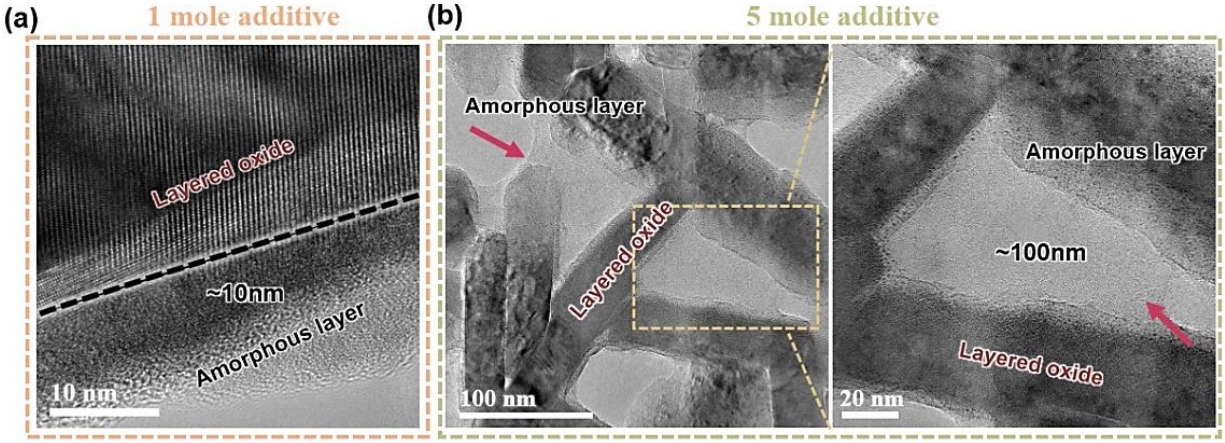

Figure 3.1.11. HRTEM image of FIB cross-sectioned (a) 1 mole % doped P-LNCM and (b) 5 mole % doped P-LNCM, which showed the increase of amorphous layer thickness upon doping amount.

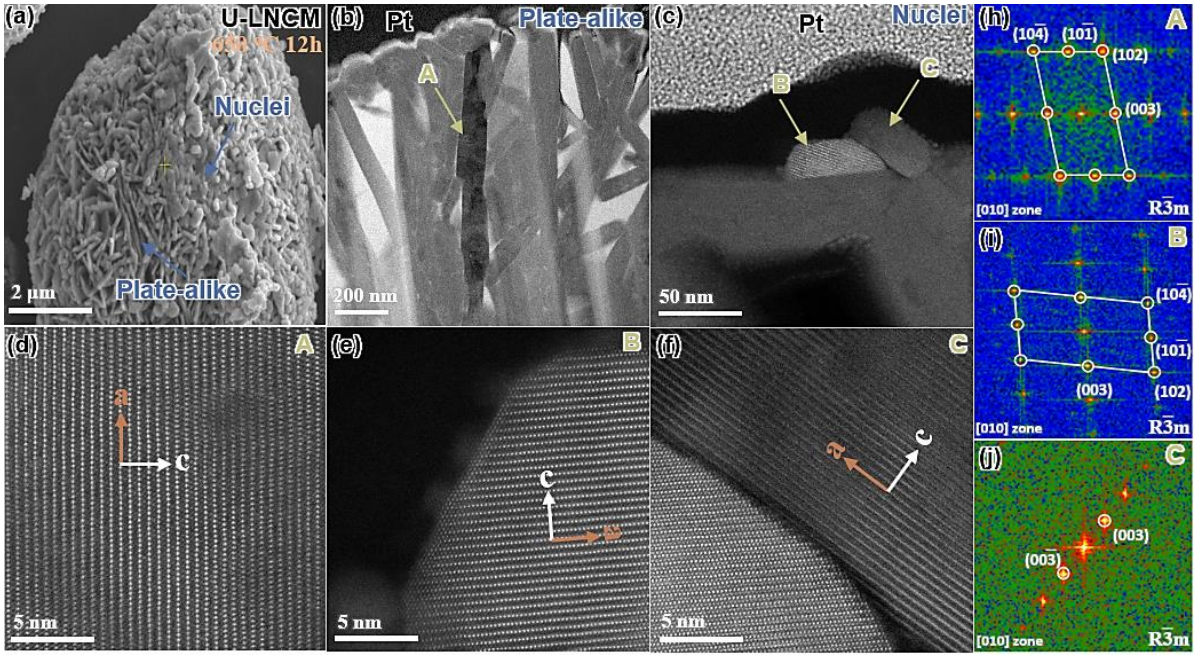

Figure 3.1.12. (a) SEM image of FIB cross-sectioned U-LNCM (650 ℃ 12h).HRTEM image of U-LNCM (650 ℃ 12h) with showing (b) original plate-alike particle [A] and (c) newly formed ellipse-alike particles [B,C]. STEM image of (d) particle A, (e) particle B, and (f) particle C. FFT image of (h) particle A, (i) particle B, and (j) particle C.

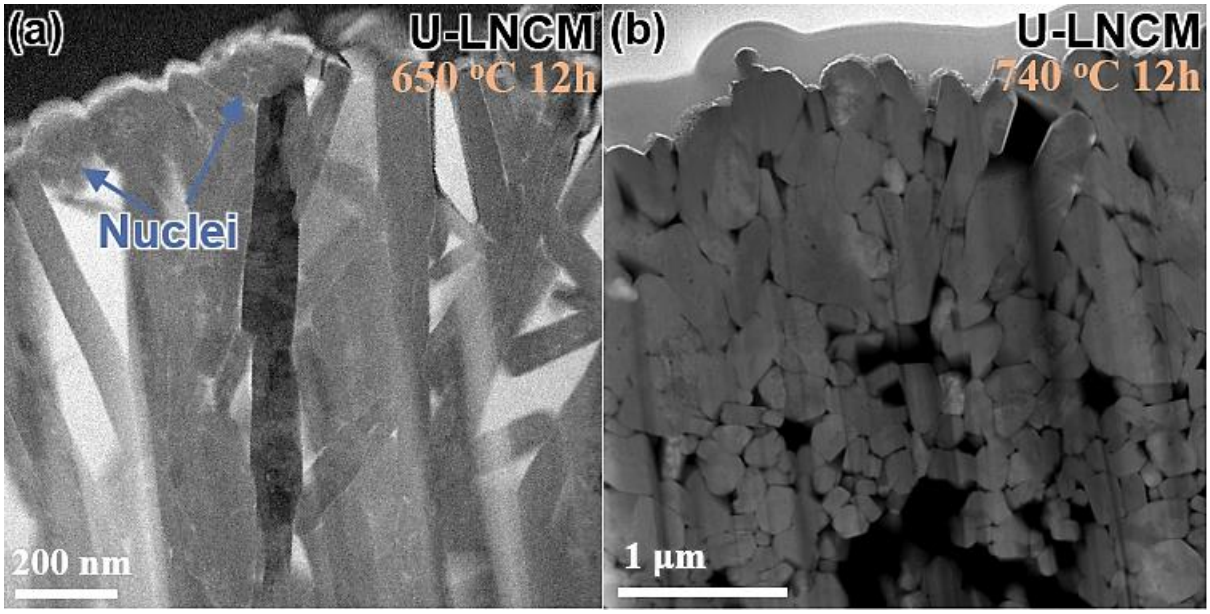

Figure 3.1.13. HRTEM image of FIB cross-sectioned U-LNCM annealed at (a) 650 ºC 12h and (b) 740 ºC 12h.

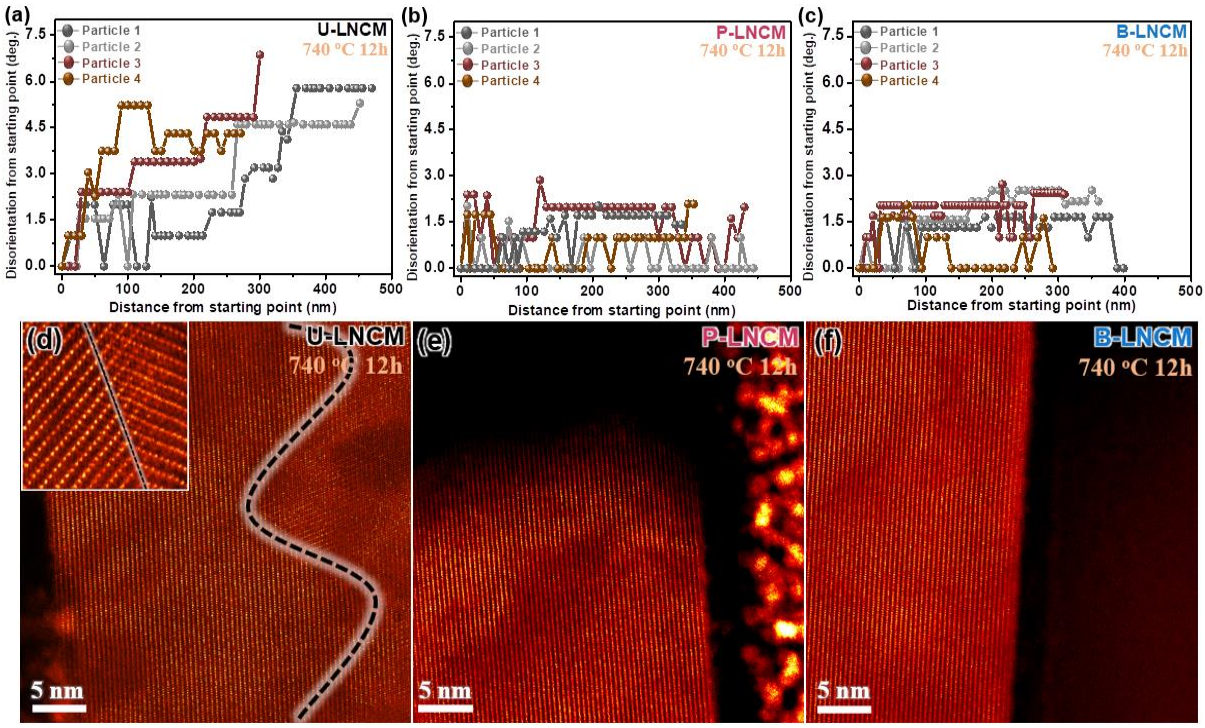

Figure 3.1.14. Disorientation angle within the inner primary particle for the 740 ℃ 12 h annealed (a) U-LNCM, (b) P-LNCM, and (c) B-LNCM, calculated from the scanned procession NBD data. Low magnification STEM image of 740 ℃ 12 h annealed (d) U-LNCM, (e) P-LNCM, and (f) B-LNCM.

3.1.6. Reference

[1] J. Joo, T. Kim, J. Lee, S. -l. Choi, K. Lee, Adv. Mater. 2020, 31, 1806682

[2] X. Huang, H. Yao, Y. Cui, W. Hao, Z. Zhu, W. Xu, D. Zhu, ACS Appl. Mater. Interfaces, 2017, 9, 40752-40759

[3] S. Misra, D. Zhang, Z. Qi, D. Li, J. Lu, H. -T. Chen, H. Wang, Cryst. Growth. Des, 2020, 20, 6101-6108

[4] K. Jiang, G. Zhang, G. Yang, J. Zhang, Z. Li, T. Ma, H. Hu, W. Ma, H. Ade, H. Yan, Adv. Energy Mater., 2018, 8, 1701370

[5] Y. Song, X. Chen, V. Dabade, T. W. Shield, R. D. James, Nature, 2013, 502, 85-88

[6] J. Choi, W. -S. Kim, K. -H. Kim, S. -H. Hong, J. Mater. Chem. A, 2018, 6, 17437-17443

[7] C. Jiang, L. Xiang, S. Miao, L. Shi, D. Xie, J. Yan, Z. Zheng, X. Zhang, Y. Tang, Adv. Mater. 2020, 32, 1908470

[8] L. Liang, W. Zhang, F. Zhao, D. K. Denis, F. U. Zaman, L. Hou, C. Yuan, Adv. Funct. Mater. 2020, 7, 1901749

[9] G. -L. Xu, X. Liu, A. Daali, R. Amine, Z. Chen, K. Amine, Adv. Funct. Mater. 2020, 30, 2004748

[10] C. -H. Jung, H. Shim, D. Eum, S. -H. Hong, J. Korean Ceram. Soc, 2021, 58, 1-27

[11] G. -L. Xu, X. Liu, A. Daali, R. Amine, Z. Chen, K Amine, Adv. Funct. Mater. 2020, 30, 2004748

[12] W. Li, E. M. Erickson, A. Manthiram, Nat. Energy. 2020, 5, 26-34

[13] D. -S. Ko, J. -H. Park, S. Park, Y. N. Ham, S. J. Ahn, J. -H. Park, H. N. Han, E. Lee, W. S. Jeon, C. Jung, Nano Energy. 2019, 56, 434-442

[14] J. -M. Lim, T. Hwang, D. Kim, M. -S. Park, K. Cho, M. Cho, Sci Rep. 217, 7, 39669

[15] Q. Lin, W. Guan, J. Zhou, J. Meng, W. Huang, T. Chen, Q. Gao, X. Wei, Y. Zeng, J. Li, Z. Zhang, Nano Energy. 2020, 76, 105021

[16] U. H. Kim, D. W. Jun, K. J. Park, Q. Zhang, P. Kaghazchi, D. Aurbach, D. T. Major, G. Goobes, M. Dixit, N. Leifer, C. M. Wang, P. Yan, D. Ahn, K. H. Kim, C. S. Yoon, Y. K. Sun, Energy Environ. Sci. 2018, 11, 1271-1279

[17] Q. Xie, W. Li, A. Manthiram, Chem. Mater. 2019, 31, 938-946

[18] S. Xia, L. Mu, Z. Xu, J. Wang, C. Wei, L. Liu, P. Pianetta, K. Zhao, X. Yu, F. Lin, Y. Liu, Nano Energy. 2018, 53, 753-762

[19] H. H. Sun, A. Dolocan, J. A. Weeks, A. Heller, C. B. Mullins, ACS Nano, 2020, 14, 17142-17150

[20] X. M. Fan, G. R. Hu, B. Zhang, X. Ou, J. F. Zhang, W. G. Zhao, ,H. P. Jia, L. F. Zou, P. Li, Y. Yang, Nano Energy. 2020, 70, 104450

[21] H. -H. Ryu, N. -Y. Park, J. H. Seo, Y. -S. Yu, M. Sharma, R. Mucke, P. Kaghazchi, C. S. Yoon, Y. -K. Sun, Mater. Today. 2020, 36, 73-82

[22] H. H. Ryu, N. -Y. Park, D. R. Yoon, U. -H. Kim, C. S. Yoon, Y. -K. Sun, Adv. Energy Mater. 2020, 10, 2000495

[23] C. -H. Jung, D. -H. Kim, D. Eum, K. -H. Kim, J. Choi, J. Lee, H. -H. Kim, K. Kang, S. -H. Hong, Adv. Funct. Mater. 2021, 2010095

[24] D. -W. Jun, C. S. Yoon, U. -H. Kim, Y. -K. Sun, Chem. Mater. 2017,29, 5048-5052

[25] X. Xu, H. Huo, J. Jian, L. Wang, H. Zhu, S. Xu, X. He, G. Yin, C. Du, X. Sun, Adv. Energy Mater. 2019, 9, 1803963

[26] B. Du, Y. Mo, H. Jin, X. Li, Y. Qu, D. Li, B. Cao, X. Jia, Y. Lu, Y. Chen, ACS Appl. Energy Mater. 2020, 3, 6657-6669

[27] K. -J. Park, H. -G. Jung, L. -Y. Kuo, P. Kaghazchi, C. S. Yoon, Y. -K. Sun, Adv. Energy

Mater. 2018, 8, 180102

[28] Q. Xie, W. Li, A. Dolocan, A. Manthiram, Chem. Mater. 2019, 31, 8886-8897

[29] A. Yuan, H. Tang, L. Liu, J. Ying, L. Tan, L. Tan, R. Sun, J. Alloys Compd. 2020, 844, 156210

[30] D. He, C. Gao, Ceram. Int. 2018, 44, 16246-16255

[31] X. Z. Ma, Z. L. Xiang, M. Z. Ma, C. Tan, Z. A. Yang, G. L. Shen, Z. Y. Chen, Q. Shu, Mater. Sci. Eng., A 2020, 772, 138749.

[32] M. S. Chuang, S. T. Lin, J. Mater. Eng. Perform. 2003, 12, 23-28

[33] F. S. Serafini, M. Peruzzo, I. Krindges, M. Felipe C. Ordonez, D. Rodrigues, R. M. Souza, M. Cristina M. Farias, Mater. Charact. 2019, 152, 253-264

[34] M. Jiang, Q. Zhang, X. Wu, Z. Chen, D. L. Danilov, R. Eichel, P. H. L. Notten, ACS Appl. Energy Mater. 2020, 3, 6583-6590

[35] C. S. Yoon, S. J. Kim, U. -H. Kim, K. -J. Park, H. -H. Ryu, H. -S. Kim, Y. -K. Sun, Adv. Funct. Mater. 2018, 28, 1802090

[36] M. -J. Zhang, G. Teng, Y. -c. K. Chen-Wiegart, Y. Duan, J. Y. P. Ko, J. Zheng, J. Thieme, E. Dooryhee, Z. Chen, J. Bai, K. Amine, F. Pan, F. Wang, J. Am.Chem. Soc. 2018, 40, 12484-12492

[37] R. F. Egerton, Ultramicroscopy. 2007, 107, 575-586

[38] V. Thomsen, D. Schatzlein, D. Mercuro, Spectroscopy. 2003, 18, 112-114

[39] J. -Y. Lee, J. -H. Lee, S. -H. Hong, Y. -K. Lee, J. -Y. Choi, Adv. Mater. 2003, 15, 1655-1658

[40] Y. Zhang, X. Wang, J. -Y. Kim, J. -R. Kim, K. -H. Hur, L. Li, J. Am. Ceram. Soc. 2013, 96, 2163-2166

[41] T. Yoneima, K. Fukushima, N. Saito, K. Nakashima, Mater. Trans. 2016, 57, 1374-1377

[42] M. J. Bermingham, S. D. McDonald, K. Nogita, D. H. St. John, M. S. Dargusch, Scr. Mater. 2008, 59, 538-541

[43] M. J. Bermingham, S. D. McDonald, D. H. St. John, M. S. Dargusch, J. Mater. Res. 2009, 24, 1529-1535

[44] H.-J. Noh, S. Youn, C. S. Yoon, Y.-K. Sun, J. Power Sources. 2013, 233, 121-130

[45] H. -H. Ryu, K. -J. Park, C. S. Yoon, Y. -K. Sun, Chem. Mater. 2018, 30, 1155-1163

[46] J. Yang, M. Hou, S. Haller, Y. Wang, C. Wang, Y. Xia, Electrochim. Acta. 2016, 189, 101-110

[47] Z. Xu, L. Xiao, F. Wang, K. Wu, L. Zhao, M. -R. Li, H. -L. Zhang, Q. Wu, J. Wang, J. Power. Sources. 2014, 248, 180-189

[48] Q. Su, Y. Li, L. Li, W. Li, G. Cao, L. Xue, J. Li, X. Cao, Mater. Lett. 2017, 198, 180-183

[49] E. F. Rauch, M. Veron, Mater. Charact. 2014, 98, 1-9

[50] A. Valery, E. F. Rauch, L. Clement, F. Lorut, J. Microsc. 2017, 268, 208-218

[51] S. -Y. Lee, G. -S. Park, C. Jung, D. -S. Ko, S. -Y. Park, H. G. Kim, S. -H. Hong, Y. Zhu, M. Kim, Adv. Sci. 2019, 6, 1800843

[52] P. Yan, J. Zheng, M. Gu, J. Xiao, J.-G. Zhang, C.-M. Wang, Nat. Commun. 2017, 8, 14101

[53] P. Yan, J. Zheng, T. Chen, L. Luo, Y. Jiang, K. Wang, M. Sui, J. -G. Zhang, S. Zhang, C. Wang, Nat. Commun. 2018, 9, 2437

[54] L. Mu, R. Lin, Rong Xu, L. Han, S. Xia, D. Sokaras, J. D. Steiner, T. -C. Weng, D. Nordlund, M. M. Doeff, Y. Liu, K. Zhao, H. L. Xin, F. Lin, Nano Lett. 2018, 18 3241-3249

3.2. New Insight into Microstructure Engineering of Ni-rich Layered Oxide Cathode for High Performance Lithium Ion Batteries

3.2.1. Introduction

Due to the rapid growth of large scale energy storage devices such as electric vehicles (EVs), the development of low-cost and high energy density lithium ion battery (LIB) electrode materials is highly demanding for the consumer needs [1]. The application of the state-of-the-art LIBs has been successfully achieved by paring graphite anode with layered transition metal oxide cathode where the lithium ions reversibly de-/intercalate through the interstitial sites of the electrodes [2,3]. In perspective of cathode materials, most widely used $LiCoO_2$ (LCO) layered oxide has faced the severe limitation due to its limited practical capacity (~140 mAh g^{-1}) and high price of cobalt (Co) [4]. To meet the automotive battery need (350 Wh/kg at US $75/kWh at cell level) [5], further extraction of lithium from the crystalline structure and substitution of high price Co with other elements are highly required. In this regard, three component layered $LiNi_xCo_yMn_{1-x-y}O_2$ (LNCM) has successfully substituted the LCO layered oxide over the years and solidified their status as the cathode material of choice for EV batteries [5,6]. Nowadays, the current trend is to push LNCM to higher Ni content, which can boost the practical capacity over 200 mAh g^{-1} attributed by the low voltage profile of Ni-rich cathodes [7,8].

Unfortunately, the viability of Ni-rich layered cathodes for the market is hindered by the

challenges from the deteriorations occurring in the length scale from nanometer to bulk. The performance degradations of LNCM are mainly attributed to surface reconstruction, singlet oxygen evolution (electrolyte decomposition), dissolution of transition metal (TM), and microcrack within the secondary particle [9,10]. Furthermore, above degradations become much severe with increasing the Ni content and among them, the particle crack and oxygen gas release have been considered as the main culprits for the cycle life failure of Ni-rich layered cathodes [11-13]. Upon the H2→H3 phase transition during charging, the lattice collapse along crystallographic *c*-axis direction leads to the particle crack, while the instability of H3 phase triggers the oxygen gas evolution [14,15].

Substantial efforts have been made to suppress the aforementioned issues and improve the cycle stability. The current strategies includes doping [16,17], lithium inactive/reactive coating [18,19], surface modification in primary particle level [20], compositional gradient cathodes [21], and morphology control [22,23]. Among them, the modulation of microstructure has received much attention as a suitable methodology to enhance the Ni-rich cathodes' performance. Especially, the textured microstructure, in which the primary particles are aligned along the radial direction, has been suggested to enhance the cathode cycle life by constraining the microcrack formation [22, 24-26]. However, as the failure of Ni-rich layered cathode is affected by the multiple deterioration factors, further improvement is expected by regulating the other degradation mechanisms besides the suppression of the microcrack formation. In this sense, oxygen gaseous release, which triggers the surface reconstruction and electrolyte decomposition [27-29], has to be also considered in order for the future design of the cathode material.

In this research, we show that both boron and phosphorous doping into Ni-rich LNCM produces the textured microstructure in a similar manner where the primary particles are

aligned along the radial direction. As far as we know, this is the first time to show the textured morphology by P doping. Attributed by their crystallographic texture, both B- and P-doped LNCMs successfully suppressed the particle cracks and enhanced the cycle life compared to the undoped LNCM, however, there existed the meaningful capacity retention difference between the doped cathodes. By conducting *in-situ/ex-situ* multi-length-scale X-ray spectroscopic analysis, microscopic imaging, and gas analysis, we show that the boron-doped Ni-rich layered oxide displays the better cycle performance not only by its ability to mitigate the microcrack formation during cycling but also by its primary particle morphology that was reluctant against the oxygen evolution. From the view point of cycle stability, the suppression of oxygen evolution attributed by its microstructure was as effective as its ability to mitigate the microcrack. Our work presents that, for the future design of the Ni-rich layered cathode materials, the suppression of microcrack formation as well as oxygen evolution has to be simultaneously considered.

3.2.2. Results and discussion

Figure 3.2.1a shows the high-resolution powder diffraction (HRPD) patterns of as-synthesized undoped, phosphorus-doped, and boron-doped $LiNi_{0.92}Co_{0.04}Mn_{0.04}O_2$ powders (denoted as U-LNCM, P-LNCM, and B-LNCM, respectively) obtained by synchrotron radiation X-ray beam. All the diffraction patterns were completely indexed based on the hexagonal α-$NaFeO_2$-type layer structure (space group R-3m) without an impurity phase. The clear splitting of (006)/(102) and (018)/(110) diffraction peaks implies a well ordered layer structure with a high crystallinity for all three powders (Figure 3.2.1b) [26]. With P and B doping, the diffraction peaks were shifted to lower 2θ values (Figure 3.2.1c) and the lattice

parameters determined by Rietveld refinement increased (Figure 3.2.1d), indicating that both P and B were successfully incorporated into the LNCM lattice. Previously, TM octahedral or Li tetrahedral site has been proposed as the possible B and P doping site [28,30-33]. The incorporation of P and B into the LNCM lattice was further corroborated by Fourier transformation infrared spectroscopy (FT-IR). In FT-IR spectra (Figure 3.2.2), the absorption band at 531 cm^{-1}, which is generally ascribed to TM-O-TM (TM=Ni, Co, and Mn) lattice vibration, was shifted to the lower wavenumber with P and B doping, while the new weak peaks at 1039 and 1045 cm^{-1}, corresponding to P-O and B-O vibrations, appeared in P-LNCM and B-LNCM powders, respectively [32]. The chemical compositions determined by inductively coupled plasma atomic emission spectroscopy (ICP-AES) indicated that the molar ratio of Mn: Co: Ni was close to the nominal composition (92: 4: 4) and the doping concentration of P and B was estimated to be approximately 1 mole%. Based on the characterization results, it can be inferred that phosphorus and boron were successfully incorporated into the LNCM crystal structure.

The morphology of as-synthesized U-LNCM, P-LNCM, and B-LNCM powders was observed by scanning electron microscopy (SEM) (Figure 3.2.3). All three powders are more or less spherical in shape with an average diameter of ~10 μm (Figure 3.2.3a, d, g). Each secondary particle was composed of smaller primary particles, but the morphology of primary particles was dramatically changed with P and B doping (Figure 3.2.3b, e, h). The U-LNCM powder was composed of slightly elongated polygonal primary particles that were randomly oriented, whereas P-LNCM and B-LNCM powders consisted of plate-like primary particles that were radially aligned. The B-LNCM powder had much thinner plate-like primary particles than the P-LNCM powder (74 vs. 144 nm). The textured morphology, that is, radial orientation of plate-like primary particles can be clearly observed in the cross-sectional polished SEM images

where the plates were extended from the surface to the near center of the secondary particles (Figure 3.2.3c, f, i).

To investigate the plate-like primary particles in P-LNCM and B-LNCM powders in detail, the cross-sectional specimens were prepared by focused ion beam (FIB) technique and observed by transmission electron microscopy (TEM). The FIB preparation details and the TEM observation direction are schematically illustrated on Figure 3.2.4. FIB specimen of plate-like primary particle should display rod-like morphology. The high magnification TEM images revealed that both primary particles exhibited the similar rod-like cross-sectional morphology as expected, but the primary particle of B-LNCM showed much thinner frontal facets (planes exposed to the surface (Figure 3.2.5a, c)). The atomic-resolution high angle annular dark filed (HAADF) scanning transmission electron microscopy (STEM) images and selected area electron diffraction (SAED) patterns indicated that both primary particles had the identical crystallographic orientation where the lateral plane was (003) and the frontal facets were (102) and (10-4) (Figure 3.2.5b, d). Consequently, the *a*-axes of the primary particles are directed to the surface of the secondary particle and the Li layers in each primary particle are aligned along the radial direction, which can facilitate the Li ion diffusion from surface to center and enhance the rate capability of LNCM cathode [35]. The textured microstructure of P-LNCM and B-LNCM powders was further confirmed by crystal orientation map obtained using ASTAR (automatic crystal orientation and phase mapping package for TEM). To obtain the crystallographic orientation maps (Figure 3.2.5e-g), each raw crystal orientation map was combined with its corresponding index map (This map is built based on the matching values between recorded diffraction pattern and most correlated diffraction pattern that is calculated from the crystal structural model) [36]. The color code for the crystal orientation map is shown in Figure 3.2.5i. The U-LNCM powder showed the randomly distributed color index, indicating

the randomly oriented primary particles (Figure 3.2.5e). On the contrary, the orientation maps of P-LNCM (Figure 3.2.5f) and B-LNCM (Figure 3.2.5g) are indexed as green tone, suggesting that most of the primary particles have the similar crystallographic orientation, that is, textured microstructure. The thinner and more elongated morphology of B-LNCM compared to P-LNCM can be further confirmed by ASTAR analysis. The development of radially aligned microstructure in boron-doped LNCM and LNCA cathodes has been attributed to the modification of surface energy through boron-doping, which was supported by the density functional theory (DFT) calculation [24,25]. However, it is well known that the addition of boron or phosphorus to the oxides forms the amorphous or glass phase at the grain boundary and modifies the microstructure during sintering through recrystallization or grain growth inhibition [37-41]. We highly speculate this possibility and further studies are ongoing to verify the detailed underlying mechanism of microstructure development in B-LNCM and P-LNCM powders.

The electrochemical properties of as-synthesized U-LNCM, P-LNCM, and B-LNCM powders as cathodes for LIBs were evaluated using a 2032 coin-type half-cell within a voltage range of 2.5~4.4 V (vs Li/Li^+) at a current density of 0.1 C (1 C= 200 mA g^{-1}) (Figure 3.2.6). All three electrodes exhibited the simialr initial charge/discharge voltage profiles, but the discharge capacity of P-LNCM (221.4 mAh g^{-1}) and B-LNCM (221.7 mAh g^{-1}) electrodes was slightly smaller than that of U-LNCM (228.5 mAh g^{-1}) due to the electrochemically inactive phosphorous and boron incorporation (Figure 4a). However, the cycle performance was significantly improved by P and B doping. After 100 cycles at the current density of 0.3 C, the U-LNCM electrode retained 64% of its initial discharge capacity whereas the P-LNCM and B-LNCM electrodes retained 72% and 78% of their initial discharge capacity, respectively (Figure 3.2.6b). Furthermore, the P-LNCM and B-LNCM electrodes exhibited much enhanced

rate capability compared to the U-LNCM electrode. At a high current density of 2 C, the P-LNCM and B-LNCM electrodes still delivered the high discharge capacity of 151.7 and 153.4 mAh g^{-1}, respectively, which was much higher than 105.7 mAh g^{-1} of the U-LNCM electrode (Figure 3.2.6c). To reveal the different cycling behavior of the three electrodes, the differential capacity (dQ dV^{-1}) profiles were obtained by differentiating the 5^{th}, 10^{th}, 15^{th}, and 30^{th} charge/discharge curves (Figure 3.2.6d-f). All three electrodes showed a series of phase transitions during charging from hexagonal to monoclinic (H1→M), monoclinic to hexagonal (M→H2), and hexagonal to hexagonal (H2→H3). The final H2→H3 phase transition is reported to be responsible for the abrupt anisotropic lattice contraction in the *c*-axis direction, which induces the mechanical stress on the particle that leads to the particle cracking and consequently, the capacity fading [8,10,11]. For the U-LNCM electrode, the intensity of H2→H3 peak rapidly decreased and the polarization voltage (potential gap between cathodic peak and anodic peak) significantly increased with cycles, implying the irreversible structural damage during cycling (Figure 3.2.6d). However, the irreversibility was reduced in the P-LNCM and B-LNCM electrodes (Figure 3.2.6e, f). In particular, the intensity and position of H2→H3 peak were relatively well maintained in the B-LNCM electrode, which was consistent with the improved cycle stability as described earlier. To see the consequence of different irreversible phase transition, the after cycled electrodes were examined by synchrotron X-ray beam. The HRPD patterns showed that all three cycled electrodes retained their original R-3m layer structure without a new phase formation (Figure 3.2.7). However, a careful observation revealed that the (003) diffraction peak was shifted to a lower 2θ in all three cycled electrodes. The peak shift is attributed to the different amount of remaining Li in the cycled electrodes, that is, Li deficiency. The Li deficiency of the cycled electrodes is due to the buildup of the electrode polarization that prevents the full-lithiation of the cathodes even at discharged state

[42]. The (003) peak shift was more significant in U-LNCM (0.05°) than P-LNCM (0.04°) and B-LNCM (0.02°) electrodes. Thus, the degree of peak shift in the HRPD patterns, extent of polarization in the dQ dV^{-1} plots, and capacity decay were in the same order (U-LNCM > P-LNCM > B-LNCM). The variation of lithium ion mobility (D_{Li}^{+}) and charge transfer resistance (R_{ct}) with cycles further supported the different cycling behavior of the three electrodes (Figure 3.2.8) [34,43]. D_{Li}^{+} and R_{ct} were determined by galvanostatic intermittent titration technique (GITT) and electrochemical impedance spectroscopy (EIS), respectively and the details are elsewhere [34,43,44]. The GITT measurement was carried out by applying the current pulse of 0.1 C for 20 min and subsequently resting for 1 h. D_{Li}^{+} continuously decreased with cycles in all three electrodes, but the reduction was more severe in U-LNCM, followed by P-LNCM and B-LNCM electrode (Figure 3.2.8a). R_{ct}, obtained by the semicircle in the Nyquist plot of EIS, increased with cycles in all three electrodes, but the rate of resistance increment was different and it was in the order of B-LNCM, P-LNCM, and U-LNCM (Figure 3.2.8b). Consequently, the degradation of lithium ion mobility and charge transfer resistance with cycles was consistent with the observed cycle stability of LNCM electrodes.

To find out the reasons for the improved cycling stability of the P-LNCM and B-LNCM electrodes, *in-situ* XRD analysis was performed to monitor the phase evolution and structural change during the delithiation. The electrodes were charged to 4.4 V (vs Li/Li^{+}) at a current density of 0.2 C using the modified coin-type cell with 3 mm hole at its center. Figure 3.2.9a represents the contour plot of (003) and (104) diffraction peaks for U-LNCM, P-LNCM, and B-LNCM electrodes. All three electrodes exhibited the continuous phase transitions upon charging, which were well matched with the previous reports [17]. Upon first charging, the $(003)_{H1}$ peak smoothly shifted to a lower 2θ and the $(003)_{H2}$ peak was evolved at ~4.1 V. The shift of (003) peak to a lower angle indicates the lattice expansion in *c*-axis direction, which is

attributed to the increase of oxygen-oxygen repulsion due to a Li removal within the Li-slab [45]. However, upon further charging, the (003) peak rapidly shifted toward higher 2θ for all three electrodes, which implies the abrupt decrease of inter-slab distance along *c*-axis direction. The peak shift during H2→H3 phase transition was 1.06, 1.04, and 1.03° for U-LNCM, P-LMCM, and B-LNCM, respectively and thus, the difference was not significant. This result suggests that the incorporation of phosphorous or boron on the crystal lattice did not noticeably mitigate the intrinsic structural change associated with the multiple phase transitions during charging. However, the beneficial effect of P and B doping can be clearly seen in the cross-sectional SEM images of the cycled electrodes (Figure 3.2.9b, c). In the 50^{th} cycled U-LNCM electrode, the numerous microcracks were formed throughout the secondary particle while some of the cracks crossed the entire particle, indicating that the randomly oriented primary particles in U-LNCM electrode could not relieve the internal stress and avoid the crack nucleation and propagation. It is expected that these microcracks provide a pathway for the electrolyte infiltration and deteriorate the newly exposed interior particles by forming the resistive surface, which results in the rapid capacity fading [46,47]. In contrast, no visible structural damage was found and the structural integrity was well preserved in the cycled P-LNCM and B-LNCM electrodes, showing that the radially aligned textured microstructure had the superior structural stability against the mechanical stress resulting from the anisotropic dimensional change during cycling [24,35]. Based on the obtained results, it can be concluded that the structural stability of textured microstructure is responsible for the enhanced cyclability of the P-LNCM and B-LNCM electrodes.

The P-LNCM and B-LNCM electrodes had the similar textured microstructure, which effectively suppressed the microcrack formation, but the B-LNCM electrode showed the comparatively better cycle performance than P-LNCM electrode (Figure 3.2.6b). Furthermore,

the degradation of lithium ion mobility and charge transfer resistance during the prolonged cycles was relatively mitigated in B-LNCM compared to P-LNCM electrode (Figure 3.2.8). These results indicate that the structural stability to restrain the particle cracking might not be the only reason for the improved cycle stability of doped electrodes. Thus, further investigation was performed by employing EELS, STEM imaging, DEMS, and sXAS analysis, focusing on elucidating the underlying mechanisms behind the cyclability difference between P-LNCM and B-LNCM electrodes.

First, electron energy loss spectroscopy (EELS) analysis was performed to understand the electronic states of the cycled electrodes (50 cycles at 0.3 C) at discharge state (Figure 3.2.10). In EELS spectra, O K-edge arises from exciting an O_{1s} shell electron to unoccupied hybridized TM_{3d}-O_{2p} orbitals, and TM L-edge measures the dipole allowed transitions from TM_{2p} orbitals to unoccupied TM_{3d}-O_{2p} orbitals [48-51]. While TM L-edge has been successfully utilized as an indicator for the oxidation states of TM ions in the layered cathodes, there are debates on using the O K pre-edge as an evidence of oxygen redox or oxygen vacancy [48,52]. This is because the TM-O hybridization decisively contributes to the O K pre-edge intensity. Furthermore, it has been proposed that the line-shape evolution of O K pre-edge is mainly determined by TM 3d state variation [53]. Nonetheless, as the O K pre-edge evolution always occurs with the TM L-edge variation and the oxygen vacancy accompanies with the TM reduction to maintain the charge balance, we can indirectly probe the oxygen vacancy formation through TM L-edge and O K pre-edge [50,54]. To probe the change of electronic states depending on the particle position, the EELS spectra were acquired by a line scanning from surface to bulk (10 nm from particle edge). Among TM L-edges, only Ni L-edge was investigated as Ni constitutes over 92% in LNCM and acts as a main culprit for the degradation of Ni-rich LNCM. All Ni L-edge spectra showed two characteristic peaks or white lines (L_3

and L_2), and the position of L_3-edge peak gradually shifted to a lower energy when moved from bulk to surface. The Ni L-edge peak recovered the bulk peak at 8 and 4 nm for frontal and lateral facets of U-LNCM (Figure 3.2.10b, c) and 6 and 3 nm for frontal and lateral facets of both P-LNCM (Figure 3.2.10e, f) and B-LNCM (Figure 3.2.10h, i), respectively. As the shift of L_3-edge peak to the lower energy implies the reduction of valence state [48,49], the above results indicate that Ni ions at the surface are reduced with an anisotropic behavior depending on the particle orientation. Thus, Ni L-edge peak recovery was strongly dependent on the doping and facet orientation (frontal vs. lateral) of the primary particles. Likewise, all O K spectra consisted of a sharp pre-edge peak at ~540 eV and a broad main-edge peak at ~550 eV. The pre-edge peak intensity gradually decreased when moved from bulk to surface and the pre-edge peak became a shoulder of the main peak at the surface. Furthermore, the intensity reduction of O K pre-edge peak coincides with the position shift of L_3-edge peak in all the cycled electrodes. Therefore, the reduction of Ni valence state and concurrent lattice oxygen loss were smaller in the doped LNCM electrodes, and the lateral facets were less vulnerable to the oxygen loss compared to the frontal facets.

We performed the First-principles calculations to further understand the facet-dependent oxygen vacancy formation (See Experimental section). Figure 3.2.10j and Figure 3.2.10k represents the lateral (003) and frontal (102) planes in $LiNiO_2$ structure, respectively. Due to high Ni contents (over 90%), we adopted the $LiNiO_2$ system which shows the structural and compositional similarity to Ni-rich LNCM according to the previous reports [24,25,55]. The oxygen vacancy formation energy of each surface was calculated as a function of lithium concentration in Li_xNiO_2 (x=1, 0.66, 0.33). From the results (Figure 3.2.10l), the frontal (102) plane was calculated to have a lower oxygen vacancy formation energy compared to the lateral (003) plane in the whole range of lithium content, which indicates that the frontal (102) plane

is more prone to release the oxygen gas. Furthermore, the oxygen vacancy formation energy monotonically decreased with increasing the lithium extraction. Especially, the frontal (102) plane showed the negative oxygen vacancy formation energy (-0.13 eV) at x=0.33, however, the lateral (003) plane still exhibited the positive oxygen vacancy formation energy value (0.35 eV). The lower oxygen vacancy formation energy of frontal (102) plane compared to lateral (003) plane is due to the presence of under-coordinated O atoms in (102) plane [56]. Those oxygens are highly unstable to evolve as oxygen gas with a lower oxygen vacancy formation energy. Overall, these calculations show the facet-dependent oxygen evolution and suggest the importance of the particle orientation.

The loss of oxygen in LNCM inevitably accompanies with the structure transformation from layered structure (R-3m) to spinel structure (Fd-3m) and eventually to rock salt structure (Fm-3m), and the phase transformation starts from the surface and migrates toward the inner bulk [11,16]. To confirm the phase transition, the outmost surfaces of the pristine and cycled electrodes were examined using atomic resolution STEM. The STEM images of the pristine electrodes showed a sub-nanometer thick cation-mixed layer on the surface, and the frontal and lateral facets had the similar thickness of cation-mixed layer (notated as surface reconstructed layer (SRL)) (Figure 3.2.11a, c). After 50 cycles at 0.3 C, the inner bulk of the LNCM electrodes maintained the original R-3m layered structure, but SRL on the surface significantly propagated toward the inner bulk and exhibited the anisotropic behavior depending on the particle orientation (Figure 3.2.11b, d). The fast Fourier transform (FFT) patterns indicated that SRL on the surface was NiO-like rock salt (Fm-3m) phase. The thickness of SRL was estimated ~6 and ~3 nm for frontal and lateral facets of both P-LNCM and B-LNCM, respectively (Figure 3.2.11b, d). The obtained results were consistent with the depth of oxygen loss determined by

EELS analysis and thus, the propagation of SRL was influenced by the presence of dopant and/or facet orientation.

To support the EELS and STEM results, *Operando* differential electrochemical mass spectrometry (DEMS) experiment was performed to monitor the gas evolution during charge process (Figure 3.2.12a, b, c). The O_2 and CO_2 release was monitored by increasing the charging voltage up to 4. 8 V at the current density of 0.1 C. For all three cathodes, O_2 started to evolve after the H2 phase and the gas evolution rate increased with raising the charge potential and reached its maximum at 4.8 V. This is because the lattice oxygen becomes more vulnerable with increasing the lithium extraction from the crystalline structure (Figure 3.2.10l) [14]. The accompanying CO_2 was resulted from the chemical oxidization of the electrolyte by the oxygen radicals that were released from the LNCM [28,29]. As expected, the amount of gases released decreased in the order of U-LNCM, P-LNCM, and B-LNCM. Thus, the B-LNCM electrode showed a minimal amount of O_2 and CO_2 evolution during charge process, demonstrating the high oxygen stability.

Based on the EELS, STEM, and DEMS analyses, it was found that the oxygen release and cation migration behavior were anisotropic and depended on the facet orientation of the primary particle, that is, the frontal facets have more vulnerable characteristics compared to lateral facets. As described earlier, the primary particles of B-LNCM were much thinner plates and thus, had more lateral facets and less frontal facets (in terms of the area) compared to P-LNCM. This implies that B-LNCM is more resistant to the oxygen loss and phase transformation during cycling, which results in the better cycle performance compared to P-LNCM (Figure 3.2.12d).

To prove the above hypothesis, the P-LNCM and B-LNCM electrodes were further examined by soft X-ray absorption spectroscopy (sXAS) using a fluorescence yield (FY) mode (depth

sensitivity of ~200 nm from the particle surface) [57]. For the O K-edge sXAS spectra, the pre-edge peak (from 528 to 535 eV) arises from the excitation of O_{1s} electron to unoccupied states of hybridized TM_{3d}-O_{2p} orbitals, while the broad peak above 535 eV corresponds to the excitation to unoccupied TM_{4sp}-O_{2p} hybridized orbitals (Figure 3.2.12e, f) [58-60]. The pre-edge peak was mainly focused in this research as the 3d orbitals of TM contribute to the main redox activity in the Ni-rich layered cathodes. For the pristine electrodes, only lattice oxygen peak of layered cathodes was detected at 529.5 eV. However, after multiple cycles, the intensity of layered lattice oxygen peak at 529.5 eV decreased and a new peak at 533 eV appeared in the cycled P-LNCM electrode, which can be attributed to the presence of NiO-type rock-salt (Figure 8e) [59,60]. On the contrary, the depression of layered lattice oxygen peak was rather small and the peak at 533.2 eV was hardly observed in the cycled B-LNCM electrode (Figure 3.2.12f), indicating that the B-LNCM electrode was more resistant against the phase transition during cycling. In case of Ni L-edge, due to the spin-orbit coupling of the core hole, Ni L-edge sXAS spectrum is divided into two separated energy bands, namely L_3-edge (Ni $2p_{3/2}$) at lower energy and L_2-edge (Ni $2p_{1/2}$) at higher energy (Figure 3.2.12g, h) [59]. In addition, the 2p-3d interaction and crystal field effect further split the L3-edge into a low energy band (L_{3L}) at ~855 eV and a high energy band (L_{3H}) at ~856.5 eV. In case of the P-LNCM electrode (Figure 3.2.12g), compared to the pristine electrode, the L_{3L}/L_{3H} ratio increased and the L_2-edge shifted to the lowed energy after cycling. This indicates an evolution of transition metal 3d bands to higher occupancies, that is, reduced oxidation states [60]. On the other hand, the Ni L-edge spectrum of the cycled B-LNCM electrode was almost identical to that of the pristine electrode, implying that the B-LNCM electrode effectively maintained its original Ni valence state and layered structure during cycling. Overall, the sXAS results showed that B-LNCM effectively suppressed the phase transformation during cycling compared to P-LNCM electrode. Therefore,

by conducting the various measurements, this research has revealed three findings; (1) origin of excellent cyclability of B-LNCM to be suppression of microcrack and alleviation of oxygen evolution, (2) importance of facet development to minimize the oxygen release, and (3) significance of oxygen evolution control for the battery performance improvement.

3.2.3. Conclusions

Herein, the Ni-rich layered oxides with textured microstructure were developed using boron and phosphorous as dopants and electrochemically tested for LIB cathode materials. Both P-LNCM and B-LNCM exhibited the textured microstructure with primary particles aligned along the radial direction, however, they differed in facet area ratio. While both P-LNCM and B-LNCM cathodes mitigated the particle cracks during cycling attributed by their textured microstructure, B-LNCM showed much improved cycle stability, which indicates that the microcrack suppression was not the only reason for the enhanced performance of B-LNCM. By utilizing the various measurements, we have revealed that the difference was highly related with the behavior of oxygen stability that depended on the facet orientation of the primary particles. The B-LNCM primary particles had more lateral facets ({003} plane) that are stable against oxygen release, leading to the better cycle life compared to P-LNCM. The insight obtained in this work suggests that not only restraining the particle cracks but also suppressing the oxygen release are important factors for further improvements in state-of-the-art Li ion battery cathode materials.

3.2.4. Experimental procedure

Materials preparation

$Ni_{0.92}Co_{0.04}Mn_{0.04}(OH)_2$ hydroxide precursor was prepared by a co-precipitation method using $NiSO_4 \cdot 6\,H_2O$ (Daejung Chemical Co.), $CoSO_4 \cdot 7\,H_2O$ (Daejung Chemical Co.), $MnSO_4 \cdot H_2O$ (Daejung Chemical Co.), NaOH (Daejung Chemical Co.), and NH_4OH (Daejung Chemical Co.) as starting materials. For a typical synthesis, a homogeneously-mixed solution (Ni:Co:Mn= 92:4:4 in molar ratio) was fed into a batch reactor filled containing a solution of NH_4OH (aq) and NaOH (aq) under a N_2 atmosphere. Concurrently, NaOH (molar ratio of NaOH/TM=2.0) and NH_4OH as a chelating agent (molar ratio of NH_4OH/TM=1.2) were pumped separately into the reactor. The precursor powder was obtained by filtering, washing, and vacuum drying the obtained precipitate at 110 °C for 12 h. The hydroxide precursor was mixed with $LiOH \cdot H_2O$ with a molar ratio of 1:1.03 and calcined at 740 °C for 12 h with an oxygen flow to obtain U-LNCM. For the synthesis of P-LNCM and B-LNCM, hydroxide precursor was mixed with $LiOH \cdot H_2O$ and 1 mole % of $NH_4H_2PO_4$ (Sigma-Aldrich) or 1 mole % of B_2O_3 (Sigma-Aldrich) as phosphorus and boron source, respectively and calcined at the same conditions.

Characterization

Fourier transformation infrared spectroscopy (FT-IR) was measured in ATR mode using a germanium (Ge) window (Nicolet 6700, Thermo Scientific). The chemical composition was analyzed by inductively coupled plasma-atomic emission spectroscopy (ICP-AES) (OPTIMA 4300DV, PerkinElmer). The crystal structure was determined based on the synchrotron radiation powder X-ray diffraction (HRRD) data collected at room temperature from the 9B HRPD beamline at the Pohang Accelerator Laboratory (PAL). The Rietveld refinement was

performed using the Fullprof program. The Rietveld refinement of the electrodes in Figure S5 was conducted by subtracting the Al foil peak beforehand. The Ni K-edge, Co K-edge, and Mn K-edge X-ray absorption near-edge structure (XANES) spectra were collected on the 7D beam line at PAL with top-up mode operation under a ring current of 200 mA at 3.0 GeV. The phase transition during charge was measured by *in-situ* battery cell X-ray diffractometer (R-AXIS IV, RIGAKU). The modified coin-type cell with a 3 mm hole at its center sealed with mylar film was used for the experiments. *In-situ* XRD measurements were conducted at a current density of 0.2 C with charging voltage up to 4.4 V vs Li/Li^+, while the electrodes were pre-cycled before the measurements. The diffraction patterns were acquired with a time resolution of 10 min. The thermal stability of the charged cathodes was conducted by DSC (Diamond DSC, PerkinElmer) measurements. The morphology of the particles was observed by SEM (SU-70, Hitachi) and TEM (JEM-2100F, JEOL), while the crystallographic orientation maps were obtained with a JEM-2100F with a voltage of 200 kV equipped with an ASTAR (NanoMEGAS) device. The high-resolution STEM images and electron energy loss spectroscopy (EELS) were obtained from a double aberration-corrected JEOL-ARM 200CF microscope with a cold-field emission gun operated at an acceleration voltage of 200 kV, which is installed at the National Center for Inter-University Research Facilities (NCIRF) in Seoul National University. The cross-sectional TEM specimens were prepared using a FIB (Helios Nano Lab450, FEI), while the cross-sectional SEM specimens were prepared by cross-section polisher (IB-19510CP, JEOL). Soft X-ray absorption spectroscopy (sXAS) measurements were performed with the 10D XAS-KIST beamline at PAL. The grating with 1100 grooves/mm was used to obtain the spectra at Ni L-edge and O K-edge. The obtained sXAS spectra were background-subtracted and normalized with respect to the post-edge height. For differential electrochemical mass spectrometry (DEMS) measurements, the electrodes were fabricated by casting the slurry onto

Al mesh (AL008772, Goodfellow) with a mass loading of ~10 mg cm^{-2}, while the cathodes were fabricated in a glove box using Li metal as counter electrode. The details for DEMS experimental setup are provided elsewhere [29,61]. For the DEMs analysis, the cell was charged to 4.8 V vs Li/Li^+ at a current density of 0.1 C.

First Principles Calculations (DFT)

First-principles calculations were conducted using Vienna ab-initio simulation package (VASP) based on density functional theory (DFT).[62] Projector augmented wave pseudopotentials (PAW) were used, and a kinetic energy cutoff of the plane-wave basis set was 500 eV [63]. All calculations were performed within spin-polarized generalized gradient approximation with Hubbard–U correction (GGA+U) [64] using the Perdew-Burke-Ernzerhof (PBE) functional [65]. Effective Hubbard–U parameters of 6.4 were selected to depict the 3d electrons in Ni atoms [66]. 3×3×2 and 2×2×1 k-pint grids based on the Monkhorst-Pack scheme were used for bulk relaxation ($Li_{12}Ni_{12}O_{24}$) and surface energy calculation ($Li_{24}Ni_{48}O_{96}$), respectively [67]. All structures were fully relaxed until the interatomic forces were smaller than 0.02 eV/Å.

Slab-surface models were used to describe (003) and (102) surface with different lithium concentrations in Li_xNiO_2 (x = 1, 0.66, 0.33). To figure out the lithium arrangement at the composition which is $Li_{0.66}NiO_2$ and $Li_{0.33}NiO_2$, the 30 lowest electrostatic energy configurations were chosen using the Ewald summation method in the bulk structure ($Li_{12}Ni_{12}O_{24}$) [68,69]. The vacuum-slab thickness (15 Å) was considered to prevent self-interaction errors between the periodic images. Oxygen vacancy formation energy (E_f) at (003) and (102) layer was defined as:

$$E_f = E^{DFT}(Li_xNi_{48}O_{95}) + \frac{1}{2} E(O_2) - E^{DFT}(Li_xNi_{48}O_{96})$$

Where E (O_2) is equivalent with Gibbs free energy of gaseous O_2 and varies along the temperature. We adopted Gibbs free energy of O_2 at 300K, which is 8.99 eV/molecule as reported [70-72].

Electrochemical Test

The half-cell electrochemical properties were evaluated by using 2032 coin-type cells (Welcos, Korea), which were fabricated in Ar-filled glove box. The cathodes were prepared by dissolving 85 wt % active material, 8 wt % carbon black (Super P), and 7 wt % polyvinylidene fluoride (PVDF) in *N* -methyl-2-pyrrolidone (NMP), which were casted on an Al foil with a mass loading of ~8 mg cm^{-2}. The cell was assembled by using Li-metal foil as a counter electrode and a separator film (Celgard) filled with $LiPF_6$ (1.2 M) solution dissolved in an ethyl carbonate-ethyl methyl carbonate mixture (3:7 *v*/*v*) with no electrolyte additive. The cells were galvanostatically charged and discharged at voltage between 2.5 and 4.4 V vs Li/Li^+ at room temperature using automatic battery cycler (WBCS 3000S WonATech). The current density of 1 C represents 200 mA g^{-1}. The galvanostatic intermittent titration technique (GITT) was conducted by applying a 0.1 C current for 20 min and subsequent resting for 1 h with a voltage range of 2.5~4.4 V. The electrochemical impedance test spectroscopy (EIS) measurements were taken over in a frequency range of 1000 kHz to 5 mHz with an AC amplitude of 10 mV using ZIVE SP1 potentiostat/galvanostat/EIS.

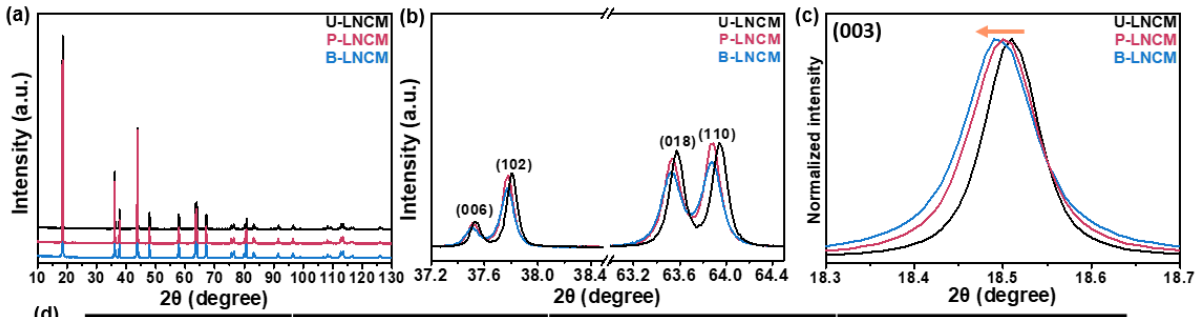

(d)

Sample	a-axis[Å]	c-axis[Å]	V[Å]
U-LNCM	2.87378 (1)	14.18950 (8)	101.486 (1)
P-LNCM	2.87631 (2)	14.19580 (2)	101.709 (1)
B-LNCM	2.87642 (2)	14.19793 (10)	101.733 (1)

Figure 3.2.1. (a) HRPD patterns of as-synthesized U-LNCM, P-LNCM, and B-LNCM powders. Enlarged patterns for (b) (006)/(102) and (018)/(110) peaks and (c) (003) peaks. (d) Calculated lattice parameters by Rietveld refinement for as-synthesized U-LNCM, P-LNCM, and B-LNCM powders.

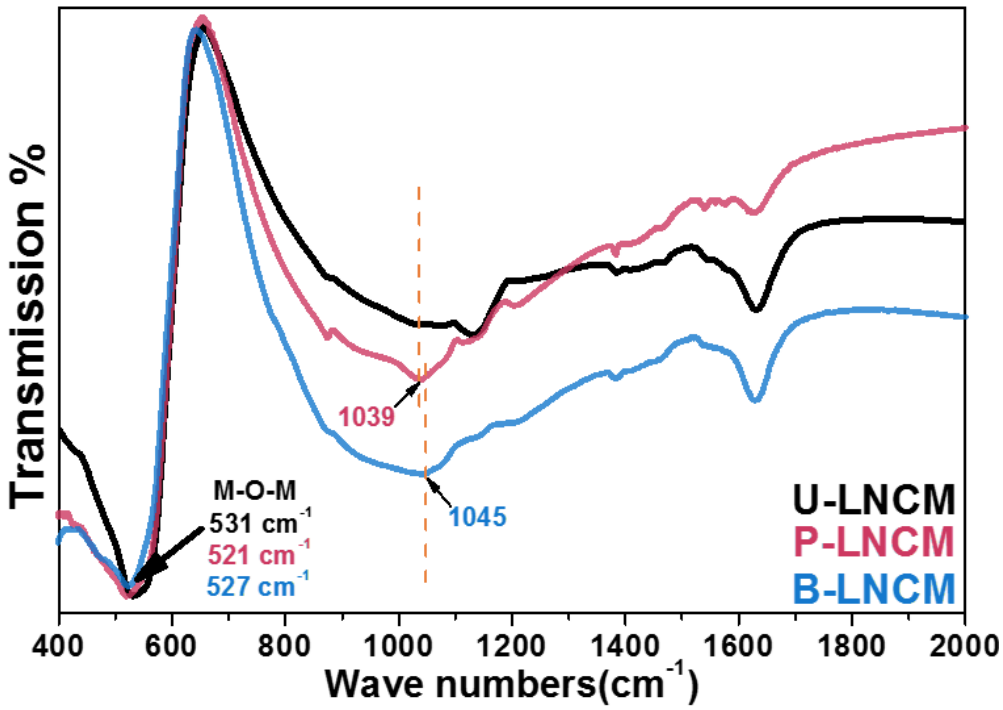

Figure 3.2.2. FT-IR spectra of as-synthesized U-LNCM, P-LNCM, and B-LNCM powders.

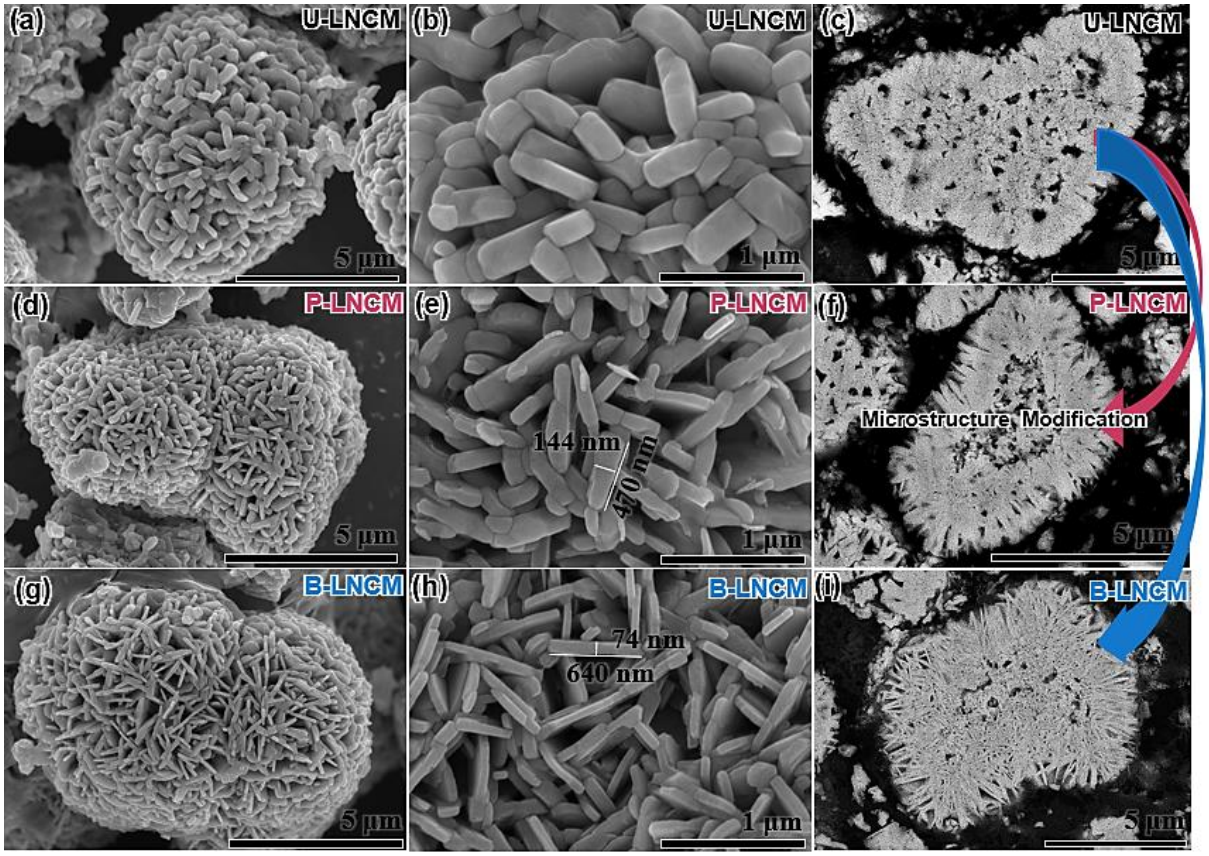

Figure 3.2.3. Low maginification SEM images of (a) U-LNCM, (d) P-LNCM, and (g) B-LNCM, high maginification SEM images of (b) U-LNCM, (e) P-LNCM, and (h) B-LNCM, and cross-sectioned polished SEM images of (c) U-LNCM, (f) P-LNCM, and (i) B-LNCM powders.

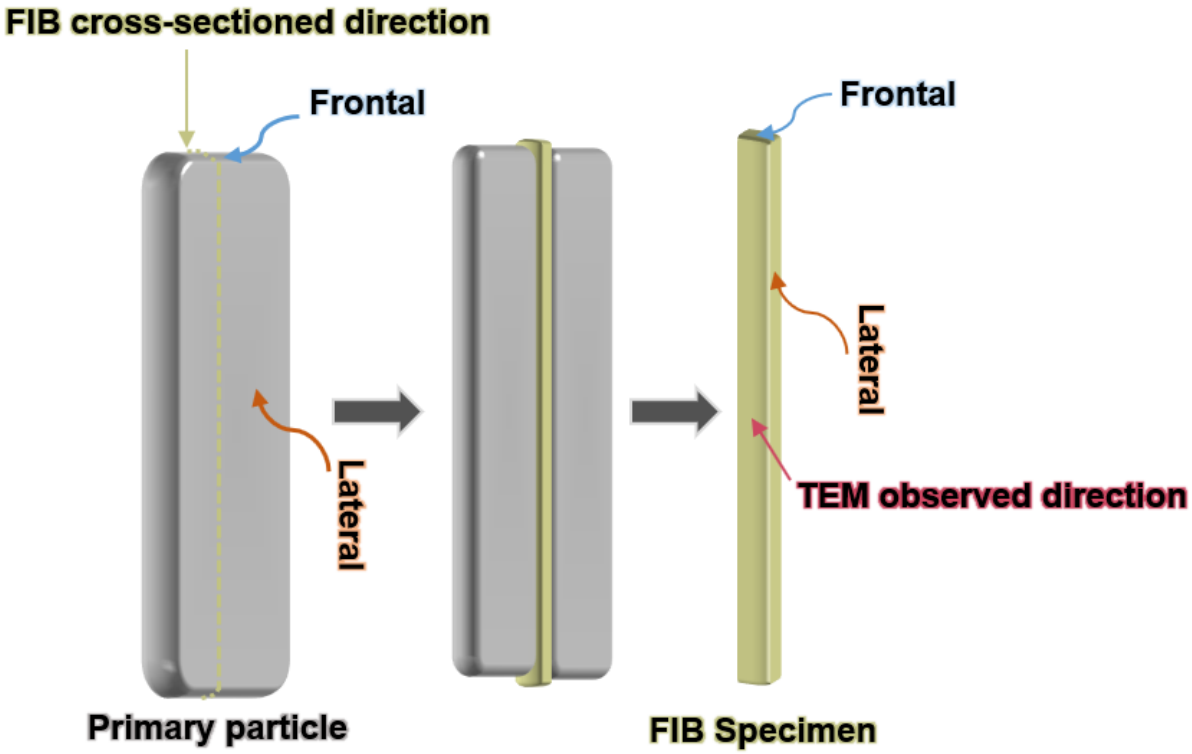

Figure 3.2.4. Schematic illustration for the FIB preparation and TEM observing direction.

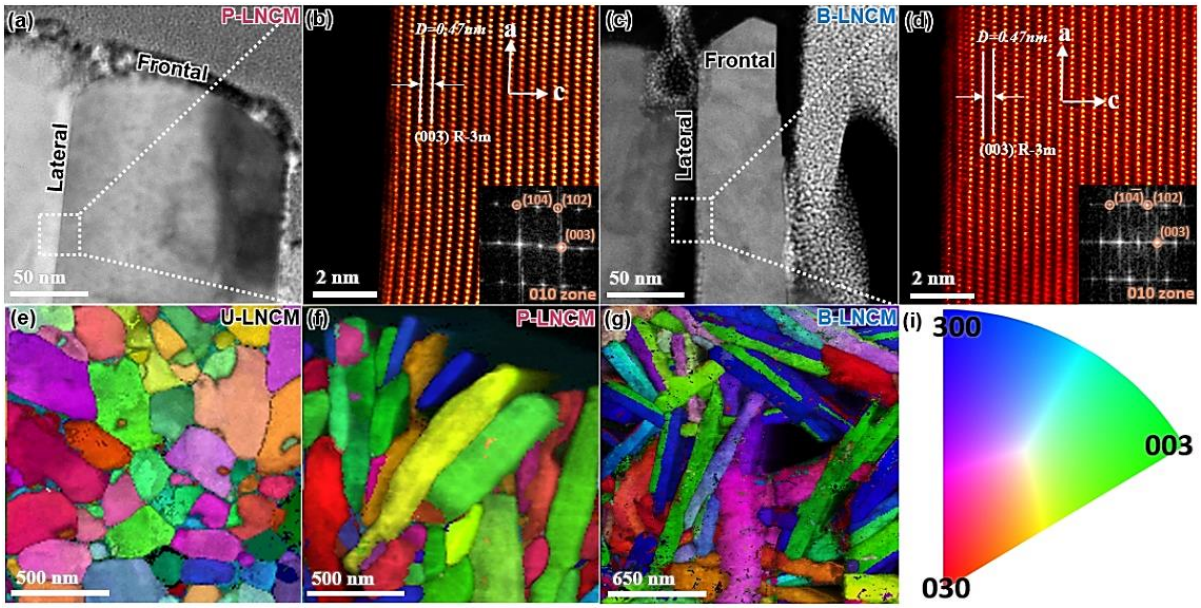

Figure 3.2.5. (a) HR-TEM image of P-LNCM particle and (b) atomic resolution image of marked area in (a), (c) HR-TEM image of B-LNCM particle and (d) atomic resolution image of marked area in (c). Color-coded crystallographic orientation maps of cross-sectional TEM sample of (e) U-LNCM, (f) P-LNCM, and (g) B-LNCM obtained by ASTAR device (NanoMEGAS) (The orientation of the planes is normal to z-axis), and (i) color codes for the crystal orientation maps expressed in the standard stereographic triangle notation.

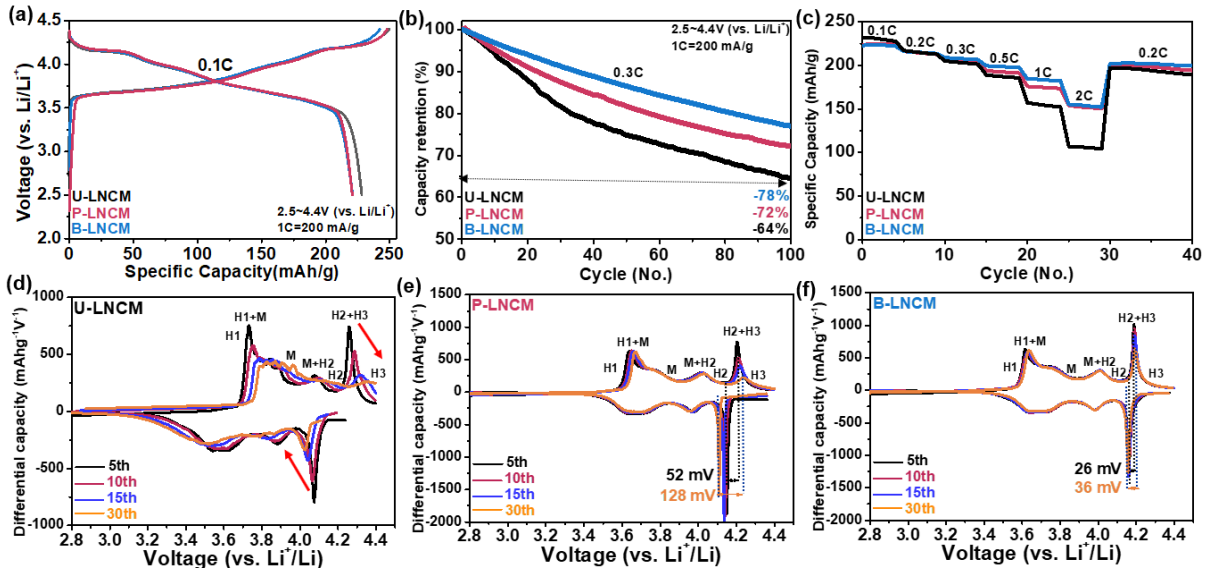

Figure 3.2.6. (a) Initial charge-discharge voltage profiles of U-LNCM, P-LNCM, and B-LNCM electrodes between 2.5 and 4.4 V (vs. Li^+/Li) at the current density of 0.1 C (1 C= 200 mA g^{-1}), (b) cycle performance of U-LNCM, P-LNCM, and B-LNCM electrodes at the current density of 0.3 C, (c) rate test for the three electrodes, and dQ dV^{-1} profiles obtained by differentiating the charge-discharge profiles at 5^{th}, 10^{th}, 15^{th}, and 30^{th} cycles for (d) U-LNCM, (e) P-LNCM, and (f) B-LNCM electrodes.

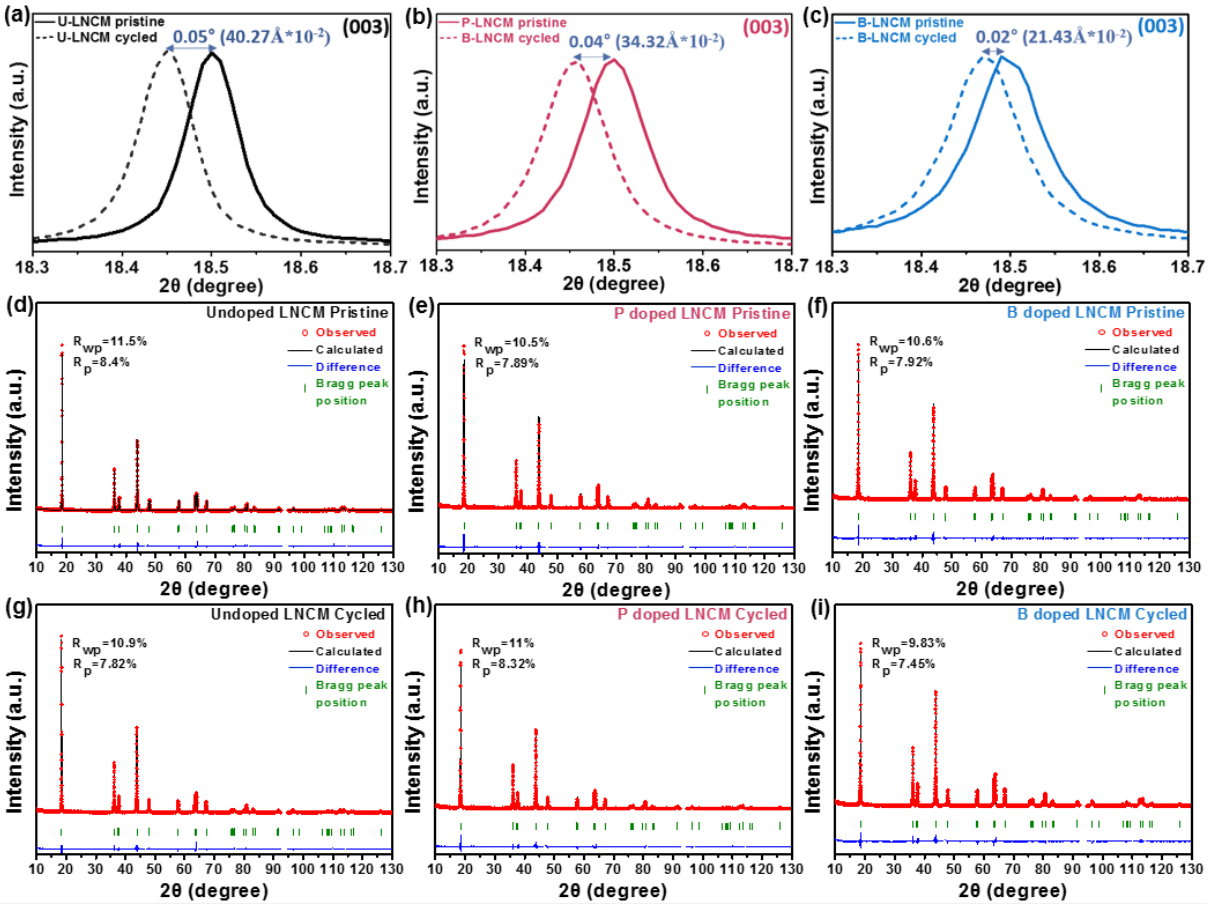

Figure 3.2.7. Enlarged HRPD patterns of (003) peak for (a) pristine/cycled U-LNCM, (b) pristine/cycled P-LNCM, and (c) pristine/cycled B-LNCM electrodes. Rietveld refinement results of (d) pristine U-LNCM, (e) pristine P-LNCM, (f) pristine B-LNCM, (g) cycled U-LNCM, (h) cycled P-LNCM, and (i) cycled B-LNCM electrodes.

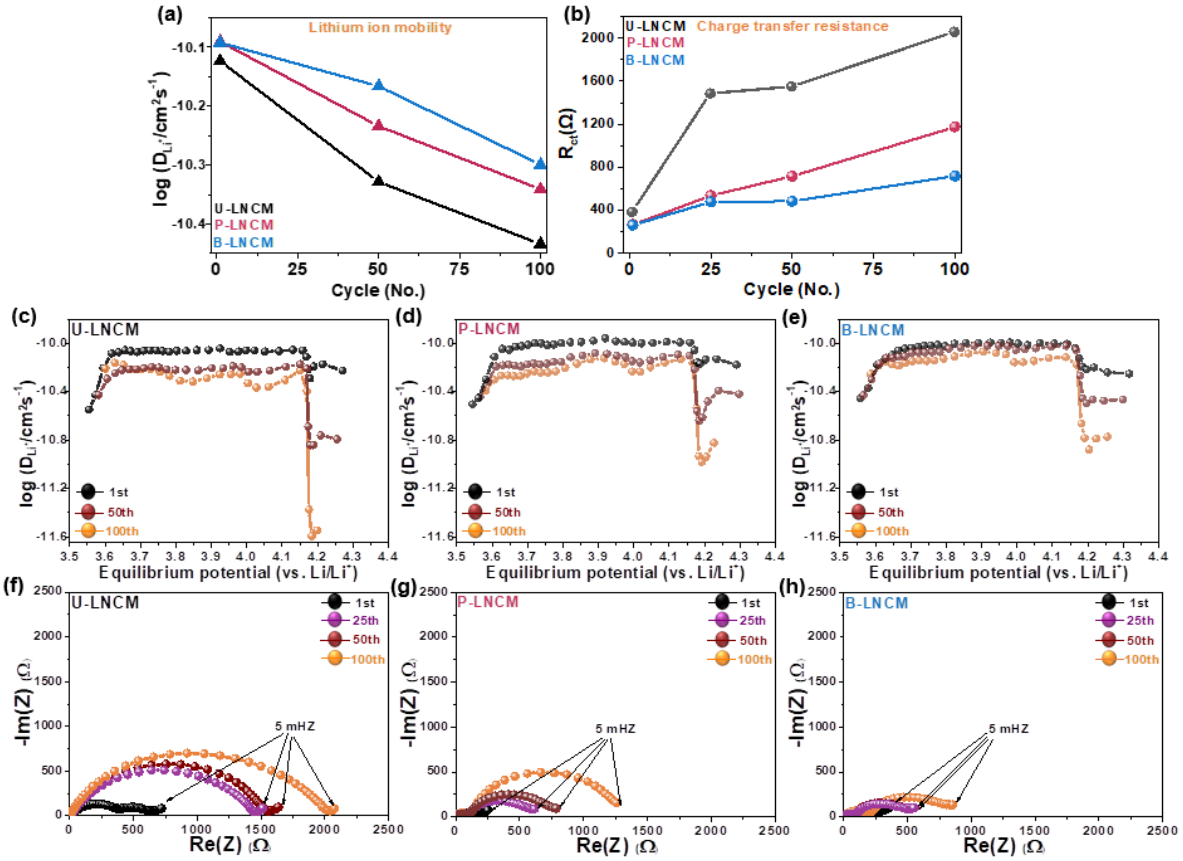

Figure 3.2.8. Variation of (a) lithium ion mobility and (b) charge transfer resistance depending on cycles. Lithium ion mobility was calculated by GITT measurement whereas charge transfer resistance was determined by EIS measurement. GITT measurements for (c) U-LNCM, (d) P-LNCM, and (e) B-LNCM. EIS measurements for (f) U-LNCM, (g) P-LNCM, and (h) B-LNCM electrodes.

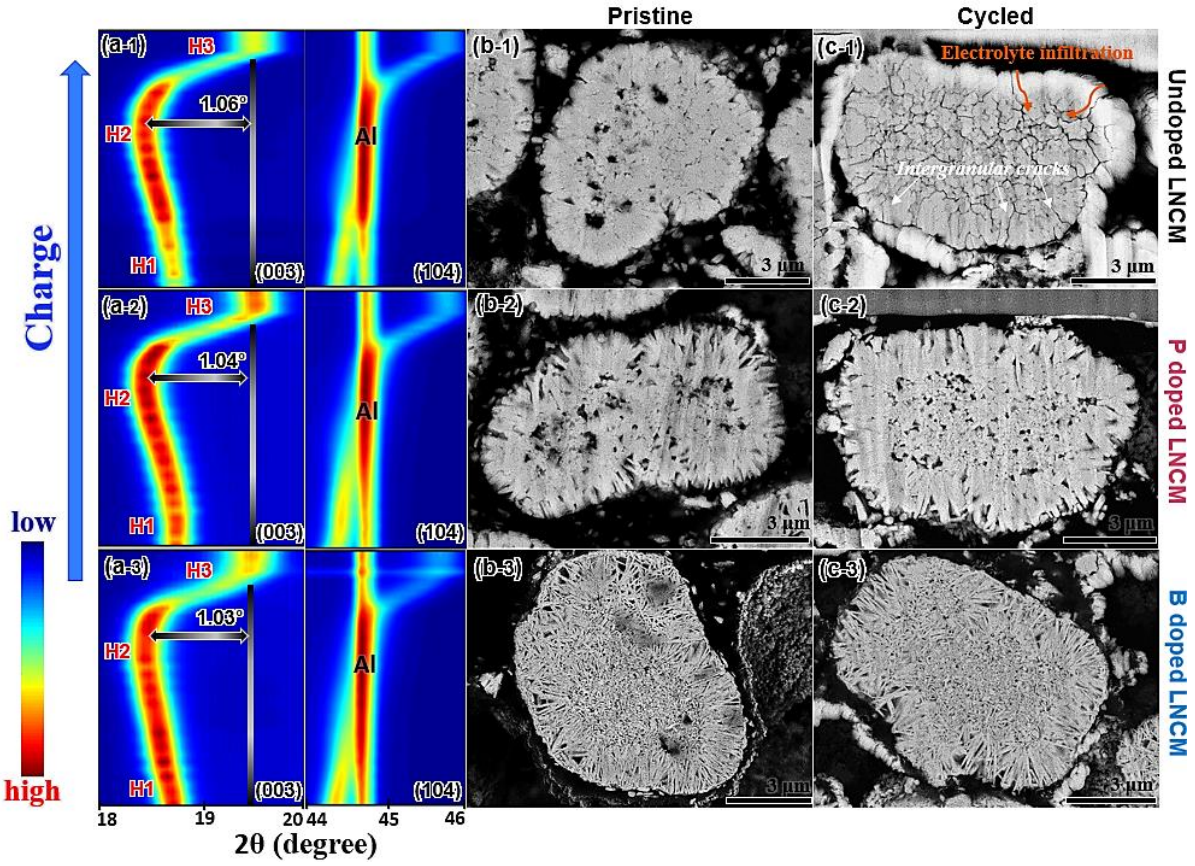

Figure 3.2.9. *In situ* XRD patterns of (a-1) U-LNCM, (a-2) P-LNCM, and (a-3) B-LNCM electrodes and cross-sectioned polished SEM images of pristine (b-1) U-LNCM, (b-2) P-LNCM, and (b-3) B-LNCM electrodes and after 50th cycled (c-1) U-LNCM, (c-2) P-LNCM, and (c-3) B-LNCM electrodes.

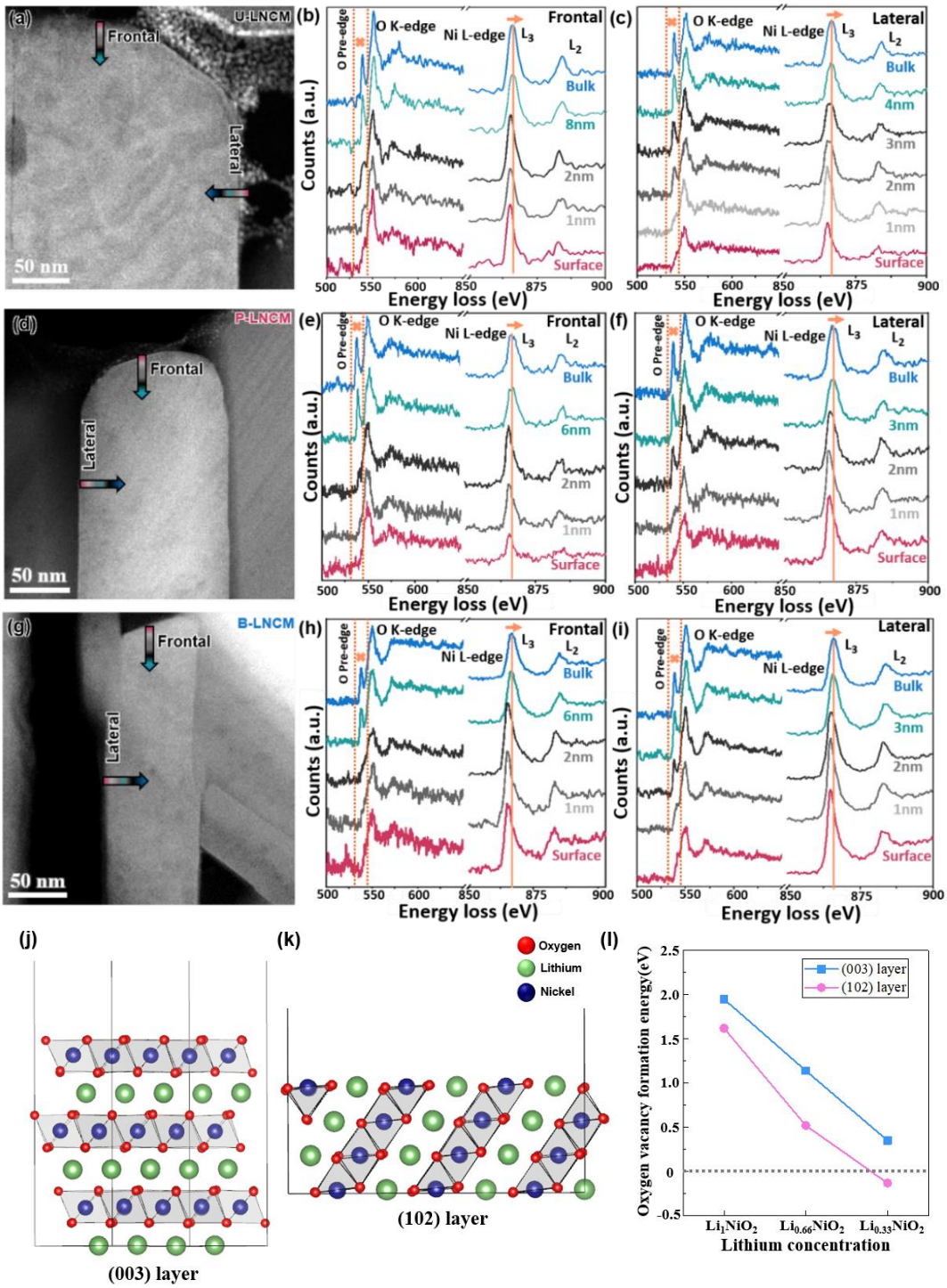

Figure 3.2.10. HR-TEM images of cycled (a) U-LNCM, (d) P-LNCM, and (g) B-LNCM electrodes, line-scanning EELS spectra of O K-edge and Ni L-edge (as-labeled) for (b) frontal and (c) lateral facets of cycled U-LNCM, (e) frontal and (f) lateral facets of cycled P-LNCM, and (h) frontal and (i) lateral facets of cycled B-LNCM electrodes. (j) (003) plane and (k) (102) plane for $LiNiO_2$, and (l) oxygen vacancy formation energy of (003) and (102) planes.

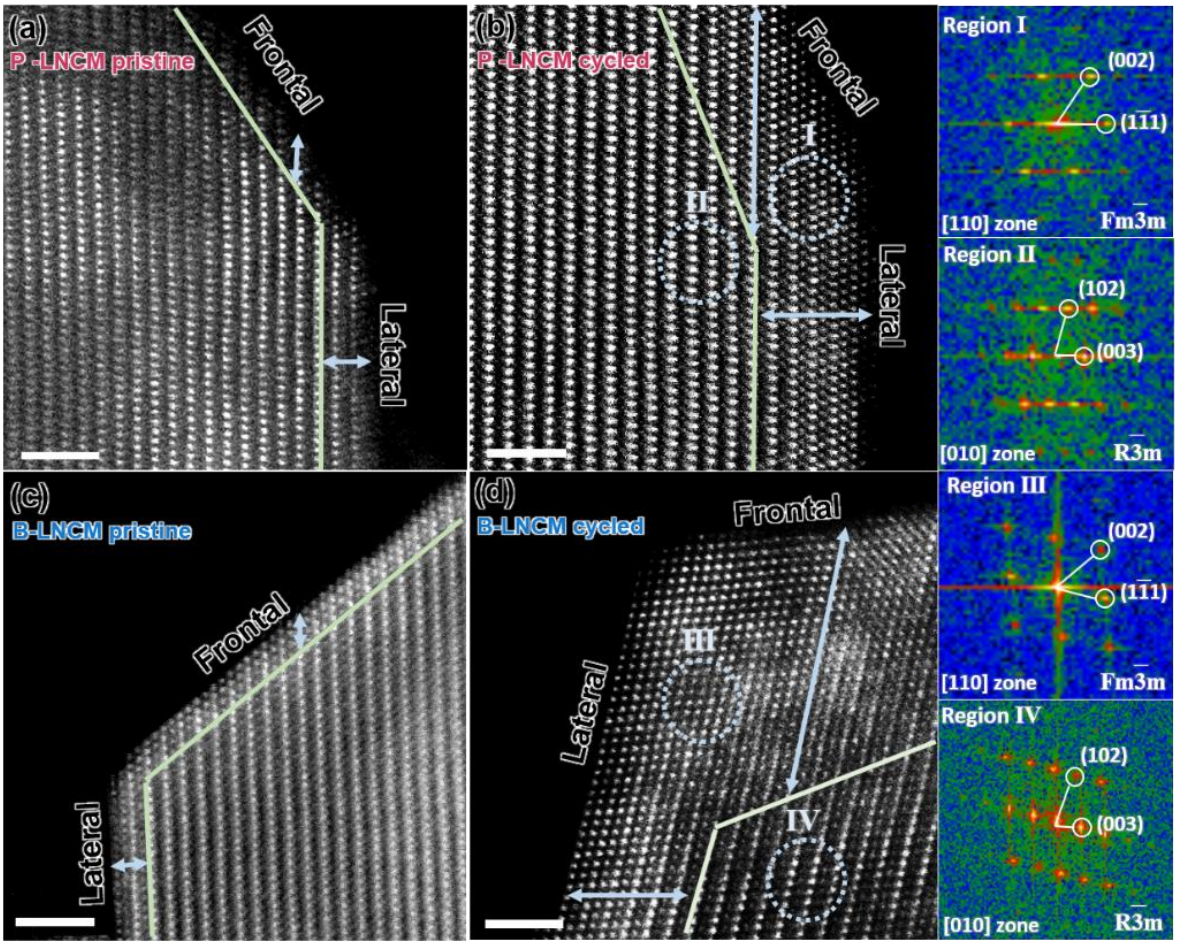

Figure 3.2.11. Atomic-resolution STEM images of (a) P-LNCM pristine, (b) P-LNCM cycled, (c) B-LNCM pristine, and (d) B-LNCM cycled electrodes. Scale bars are 2 nm.

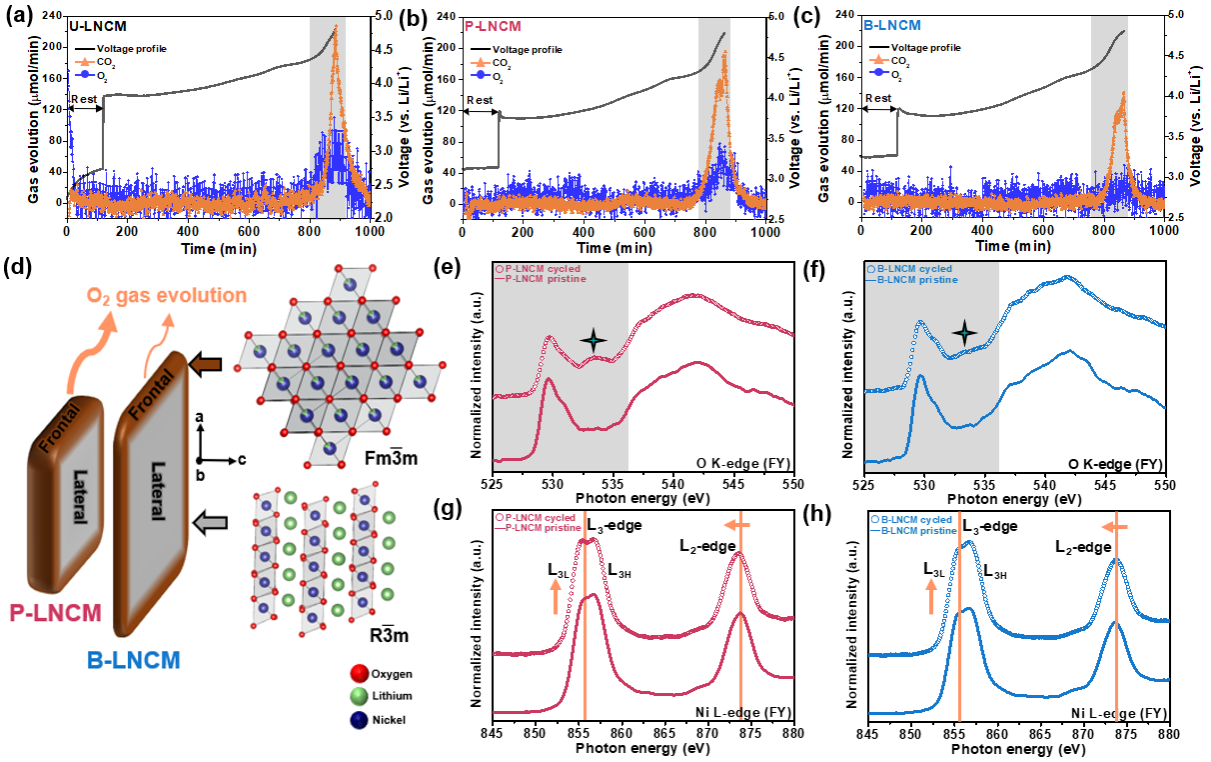

Figure 3.2.12. Differential electrochemical mass spectrometry (DEMS) spectra of (a) U-LNCM, (b) P-LNCM, and (c) B-LNCM electrodes when charged to 4.8 V at 0.1 C current density, (d) schematic illustration of cycle stability difference between P-LNCM and B-LNCM electrodes, and soft X-ray absorption spectroscopy (sXAS) O K-edge FY mode spectra for pristine/cycled (e) P-LNCM and (f) B-LNCM electrodes and sXAS Ni L-edge FY mode spectra for pristine/cycled (g) P-LNCM and (h) B-LNCM electrodes.

3.2.5. Reference

[1] J. Wang, Y. Yamada, K. Sodeyama, C. H. Chiang, Y. Tateyama and A. Yamada, Nat. Commun. 2016, 7, 12032

[2] M. D. Radin, S. Hy, M. Sina, C. Fang, H. Liu, J. Vinckeviciute, M. Zhang, M. S. Whittingham, Y. S. Meng, A. Van der Ven, Adv. Energy Mater. 2017, 7, 1602888

[3] P. K. Nayak, E. M. Erickson, F. Schipper, T. R. Penki, N. Munichandraiah, P. Adelhelm, H. Sclar, F. Amalraj, B. Markovsky, D. Aurbac, Adv. Energy Mater. 2018, 8, 1702397

[4] J. Kim, H. Lee, H. Cha, M. Yoon, M. Park, J. Cho, Adv. Energy Mater. 2018, 8, 1702028

[5] W. Li, E. M. Erickson, A. Manthiram, Nat. Energy. 2020, 5, 26

[6] L. D. Biasi, B. Schwarz, T. Brezesinski, P. Hartmann, J. Janek, H. Ehrenberg, Adv. Mater. 2019, 31, 1900985

[7] Y. -K. Sun, ACS Energy Lett. 2019, 4, 1042

[8] U.-H. Kim, L. -Y. Kuo, P. Kaghazchi, C. S. Yoon, Y. -K. Sun, ACS Energy Lett. 2019, 4, 576

[9] X. Han, L. Lu, Y. Zheng, X. Feng, Z. Li, J. Li, M. Quyang, eTransportation. 2019, 1, 100005

[10] J. -H. Kim, H. -H. Ryu, S. J. Kim, C. S. Yoon, Y. -K. Sun, ACS Appl. Mater. Interfaces. 2019, 11, 30936

[11] A. Manthiram, B. Song, W. Li, Energy Storage Mater. 2017, 6, 125

[12] W. Li, H. Y. Asl, Q. Xie, A. Manthiram, J. Am. Chem. Soc. 2019, 141, 5097

[13] K. -W. Nam, S. -M. Bak, E. Hu, X. Yu, Y. Zhou, X. Wang, L. Wu, Y. Zhu, K. -Y. Chung, X. -Q. Yang, Adv. Funct. Mater. 2013, 23, 1047

[14] L. D. Biasi, A. Schiele, M. Roca-Ayats, G. Garcia, T. Brezesinski, P. Hartmann, J. Janek, ChemSusChem. 2019, 12, 2240

[15] H. -H. Ryu, K. -J. Park, C. S. Yoon, Y. -K. Sun, Chem. Mater. 2018, 30, 1155

[16] J. H. Choi, S. Y. Lee, S. M. Yoon, K. H. Kim, M. Kim, and S. H. Hong, ChemSusChem. 2019, 12, 2439

[17] U. H. Kim, D. W. Jun, K. J. Park, Q. Zhang, P. Kaghazchi, D. Aurbach, D. T. Major, G. Goobes, M. Dixit, N. Leifer, C. M. Wang, P. Yan, D. Ahn, K. H. Kim, C. S. Yoon and Y. K. Sun, Energy Environ. Sci. 2018, 11, 1271

[18] H. Kim, J. Jang, D. Byun, H. S. Kim, and W. Choi, ChemSusChem. 2019, 12, 5253

[19] W. Liu, X. F. Li, D. B. Xiong, Y. C. Hao, J. W. Lia, H. R. Kou, B. Yan, D. J. Lia, S. G. Lu, A. Koo, K. Adair, X. L. Sun, Nano Energy. 2018, 44, 111

[20] H. J. Kim, S. H. Lee, H. Cho , J. H. Kim , J. Lee , S. H. Park , S. H. Joo , S. H. Kim , Y. G. Cho , H. K. Song , S. K. Kwak, and J. P Cho, Adv. Mater. 2016, 28, 4705

[21] U. H. Kim, H. H. Ryu, J. H. Kim, R. B. Mücke, P. Y. Kaghazchi, C. S. Yoon, and Y. K. Sun, Adv. Energy Mater. 2019, 9, 1803902

[22] X. Xu, H. Huo, J. Jian, L. Wang, H. Zhu, S. Xu, X. He, G. Yin, C. Du, X. Sun, Adv. Energy Mater. 2019, 9, 1803963

[23] X. M. Fan, G. R. Hu, B. Zhang, X. Ou, J. F. Zhang, W. G. Zhao, ,H. P. Jia, L. F. Zou, P. Li, Y. Yang, Nano Energy. 2020, 70, 104450

[24] H. -H. Ryu, N. -Y. Park, J. H. Seo, Y. -S. Yu, M. Sharma, R. Mucke, P. Kaghazchi, C. S. Yoon, Y. -K. Sun, Mater. Today. 2020, 36, 73

[25] K. -J. Park, H. -G. Jung, L. -Y. Kuo, P. Kaghazchi, C. S. Yoon, Y. -K. Sun, Adv. Energy Mater. 2018, 8, 180102

[26] H. H. Ryu, N. -Y. Park, D. R. Yoon, U. -H. Kim, C. S. Yoon, Y. -K. Sun, Adv. Energy Mater. 2020, 10, 2000495

[27] F. Kong, C. Liang, L. Wang, Y. Zheng, S. Perananthan, R. C. Longo, J. P. Ferraris, M. Kim,

K. Cho, Adv. Energy Mater. 2019, 9, 1802586

[28] J. Wandt, A. T. S. Freiber, A. Ogrodnik, H. A. Gasteiger, Mater. Today. 2018, 21, 825

[29] R. Jung, M. Metzger, F. maglia, C. Stinner, H. A. Gasteiger, J. Phys. Chem. Lett. 2017, 8, 4820

[30] L. Pan, Y. Xia, B. Qiu, H. Zhao, H. Guo, K .Jia, Q. Gu, Z. Liu, J. Power Sources. 2016, 327, 273

[31] Q. Xie, W. Li, A. Dolocan, A. Manthiram, Chem. Mater. 2019, 31, 8886

[32] H. Z. Zhang, Q. Q. Qiao, G. R. Li, X. P. Gao, J. Mater. Chem. A. 2014, 2, 7454

[33] A. Yuan, H. Tang, L. Liu, J. Ying, L. Tan, L. Tan, R. Sun, J. Alloys Compd. 2020, 844, 156210

[34] P. K. Nayak, J. Grinblat, M. Levi, E. Levi, S. Kim, J. W. Choi, D. Aurbach, Adv. Energy Mater. 2016, 6, 1502398

[35] X. Xu, H. Huo, J. Jian, L. Wang, H. Zhu, S. Xu, X. He, G. Yin, C. Du, X. Sun, Adv. Energy Mater. 2019, 9, 1803963

[36] S. -Y. Lee, G. -S. Park, C. Jung, D. -S. Ko, S. -Y. Park, H. G. Kim, S. -H. Hong, Y. Zhu, M. Kim, Adv. Sci. 2019, 6, 1800843

[37] F. S. Serafini, M. Peruzzo, I. Krindges, M. Felipe C. Ordonez, D. Rodrigues, R. M. Souza, M. Cristina M. Farias, Mater. Charact. 2019, 152, 253

[38] D. He, C. Gao, Ceram. Int. 2018, 44, 16246

[39] M. S. Chuang, S. T. Lin, J. Mater. Eng. Perform. 2003, 12, 23

[40] X. Z. Ma, Z. L. Xiang, M. Z. Ma, C. Tan, Z. A. Yang, G. L. Shen, Z. Y. Chen, Q. Shu, Mater. Sci. Eng., A. 2020, 772, 138749

[41] M. J. Bermingham, S. D. McDonald, K. Nogita, D. H. St. John, M. S. Dargusch, Scr. Mater. 2008, 59, 538

[42] S. -K. Jung, H. Gwon, J. Hong, K. -Y. Park, D. -H. Seo, H. Kim, J. Hyun, W. Yang, K. Kang, Adv. Energy Mater. 2014, 4, 1300787

[43] Z. Zhu, D. Yu, Y. Yang, C. Su, Y. Huang, Y. Dong, I. Waluyo, B. Wang, A. Hunt, X. Yao, J. Lee, W. Xue, J. Li, Nat. Energy. 2019, 4, 1049

[44] C. -H. Jung, K. -H. Kim, S. -H. Hong, J. Mater. Chem. A, 2019, 7, 12763

[45] H. Li, P. Zhou, F. Liu, H. Li, F. Cheng, J. Chen, Chem. Sci. 2019, 10, 1374

[46] C. S. Yoon, D. -W. Jun, S. -T. Myung, Y. -K. Sun, ACS Energy Lett. 2017, 2, 1150

[47] S. Xia, L. Mu, Z. Xu, J. Wang, C. Wei, L. Liu, P. Pianetta, K. Zhao, X. Yu, F. Lin, Y. Liu, Nano Energy. 2018, 53, 753

[48] Q. Lin, W. Guan, J. Meng, W. Huang, X. Wei, Y. Zeng, J. Li, Z. Zhang, Nano Energy. 2018, 54, 313

[49] L. Mu, R. Lin, R. Xu, L. Han, S. Xia, D. Sokara, J. D. Steiner, T. -C. Weng, D. Nordlund, M. M. Doeff, Y. Liu, K. Zhao, H. L. Xin, F. Lin, Nano Lett. 2018, 18, 3241

[50] P. Yan, J. Zheng, Z. -K. Tang, A. Devaraj, G. Chen, K. Amin, J. -G. Zhang, L. -M. Liu, C. Wang, Nat. Nanotech. 2019, 14, 602

[51] K. Jarvis, C. -C. Wang, M. Varela, R. R. Unocic, A. Manthiram, P. J. Ferreira, Chem. Mater. 2017, 29, 7668

[52] W. Yang, T. P. Devereaux, J. Power Sources. 2018, 389, 188

[53] S. Roychoudhury, R. Qiao, Z. Zhuo, Q. Li, Y. Lyu, J. -H. Kim, J. Liu, E. Lee, B. J. Polzin, Ji. Guo, S. Yan, Y. Hu, H. Li, D. Prendergast, W. Yang, Energy Environ. Mater. 2020, 0, 1

[54] D. Qian, B. Xu, M. Chi, Y. S. Meng, Phys. Chem. Chem. Phys. 2014, 16, 14665

[55] L. Zou, Z. Liu, W. Zhao, H. Jia, J. Zheng, Y. Yang, G. Wang, J. -G. Zhang, C. Wang, Chem. Mater. 2018, 30, 7016

[56] S. Sharifi-As, F. A. Soto, A. Nie, Y. Yuan, H. Asayesh-Ardakani, T. Foroozan, V. Yurkiv,

B. Song, F. Mashayek, R. F. Klie, K. Amine, J. Lu, P. B. Balbuena, R. Shahbazian-Yassar, Nano Lett. 2017, 17, 2165

[57] N. Li, S. Sallis, J. K. Papp, J. Wei, B. D. McCloskey, W. Yang, W. Tong, ACS Energy Lett. 2019, 4, 2836

[58] K. Luo, M. R. Roberts, R. Hao, N. Guerrini, D. M. Pickup, Y. -S. Liu, K. Edstrom, J. Guo, A. V. Chadwick, L. C. Duda, P. G. Bruce, Nat. Chem. 2016, 8, 684

[59] M. M. Besli, A. K. Shukla, C. Wei, M. Metzger, J. Alvarado, J. Boell, D. Nordlund, G. Schneider, S. Hellstrom, C. Johnston, J. Christensen, M. M. Doeff, Y. Liu, S. Kuppan, J. Mater. Chem. A. 2019, 7, 12593

[60] E. Hu, X. Yu, R. Lin, X. Bi, J. Lu, S. Bak, K. -W. Nam, H. L. Xin, C. Jaye, D. A. Fischer, K. Amin, X. -Q. Yang, Nat. Energy. 2018, 3, 690

[61] J. Hong, H. -D. Lim, M. Lee, S. -W. Kim, H. Kim, S. -T. Oh, G. -C. Chung, K. Kang, Chem. Mater. 2012, 24, 2692

[62] G. Kresse, J. Furthmuller, Phys. Rev. B 1996, 54, 11169

[63] G. Kresse D. Joubert, Phys. Rev. B: Condens. Matter Mater. Phys. 1999, 59, 1758

[64] V. I. Anisimov, J. Zaanen, O. K. Andersen, Phys. Rev. B: Condens. Matter Mater. Phys. 1991, 44, 943

[65] P. E. Blochl, Phys. Rev. B: Condens, Matter Mater. Phys. 1994, 50, 17953

[66] L. Wang, T. Maxisch, G. Ceder, Phys. Rev. B: Condens. Matter Mater. Phys. 2006, 73, 195107

[67] H. J. Monkhorst, J. D. Pack, Phys. Rev. B. 1976, 13, 5188

[68] S. P. Ong, W. D. Richards, A. Jain, G. Hautier, M. Kocher, S. Cholia, D. Gunter, V. C. Chevrier, K. A. Persson, G. Ceder, Computational Materials Science. 2013, 68, 314

[69] B. Xu, C. R. Fell, M. Chi, Y. S. Meng, Energy Environ. Sci. 2011, 4, 2223

[70] F. Kong, C. Liang, R. C. Longo, Y. Zheng, K. Cho, J. Power Sources. 2018, 378, 750

[71] M. W. Chase, J. Phys. Chem. Ref. Data. 1996, 25, 551

[72] F. Kong, C. Liang, L. Wang, Y. Zheng, S. Perananthan, R. C. Longo, J. P. Ferraris, M. Kim, K. Cho, Adv. Energy Mater. 2019, 9, 1802586

Abstract in Korean

국 문 초 록

1991 년 Sony Corporation 이 리튬 이온 배터리 (LIB)를 상용화한 이래 소비자의 요구를 충족하기 위해 광범위한 연구가 수행되었다. 특히 전기 자동차 (EV)와 같은 대규모 에너지 저장 장치의 출현의 급속한 성장에 따라, 저비용 고에너지 밀도 LIB 전극 재료의 개발이 시급히 요구되고 있다. 양극 재 관점에서, 가장 널리 사용되는 $LiCoO_2$ (LCO) 층상 산화물은 낮은 용량 (~ 140 mAh g−1)과 높은 코발트 (Co) 가격으로 인해 산업적 적용 한계에 직면해 있다. 자동차 배터리 요구 사항 (셀 수준에서 US $ 75/kWh 에서 350Wh/kg)을 충족하기 위해선, 고가의 Co 를 다른 원소로 대체하여 가격과 용량의 문제를 해결하는 것이 필요하다. 이와 관련하여 $LiNi_xCo_yMn_{1-x-y}O_2$ (LNCM)의 양극 소재는 여러 가지 장점으로 인해, LCO 적층 산화물을 성공적으로 대체하여 EV 배터리 양극 소재로 널리 사용되고 있다. 그럼에도 불구하고, Ni 가 풍부한 LNCM 층상 산화물의 실제 구현은 사이클에 따른 지속적인 용량 감소로 인한 한계가 존재하며, 특히 Ni 함량이 증가하거나 높은 충전 상태 (SOC)에 도달하면 열화가 점점 심해진다는 단점이 존재한다. 이러한 문제를 극복하기 위해선, 저비용 방법의 개발, 재료 설계를 위한 새로운 전략, 배터리 성능을 위한 전기 화학적 메커니즘에 대한 포괄적 인 이해가 필수적이다.

이 논문의 첫 번째 장에서는, 층상 양극 소재의 intrinsic 특성을 Zr 도핑을 통해 변형함으로써 소재의 성능 향상을 도모하였다. 특히 $LiNi_{0.92}Co_{0.04}Mn_{0.04}O_2$ LIB 양극 소재의 Zr 도핑 효과에 대한 포괄적 인 분석을 제공하며, 이의 결정적인 메커니즘을 발견하는데 중점을 두었다. 첫째, 다중 길이 X 선 분광 분석 및 가스 분석 기술을 채택하여 Zr 도핑이 격자 수축, 입자 균열, 산소 발생, 전해질 분해 및 양이온 혼합을 억제하여 양극 소재의 전기 화학적 성능을 향상시켰음을 보여준다. 그 후, 최첨단 자 기계, 공명 비탄성 X 선 산란 (RIXS),

주사 투과 X 선 현미경 (STXM) 및 제 1 원칙 계산의 협력을 통해 Zr 도핑의 근본적인 메커니즘을 밝히고자 하였다. 위 연구는, 높은 충전 상태에서 Zr 도핑의 산소 산화 억제가 근본적인 메커니즘이라는 것을 처음으로 보여준다.

두 번째 장에서는 층상 양극 소재의 extrinsic 특성을 도핑을 통해 변형함으로써 소재의 성능 향상을 도모하였다. 특히, 인 또는 붕소 도핑을 통해, 1 차 입자가 방사상 방향을 따라 정렬되는 텍스처 미세 구조를 보이는 양극 소재 합성을 진행하였다. 이전 연구는, B 도핑을 통한 텍스처 미세 구조의 기원을 표면 에너지 변형이라 제안하였다. 이와 같은 주장은, 제 1 원리 계산을 사용하여 제안되었지만, 아직까지 미세 구조 변조에 대한 도핑의 정확한 이유는 밝혀지지 않았다. 그리하여, 이 논문에서는 B/P 도핑을 통해 Ni-rich 양극 소재 텍스처 구조의 기원을 밝히기 위한 체계적인 조사가 수행되었다. 위 연구는 B/P 도핑 된 층상 산화물의 독특한 결정 학적 질감은 수산화물 전구체 형태에서 유래한 반면, 그의 메커니즘은 합성 중 재결정 화 시작 온도를 지연시키는 비정질 층의 형성과 높은 관련이 있음을 보여준다.

세 번째 장에서는, 텍스처 구조를 갖는 Ni-rich 양극 소재의 구조 설계에 관한 전략을 제공한다. 구체적으로, 텍스처 구조를 갖는 P 도핑 된 양극 소재와 B 도핑 된 양극 소재의 전기 화학 성능 비교 분석을 진행하였다. P- 및 B- 도핑 된 양극 소재는, 텍스처 구조로 인해 충방전에 따른 미세 균열 형성을 억제하여 도핑 되지 않은 양극 소재 대비 수명 특성이 향상되었지만, 도핑 된 양극 소재 간에 수명 특성 차이가 존재함을 밝혀냈다. 이의 메커니즘을 밝히기 위해, 다중 길이 규모의 X 선 분광 분석에서 가스 분석 기술에 이르기까지 다양한 측정을 수행하였다. 결과로부터, 도핑 된 양극 소재의 수명 특성 차이는 입자 배향면에 따른 산소 안전성의 거동과 높은 관련이 있음을 보여준다.

주요어: 리튬 이온전지, 층상 양극 소재, 도핑, 메커니즘, 텍스처 구조

학번: 2016-20828